Design of Embedded Metal Catalysts via Reverser Micro-Emulsion System: a Way to Suppress Catalyst Deactivation by Metal Sintering

Dissertation by

Noor AlMana

In Partial Fulfillment of the Requirements

For the Degree of

Doctor of Philosophy

King Abdullah University of Science and Technology

Thuwal, Kingdom of Saudi Arabia

The dissertation of Noor AlMana is approved by the examination committee.

Committee Chairperson Jean-Marie Basset

Committee Co-Chair Kazuhiro Takanabe

Committee Member Pascal Saikaly

Committee Member Paolo Fornasiero

ABSTRACT

Design of Embedded Metal Catalysts via Reverser Micro-Emulsion System: a Way to Suppress Catalyst Deactivation by Metal Sintering

Noor AlMana

The development of highly selective and active, long-lasting, robust, low-cost and environmentally benign catalytic materials is the greatest challenge in the area of catalysis study. In this context, core-shell structures where the active sites are embedded inside the protecting shell have attracted a lot of researchers working in the field of catalysis owing to their enhanced physical and chemical properties suppress catalyst deactivation. Also, a new active site generated at the interface between the core and shell may increases the activity and efficiency of the catalyst in catalytic reactions especially for oxide shells that exhibit redox properties such as TiO_2 and CeO_2. Moreover, coating oxide layer over metal nanoparticles (NPs) can be designed to provide porosity (micropore/mesopore) that gives selectivity of the various reactants by the different gas diffusion rates. In this thesis, we will discuss the concept of catalyst stabilization against metal sintering by a core-shell system. In particular we will study the mechanistic of forming core-shell particles and the key parameters that can influence the properties and morphology of the Pt metal particle core and SiO_2 shell ($Pt@SiO_2$) using the reverse micro-emulsion

method. The Pt@SiO_2 core-shell catalysts were investigated for low-temperature CO oxidation reaction. The study was further extended to other catalytic applications by varying the composition of the core as well as the chemical nature of the shell material.

The Pt NPs were embedded within another oxide matrix such as ZrO_2 and TiO_2 for CO oxidation reaction. These materials were studied in details to identify the factors governing the coating of the oxide around the metal NPs. Next, a more challenging system, namely, bimetallic Ni_9Pt NPs embedded in TiO_2 and ZrO_2 matrix were investigated for dry reforming of methane reaction at high temperatures. The challenges of designing Ni_9Pt@oxide core-shell structure with TiO_2 and ZrO_2 and their tolerance of the structure to the conditions of dry reforming of methane will be discussed.

ACKNOWLEDGEMENTS

I would like to thank my committee chair, Professor Jean-Marie Basset, my co-advisor Professor Kazuhiro Takanabe and my committee members Professor Paolo Fornasiero, and Professor Pascal Saikaly for their guidance and support throughout the course of this research.

My appreciation also goes to my friend Bedour Alsabban, Dr. Paco Laveille and colleagues in KCC department who were willing to participate in the study and for making my time at King Abdullah University of Science and Technology a great experience. I also want to extend my gratitude to the King Abdullah University of Science and Technology, which provided the instrument and funding, in addition to the basic funding provided by SABIC and ARAMCO.

Finally, my heartfelt gratitude is extended to my mother, sister, and brothers, and for their encouragement and their love which made all this possible, and to my husband for his patience and support. My brother Hobby and my daughters are my strength and motivation in each and every step I take.

To hobby.

To my family.

TABLE OF CONTENTS

CHAPTER 1

1. Introduction, motivation and state of the art

1.1 Introduction and motivation

Catalysis was introduced for the first time in 1836 by Berzelius to explain a certain type of chemical cycle where additional substances called “catalysts” increase the rate of a chemical reaction, without changing the thermodynamic equilibrium of this reaction, by facilitating the interaction of the reactants and the release of the products.[1] Ideally, the catalysts should not be consumed in the chemical cycle however real catalysts deactivate and are structurally changed during the catalytic process which affect their efficiency. The loss of catalytic activity is considered as a major problem for industrial processes since it costs billions of dollars per year to regenerate and/or replace the catalysts.[2] Heterogeneous catalysts are usually used as industrial catalysts rather than homogeneous catalysts (but strong process exist also in homogeneous catalysis (e.g. dimersol)) this preference is due to the ability to separate easily heterogeneous catalysts at the end of the reaction, to reuse them and to use them at high temperature where they exhibit thermal stability.[3] The heterogeneous catalysts consist of so called active sites present at the surface of metal particles or oxides or sulfides or even acidic catalysts. The metal particles are dispersed on a high surface area and thermally stable inorganic support (usually metal oxides).[4]

In heterogeneous catalysis the catalytic activity is in principle determined by the turnover rate, TOR, defined by the amount of products formed per site per unit time.[5] But frequently the number of active site is not known precisely. For this reason, researchers innovated different synthetic procedures to maximize the expected surface area by producing highly dispersed and stable catalysts.

The development of heterogeneous catalysis material with a stable active metal surface area and precise control of morphology, size and distribution of nanomaterials are of great of importance for controlling the activity and selectivity of the desired reactions. The innovation of nanotechnology in the catalysis field has brought an exciting era of scientific research where researchers can see clearly nanoparticles (NPs) at an atomic level.[1] This has improved the fundamental understanding of catalysis and thus the development of well-defined catalysts materials.

However, as already mentioned, the sintering of particles is a severe problem in heterogeneous catalysis, which should be avoided, when the catalysts lose the surface. This phenomenon usually occurs at high temperature, and it might also happen under milder conditions. So, the development of heterogeneous catalysts stable against sintering at high temperature is of great of interest for industrial applications. Core-shell nanocomposites have gained a lot of attention in the recent year as a possible solution to solve sintering problem. Despite tremendous advances made in the field of core-shell in recent years, many aspects of the processes involved in preparing and developing porous core-shell structures

still require greater insights. Specifically, emphasis was placed to provide some answers to the following questions:

How can core-shell NPs solve agglomeration problem?

If these particles are already in use, what are the techniques and processes employed to make them?

Which industrial applications has already been developed the core-shell NPs?

How thermally and chemically stable are core-shell NPs in industrial catalysis?

What are the remaining challenges for the preparation and use of core-shell NPs?

A literature review will be done in the next section to find an answer for the above-mentioned questions. The aim of this work was to gain a deeper understanding of the core-shell systems, their properties, their chemistry, the control of their morphology and thermal stability in industrial reactions. We also wish to find ideal synthesis procedure/protocol for the production of porous core-shell structures with high control of their size and composition.

In our laboratory “Catalysis by Design” is the target approach to design a novel catalyst systems. We utilize nanotechnology to develop a core-shell system that can protect metal NPs against sintering at high temperature by encapsulation within a porous oxide shell. The core-shell material can be heated to 500°C or above without loss of activity as it shown during the CO oxidation and dry reforming tests. High thermal stability against metal sintering is achieved by a protective layer

of oxide around the metal NPs that avoids the direct contact between the particles thus the particle growth via particle coalescence is inhibited.

Chapter 2 describes: the mechanism of forming core-shell particles and the influences of certain parameters on the properties and morphology of the SiO_2 shell was investigated using reverse micro-emulsion method. The promising results of $Pt@SiO_2$ core-shell catalysts led to the conclusion that the concept needs to be extended; to expand the window of catalytic applications, the composition of the core has to be varied, as well as the chemical nature of the shell material.

In chapter 3, the concept of catalyst stabilization by a core-shell method was employed for the development of further variations on the entrapment of metal NPs within the oxide layer.

- The first target was the fabrication of Pt NPs stable against sintering by embedding them within another oxide matrix such as ZrO_2 and TiO_2.
- This was accompanied by the study of the factors governing the coating of the oxide around the metal NPs.
- Furthermore, the catalytic activity of the resulting materials was examined in the CO oxidation reaction to find out whether the entrapment approach leads to a stabilization of the Pt NPs after thermal treatment at elevated temperatures.

Chapter 4 describes: a more challenging system than Pt monometallic particle, namely, bimetallic Ni_9Pt NPs were investigated for the dry reforming of

methane reaction. Ni NPs were added to the Pt to increase the activity of the catalysts and to make it suitable for the application of dry reforming of methane. The amount of ZrO_2 and TiO_2 were varied to achieve the right amount of the oxides vs. the amount of Ni_9Pt NPs. Both $Ni_9Pt@TiO_2$ and $Ni_9Pt@ZrO_2$ catalysts were tested in the dry reforming of methane to check their stability against the rather severe conditions of this reaction.

1.2 State of the art

1.2.1 Core-shell NPs

1.2.1.1 Historical perspective

The definition nanomaterials are employed to describe a class of materials that have at least one dimension in the nanometer scale (≤100 nm) range.[6] These materials have gained a lot of attention due to their unique and much-enhanced properties compared with the bulk materials.[7] The initial research focused on the single NPs, however, later it was realized, in the late 1980s, that composite, heterogeneous, hybrid or sandwich colloidal particles have improved efficiency; in some cases, they might even educe some new characteristics than their corresponding single particles.[8-9] In the early 1990s, the terminology “core-shell” was adopted for a “concentric multilayer” semiconductor NPs.[10-12] Subsequently, with the advancement in the research study of core–shell nanocomposites, the term “core-shell” was extended to include nanomaterials having a distinguished

outer layer material (shell) wrapping, either entirely or partially, the inner material (core) with the ability to identify them separately.[13] The research activity in different core-shell material has increased gradually along with the development of characterization techniques which greatly helped the fabrication of such materials.

1.2.1.2 Importance of core-shell NPs

The application of core-shell NPs has expanded from material chemistry to other fields such as biomedical, electronics, catalysis, optics, and pharmaceutical. This is due to their multifunctional capabilities, versatile compositions and structures coming from emerging different materials together, which manipulate their surface functions to meet the requirements of diverse applications.[6, 14] Moreover, new distinctive properties may be devolved by the core-shell structure depending on the interaction among the shell and the core.[15-18] There are many reasons for coating the core NPs with addition shell layer, such as increase the functionality, stability, surface alteration, controlled release of the core, dispersibility, lowering the consumption of expensive materials, etc.[6]

Core-shell nanomaterials were widely used in various applications (**Figure 1**) such as enhanced optical devices[19-21], bio-nanotechnology[22-24], pharmaceutical applications[14], photoluminescence[25-26], electronics[10, 27], energy storage materials[28], fuel cell[29] and many important catalytic processes[30-37]. See **Figure 1**.

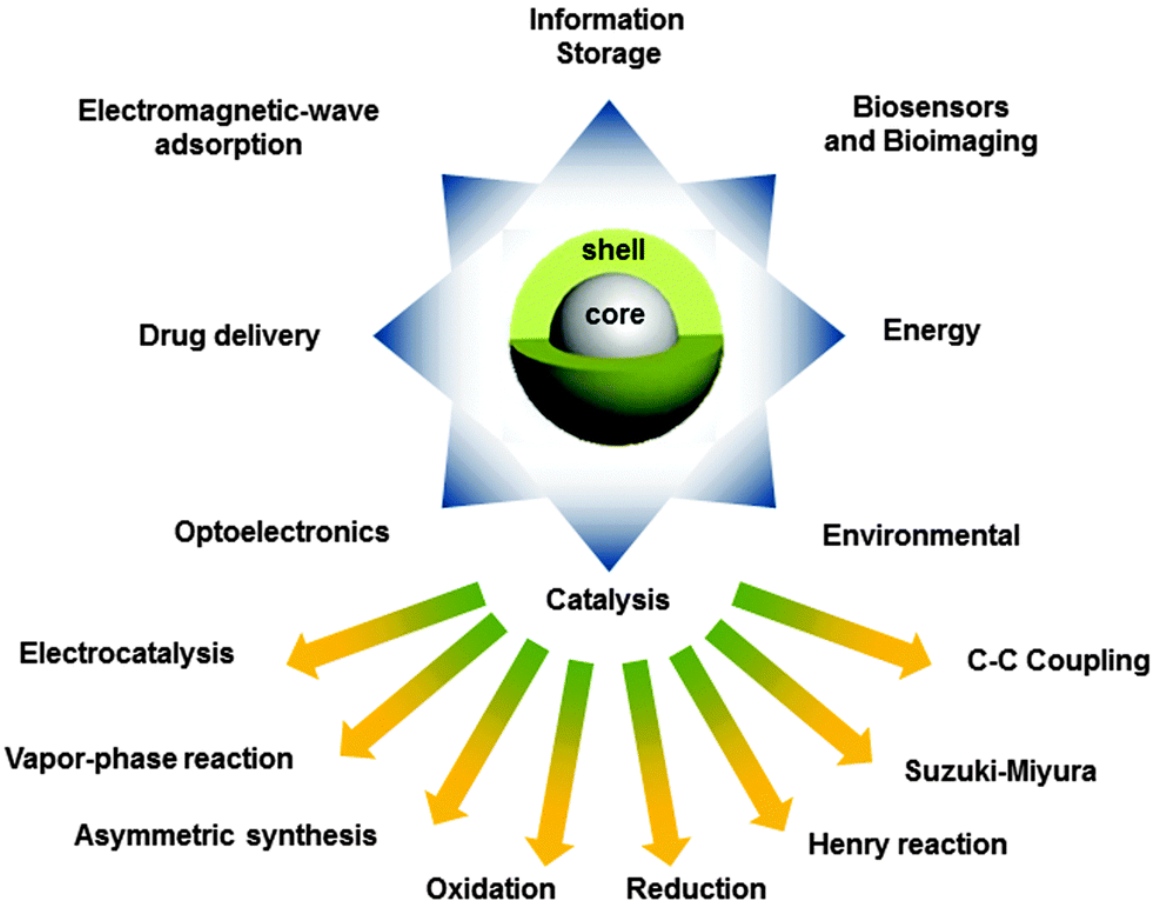

Figure 1. Applications of core-shell NPs in several applications of modern technology *particularly in the field of catalysis* (adopted from[38]).

1.2.1.3 Shapes and classes of core-shell NPs

With the advances in the synthesis procedures, it is possible to fabricate various structures of core-shell NPs (**Figure 2**) such as (a) “spherical”; (b) “hexagonal”; (c) “multiple-core” materials coated by single shell; (d) “sandwich-type”; (e) “rattle-type hollow sphere”. The properties of core-shell materials depend on both size and shape of the core-shell NP.[39-42]

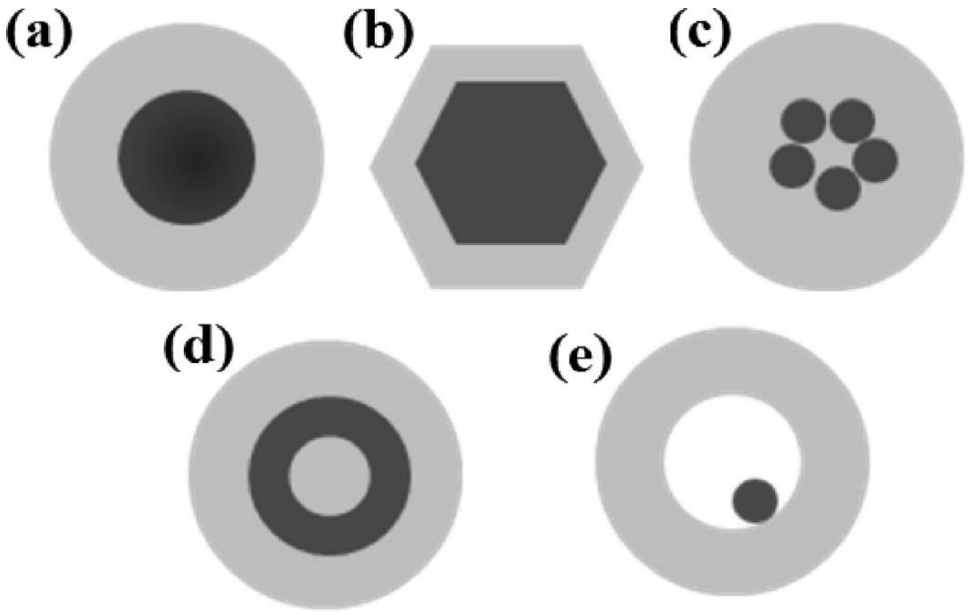

Figure 2. Different structures of core-shell materials: (a) “spherical”; (b) “hexagonal”; (c) “multiple-core”; (d) “sandwich-type”; (e) “rattle-type hollow sphere” (adapted from [6]).

Core–shell nanostructures can be categorized into several classes based on the arrangements and compositions of the two components (inorganic and organic) in the materials (***Figure 3***); including “inorganic/inorganic”, “organic/inorganic”, “inorganic/organic’, and ‘organic/organic’ type core–shell NPs.[29, 43-44] “Inorganic/inorganic” core-shell NPs are the most important class and will be the focused in the current thesis since these types of materials are now widely applied for the enhancement of catalysis.

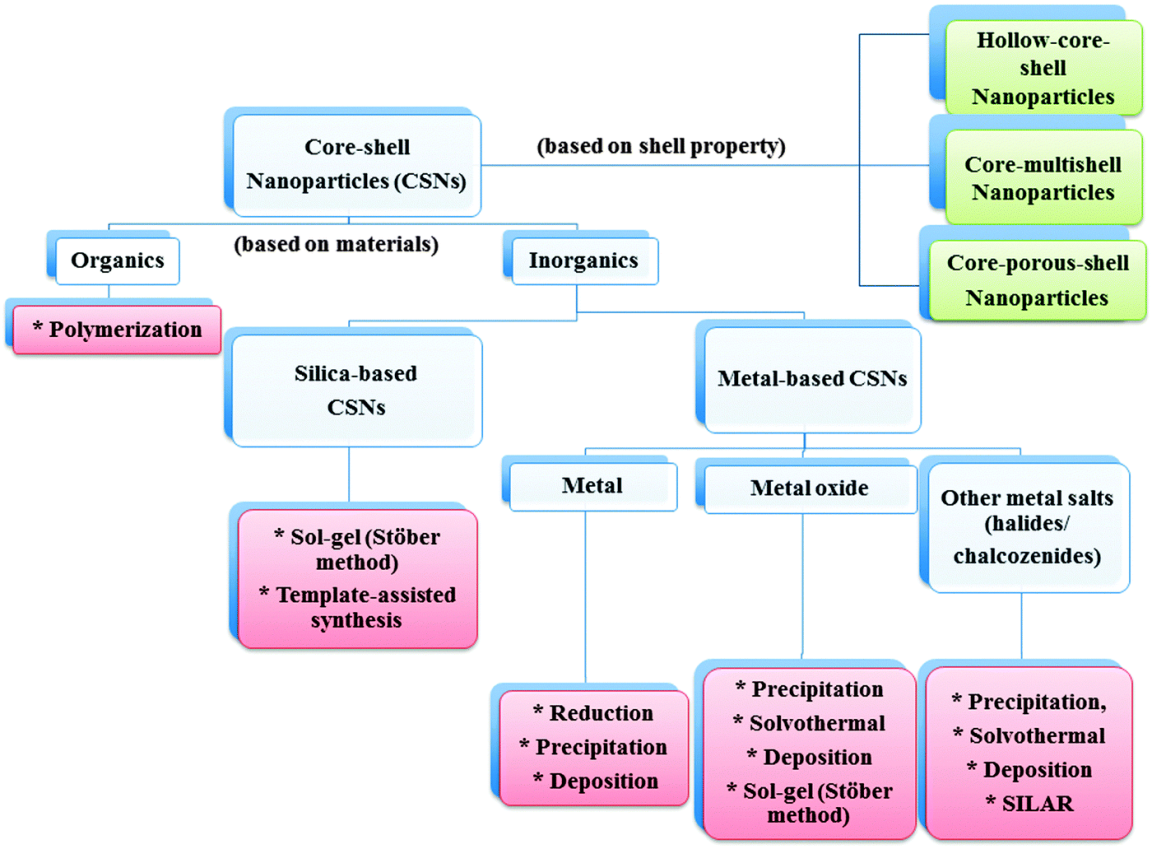

Figure 3. General classification of core–shell NPs depending on material-type (beside with the most synthetic approaches) and properties of their shells (adapted from [38]).

The different kinds of inorganic/inorganic materials, based on the nature of the shell substance, are made of metal, metal oxide, other inorganic materials, or silica. They can be broadly categories into two groups: either silica-containing ones or those consist of a metal-based material. The choice of shell layer of the core-shell NP is strongly relying on the end use and application.

1.2.1.4 General synthesis strategies for core-shell NP

The SiO_2-coated core-shell materials are produced using “sol–gel” chemistry which involve the hydrolysis of silicon alkoxides followed by

condensation in a polar solvent, water for example, in the existence of a base catalyst, ammonia for example. Stöber process is a well-known method and widely used to synthetize mono-dispersed SiO_2 particles due to its reproducibility, simplicity, in addition to versatility. However, a solid non-porous SiO_2 layer is generated form this technique and can only be used for synthesizing SiO_2-based materials. Newer approaches have now been established to produce porous shells using either template-based procedures or post-synthetic treatments.[38] Porous SiO_2-based core-shell nanostructures have the enhanced accessibility of the cores and shells along with increased surface area of the material. Furthermore, the pores of the core-shell nanostructures can further be improved with various functional groups, providing the nanostructures with multi-functionality for different catalytic reactions. However, the size of the core-shell composite obtained from Stöber method is usually between 100 nm to a few μm since the small NPs are unstable and lean to aggregate in the alcoholic solution; also other structures than core–shell are seldom generated. The reverse micro-emulsion technique is a better route to get silica-based nanomaterials with smaller size and versatile structures. The thickness of SiO_2 layer can be controlled by changing the experimental conditions such as the concentration of precursors, catalyst, coating time, and presence of other reactants. We will discuss reverser micro-emulsion method in details in coming section.

Metallic core-shell NPs, on the other hand, are usually generated via reduction of their metal precursors, either by using reducing agents (such as hydrazine, $NaBH_4$, etc.) or by a metal ion-exchange (transmetallation) via effective

redox of the metal precursors and ligands. The type of reducing agent, temperature and reaction medium are crucial parameters that influence the reduction kinetics including particle size, growth, shape and thereby the properties of resultant material.

Metal oxide-based materials core-shell NPs (such as titania, zirconia or ceria), are often produced via the ‘‘sol–gel’’ chemistry (similar to that used for silica). However, the synthesis of these oxides are challenging compared to SiO_2 since the kinetics that involves their formation are faster than with SiO_2 due to the moderately higher reactivity of their precursors.[38] In addition, the high solubility of silica-based systems in polar solvents such as water makes them more dispersed in these solvents, which is less applicable to other oxides.[45] The dispersibility of oxide NPs is a key feature for avoiding the formation of aggregates.[45]

There are other synthetic procedures than sol–gel method that are also used to coat metal oxides, namely, thermal decomposition or co-precipitation methods which depend on the chemical properties of the metal precursors. Thermal decomposition technique involves organometallic precursors treated at high temperature in the presence of air or oxygen to obtain the final material. The co-precipitation method is usually used for metal hydroxides/oxides that are able to precipitate under basic conditions. There are other physical techniques that can be used for the deposition of the oxide layer as a shell such as electrochemical deposition and chemical vapor deposition. However, the coating of the oxides layer around the core material and the thickness of the shell by the previously mentioned

synthesis method are poorly controlled, which leads to a decrease in catalytic activity due to low diffusion of the gases in the shells that are thicker than desired.

Recently, M. Cargnello et.al.[45-46] reported a new sophisticated procedure for the synthesis of Pd@CeO_2 core-shell via a layer-by-layer supramolecular method that involves ligand exchange between thiol functionalized Pd and cerium alkoxide $Ce(OR)_4$. However it is a multi-step process and it cannot be applicable for another metal oxides such as TiO_2 and ZrO_2.

Reverse micro-emulsion method is a promising tool for the synthesis of oxides shell with high control of the composition, thickness, and size of metal oxide shell. Many researchers reported the synthesis of various oxides via this method such as SiO_2[47-52] , TiO_2[53]or CeO_2[54-56] for different catalytic reactions. This synthesis procedure will be elaborated more in the next section.

1.2.2 Core-shell NPs by reverse micro-emulsion procedure

Reverse micro-emulsion technique consists of nano-size droplets of water surrounded by a self-assembled surfactant to form a kind of thermodynamically stable nanoreactor or so-called reverse micelles dispersed in an organic solvent.[57-58] The reactants exchanged among the micelles through collision produce NPs.[58-60] Different types of nanomaterials can be synthesized in these nanoreactors such as inorganic minerals,[61] organic materials,[57, 62] metals,[63-66] metal oxides,[67] or even mixed oxides,[68-71] in a mild condition and rather simple operations. Moreover, the confined space of nanoreactor environment can

produce fine and mono-dispersed particles, smaller than these nanodroplets, with narrow size distribution as well as control the composition of the metal alloy.[48, 58] There are different structures of the micelles: spherical which has the lowest energy or elongated micelles that act as a template for the prepared nanomaterials.[48, 60, 72-74] There are crucial parameters that play a vital role in this procedure which affect the size, shape and stability of micelles and eventually the morphology of synthesis material.[48, 60, 73] These parameters are the surfactant and organic solvent type, water to surfactant molar ratio (*R*), and type and concentration of reactants.[57, 60, 72] This is a very expanding area, and most of the mentioned parameters and their influence on micelles characters have been well studied and reported in previous papers.[57, 59-60, 72, 75]

One of the most prominent advantages of micro-emulsion technique is the possibility to perform sequential reactions using the confined environment by adding new reactants and reagents; e.g., the first reaction includes formation of the uniform seeds of metal particle (core), followed by adding other separate reactants to proceed to coat those core (shell).[74] For instance, micro-emulsion methods were applied to fabricate an extra uniform layer of NPs with a very precise size control forming different kinds of morphologies such as ‘onion-like’, ‘yolk-shell, and core-shell structures.[48, 74] Several bimetallic core-shell NPs synthesized by micro-emulsion were reported in the literature (few examples Ni@Au,[76] Au@Pt,[77] and Pd@Au).[78] Not only coating additional layer of metallic NPs to the primary metal was possible by micro-emulsion, but also metal oxide layer can be delicately added around the metal. Indeed, many metal NPs were protected against sintering

at high temperature by encapsulation within a porous SiO_2[47-52] , TiO_2[53], CeO_2[54-56] or $Ce_xZr_{1-x}O_2$[56] forming core@shell structures prepared by micro-emulsion for different catalytic reactions. The thickness of oxide layer can be tailored by the reagents concentration.

A great deal of research has reported the advanced synthesis of metal@oxide core-shell NPs via revers micro-emulsion method.[47, 51-52, 79-81] The importance of core-shell structure for high-temperature catalysis was emphasized by Joo *et al.* using Pt metallic particle core with a mesoporous SiO_2 to protect metals from sintering while maintaining accessibility to the active metal surfaces.[82] **Figure 4**, **Figure 5**, **Figure 6**, **Figure 7** and **Figure 8** are examples from the literature of SiO_2-based shell materials. Guerrero-Martínez *et al.*[83] pointed out in his review in 2010, the possibility of synthesizing of core–shell silica-based nanocomposites in reverse micro-emulsions method whether the cores are pre-synthesized or synthesized in situ which is an advantage for this method.

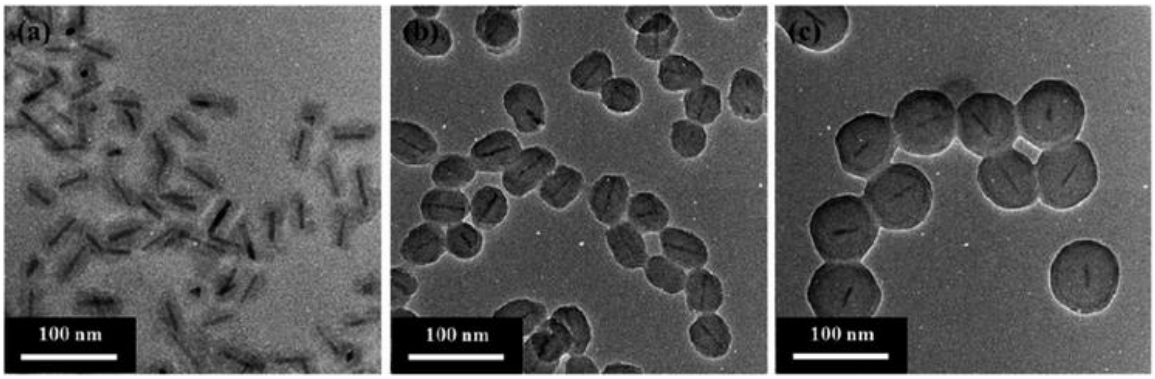

Figure 4. TEM images of CoO@SiO_2 with a shell thickness of (a) 11.7, (b) 20.1, and (c) 32.6 nm (adopted from[84]).

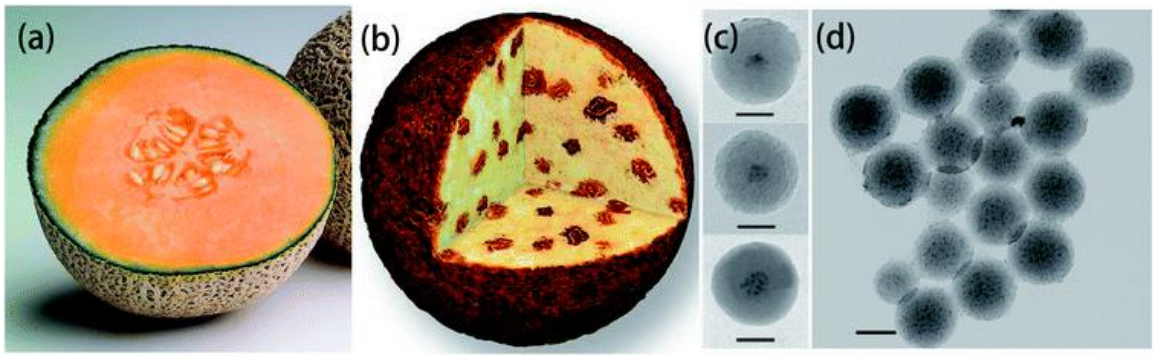

Figure 5. (a) “Muskmelon” (b) “Raisin-bun” model (c) TEM images of “muskmelon” structured CdTe@SiO_2 particles (adopted from [85]).

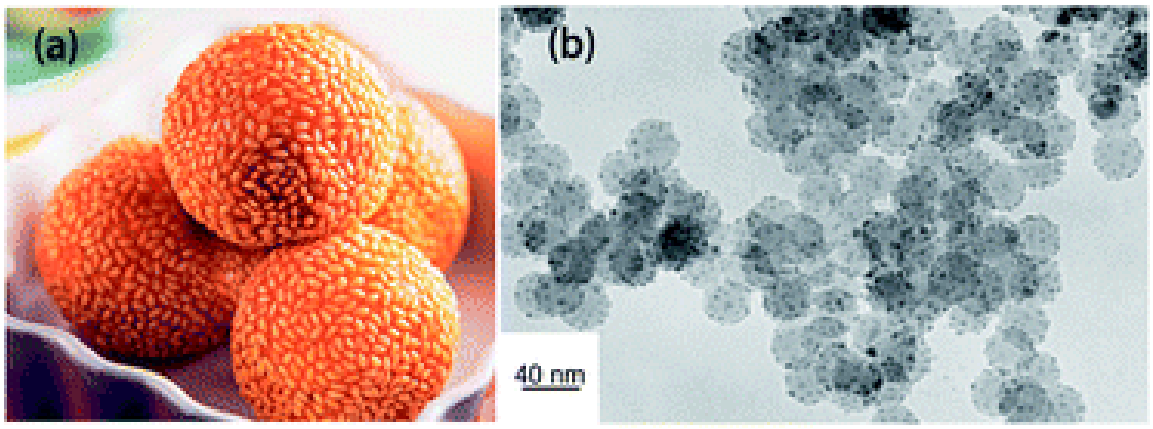

Figure 6. (a) “Glutinous rice sesame balls” (b) TEM image of silver-coated silica NPs (adopted from[86]).

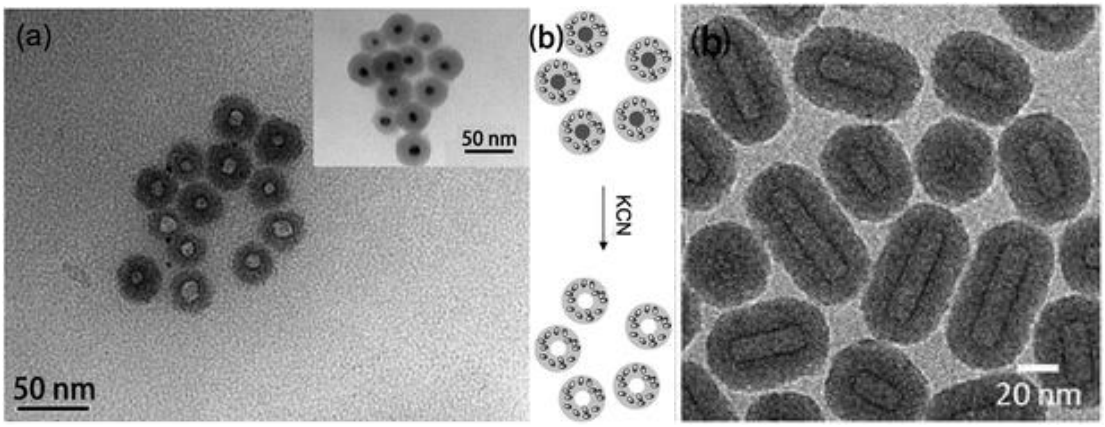

Figure 7. (a) TEM images of hollow SiO_2-FITC. The inset displays the Ag@SiO_2-FITC before etching with schematic presentation of the formation mechanism (adopted from [87]) (b) TEM images for hollow Ni@SiO_2 synthesized (adopted from [48]).

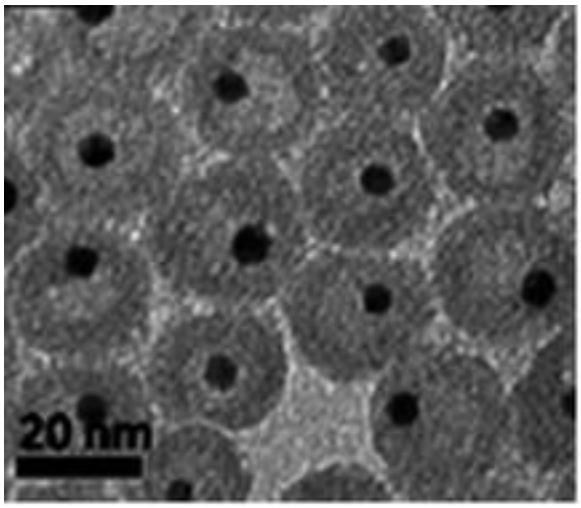

Figure 8. TEM images of "yolk–shell" Au@SiO_2 (adopted from [88]).

Although there were intensive reports on the synthesis of core-shell material via micro-emulsion, however, the detailed mechanism of their fabrication and critical parameters that affect their formation is still not explored. Deeper

understanding of the core-shell systems, their properties, chemistry and morphology control obtained by the reverse micro-emulsion method is important first step for catalytic chemist to develop and design catalysts with high effective and control approach.

1.2.3 Catalysts deactivation by sintering

Catalyst deactivation is the loss of catalytic activity (amount of products/g_{cat},h) and/or selectivity (product distribution) over time, which is a serious problem for industrial catalytic processes and costs total billions of dollars per year for the regeneration of the catalysts.[2, 89] The possible causes for catalyst deactivation (**Figure 9**) are: (1) chemical degradation including leaching and volatilization, (2) mechanical degradation, (3) fouling, coking and carbon deposition, (4) thermal degradation and (5) poisoning.[2, 89] We will focus in this chapter on the catalyst decay by thermal degradation (metal sintering).

The efficiency of the catalysts towards industrial applications is dependent on the size of the metal particles in relation with the dispersion of the active metal over catalyst support; the higher and the smaller the dispersion and size of the active metal particle, respectively, the higher their activity in the catalytic reaction.[90] The dispersion is lost over time due to thermal degradation of the catalyst when exposed to alternatively oxidative and/or reductive atmospheres especially at high temperature (above 600 °C). [91] The thermal degradation, also known as “sintering’, of catalyst are: (1) the loss of catalyst’s active surface of small metal crystallites into larger ones due to crystallite growth of the metal (**Figure 9C**),

and/or (2) loss of support area due to a collapse of pore structure which leads to encapsulation of active metal particles (**Figure 9D**).[2, 89] Understanding the mechanism of metal sintering could be an important first step for catalytic chemist to develop and design catalysts having better durability and resistance for sintering.[92] Three main mechanisms of crystallite metal growth have been proposed: (1) “atomic migration” (also known as “Ostwald ripening”), (2) “crystallite or particle migration”, and (3) “vapor transport” (occurs at very high temperatures).[2, 89, 92] “Atomic migration” involves migration of metal atoms or molecular metal or clusters, that detachment from crystallites, over the support surface and eventually capture by larger crystallites.[2, 89, 92] “Crystallite or particle migration” is the Brownian motion of particles which involves the migration of whole crystallites over the support surface leading to collision and coalescence when particles come close to each other.[2, 89, 92] The sintering mechanism may change from particle migration to Ostwald ripening depending on the size of NPs.[93] Particle or crystal migration occurs in the early phases when the NPs are very small then Ostwald ripening occurs when the NPs become large and immobile.[93-95]

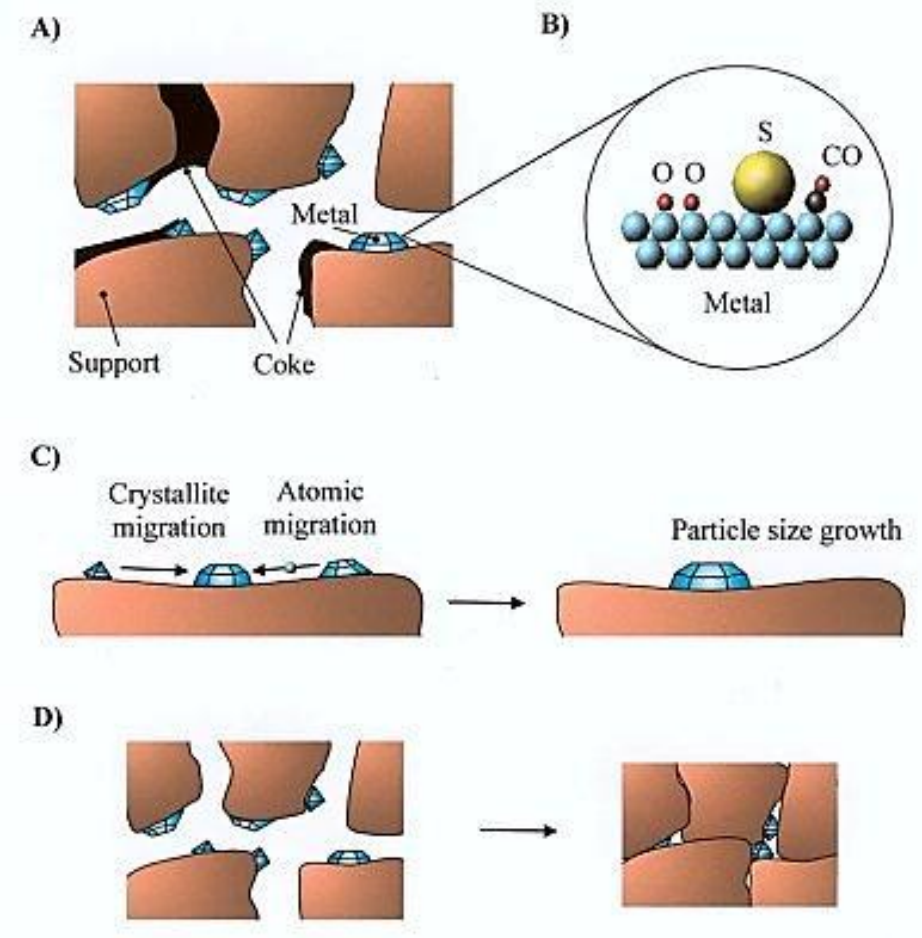

Figure 9. Deactivation mechanisms: A) “coke formation”, B) “poisoning”, C) “sintering of the active metal particles”, and D) sintering and “solid-solid phase transitions” of the support and encapsulation of active metal particles (adapted from [96]).

There are different factors that affect the rate of sintering of the metal particles: Temperature, support surface area, metal type, atmosphere, metal dispersion, texture and porosity, and promoters/impurities (see **Table 1**,[2, 89]). Sintering rates is accelerated exponentially by increasing temperature especially in oxygen and water vapor relatively slowly in hydrogen.[2, 89, 91] Also, the smaller the size of metal particles and the lower their “Tammann temperature” (half of the

bulk melting point in degrees Kelvin indicates the temperature at which sintering starts), the higher tendency for them to grow and sinter.[97] For instance, Rh is known to be the most sensitive metal towards sintering under different ageing atmospheres compared with other the active metals Pt and Pd, which leads to poor activity in catalytic reaction.[98-100] In addition to temperature, time and atmosphere, the rate of sintering is also dependent on several other aspects, such as loading of the metal and composition of the support.

Solid-solid phase transition is the transformation of one crystalline phase into another which happens at very high temperatures. For example, highly porous γ-alumina transform to non-porous α-alumina at high temperature and it is much more sensitive to sintering than α-alumina.[97] Exposing γ-alumina to a high temperature (>750°C) will collapse their pores leading to encapsulation of metal particles into support matrix (**Figure 9D**).

Table 1. Effects of important catalyst variables and reaction conditions on the rates of sintering for supported metals (adopted from [2, 89]).

Variable	Effect
Temperature	Sintering rates are exponentially dependent on T; E_{act} varies from 30 to 150 kJ/mol; E_{act} decreases with increasing metal loading; it increases in the following order with atmosphere: NO, O_2, H_2, N_2
Atmosphere	Sintering rates are much higher for noble metals in O_2 than in H_2 and higher for noble and base metals in H_2 relative to N_2; sintering rate decreases for supported Pt in atmospheres in the following order: NO, O_2, H_2, N_2
Metal	Observed order of decreasing thermal stability in H_2 is Ru > Ir ≅ Rh > Pt; thermal stability in O_2 is a function of (1) volatility of metal oxide and (2) strength of metal oxide–support interaction
Support	Metal–support interactions are weak (bond strengths of 5–15 kJ/mol); with a few exceptions, thermal stability for a given metal decreases with support in the following order: Al_2O_3 > SiO_2 > carbon
Promoters	Some additives decrease atom mobility, e.g. C, O, CaO, BaO, CeO_2, GeO_2; others increase atom mobility, e.g. Pb, Bi, Cl, F, or S; oxides of Ba, Ca, or Sr are "trapping agents" that decrease sintering rate
Pore size	Sintering rates are lower for porous vs. non-porous supports; they decrease as crystallite diameters approach those of the pores

Table 2. Effect of ageing atmosphere on the sintering behavior (NPs size) of Pd, Pt, and Rh (metal loading 0.14 wt-%, support La_2O_3-doped Al_2O_3) (adopted from[99]).

Particle size (Å)	Pt	Pd	Rh
N_2 / 1100°C	210	970	140
Exhaust gas / 1100°C	780	680	880
Air/ 1100°C	970	n.d.	n.d.

n.d. = not determined

The kinetics of a catalyst sintering is a function of, time, pressure, temperature, and the concentrations of different reactants. The kinetics of sintering can be derived at a constant temperature from surface area of active metal *versus* time measurements. **Equation 1** can be applied in a quantitative comparison regarding the effect of time, atmosphere and temperature on the rate of sintering of supported metal catalysts.[2, 89]

Equation 1.

$$\frac{d(D/D_0)}{dt} = -k(D/D_0 - D_{eq}/D_0)^n$$

where
- D is the metal dispersion (or metal surface area),
- D_0 is the initial metal dispersion (or initial metal surface area),
- D_{eq} is the final dispersion (when the asympototic approach is achieved),
- k is the kinetic rate constant for sintering, and
- n the sintering order.

1.2.3.1 Strategies to reduce sintering

There are different ways that have been reported in the literature to reduce the sintering affect. For instant, bimetallic catalysts was used such as Pt-Rh or Pd-Rh which gave an improved catalytic activity at high temperatures. [99] Also, some specific promoters are known for minimizing the sintering of a catalyst such as: BaO, ZrO_2, CeO_2, MgO, and La_2O_3 enhance the stability of γ-Al_2O_3 against sintering in the presence of high concentration of water.[101-102] Increasing metal-support interaction by using reducible oxides such TiO_2 is another way to reduce sintering.[4, 103]

Coating metal NPs with a mesoporous oxide over layer have been the center of many researchers. It is an interesting approach to prevent the metal growth since oxides physically separate metal NPs from each other and oxides also exhibit higher thermal stability than metal NPs. However, many factors should be considered when applying this approach such as diffusion of reactant through oxide shell, use the suitable oxide for certain application and finding the effective synthesis method to coat oxide layer over metal NPs.

1.2.3.2 Core-shell catalysts for industrial applications

As mentioned previously, core-shell systems have attracted a lot of researchers working in the area of catalysis owing to their enhanced physical and chemical properties towards catalyst deactivation. Also, new active sites generated at the interface between the core and shell increases the activity and efficiency of

the catalyst in catalytic reactions especially for oxide shells that have redox properties such as TiO_2 and CeO_2. Another advantage of coating oxide layer over metal NPs is selectivity of the various reactants by the different diffusion rates of the substrates through a micro-pore oxide shell. In this section we will discuss the thermal stability and the properties of oxide coated metal NPs catalysts for industrial applications.

Recently, many researchers reported the protection of metal NPs against sintering at high temperature by encapsulation within a porous SiO_2 shell forming core-shell structures for different oxidation and reforming reactions.[104-109] For instant, Takenaka *et al.*[47, 51] reported that the Pt NPs in Pt@SiO_2 core-shell catalyst was protected against sintering in contrast of supported Pt/SiO_2. In addition, the Pt@SiO_2 core-shell catalyst had similar activity in oxidation of different hydrocarbons (tested at 300°C) with supported Pt catalyst, however, Pt@SiO_2 core-shell catalyst exhibited higher selectivity to methane oxidation. This selectivity was attributed to the difference in the diffusion rates of the hydrocarbons through the micro-pore silica shell to the active Pt surface. Takenaka *et al.*[49] also reported the Ni@SiO_2 catalysts with 2–5 nm Ni particles size covered uniformly with 10 nm silica layer investigated in partial oxidation of methane at various temperatures (650°C, 700°C and 800°C). The Ni supported on SiO_2 catalyst had a low catalytic activity and deactivated rapidly due to oxidation of Ni into NiO and formation of coke. On the other hand, the confined structure of core-shell Ni@SiO_2 catalysts did not have enough space for fibrous carbons to grow and the catalyst exhibit high stability and catalytic activity. Moreover, the strong interaction of Ni

NPs with SiO_2 had prevented the detachment of the Ni from the SiO_2 support, which typically occurs if fibrous carbons start to grow. Another study of Ni@SiO_2 core-shell catalyst conducted by Takenaka *et al.*[109] for propane steam reforming. The performance of Ni@SiO_2 core-shell catalyst was compared with the Ni NP supported on magnesia (MgO), silica (SiO_2) and alumina (Al_2O_3).The Ni@SiO_2 core-shell catalyst showed higher activity for propane steam reforming at 600°C than Ni/Al_2O_3 and Ni/MgO catalysts whereas the silica-supported Ni exhibited poor catalytic activity. The coating of Ni metal NPs with silica not only improved their catalytic activity but also lower carbon deposition during the steam reforming of propane at 600°C than that on Ni/Al_2O_3 and Ni/MgO catalysts.

Han *et al.*[110] showed that supported Ni catalysts coated with additional mesoporous SiO_2 layer by Stöber method (“sandwich-type” Pt core@shell catalysts “SiO_2@Pt@SiO_2” were resistance for coke and sintering under DRM conditions. Li *et al.*[50], studied the effect of various silica shell thickness (3, 6, 9, 11 and 15 nm) of the “yolk−satellite−shell” structured of Ni−yolk@Ni@SiO_2 nanocomposite on metal sintering and the catalytic performance for CO_2 reforming of methane reaction (tested at 800°C). He found that the catalyst with 11 nm SiO_2 shell was resistance to sintering and had best catalytic activity among other catalysts. The Ni−yolk@Ni@SiO_2 nanocomposite with thin SiO_2 shell (3, 6 and 9) suffer from metal sintering and/or carbon formation. “Cross-linking” between silica shells occurred during the reaction of the catalysts with 3 and 15 nm SiO_2 shell thickness. Also, the SiO_2 layer becomes denser due to further dehydration between hydroxyl groups. He explained that the cross-linking happened due to

water vapor generated by reverse water gas shift reaction leading to hydroxylation between −(Si−O−Si)− groups which create polymeric chains of −$Si(OH)_2$−O−$Si(OH)_2$−OH groups, that link up to form 3D networks.

Indeed, although intensive research was done on SiO_2 shell due to their relative simple synthesis compared with other oxides, however, SiO_2 is known to be unstable under the steam condition.[50, 111] Moreover, SiO_2 is relatively an inert oxide that follows a mono-functional pathway for the mechanism of dry reforming of methane for example, where the metal only activates both reactants leading to carbon formation and deactivation.[112] Core-shell NPs with oxide shell, other than SiO_2, that can produce core-shell with bi-functionally properties (such as TiO_2, ZrO_2, and CeO_2) is really interesting for industrial application, however the synthesis of such oxides is more challenging.

An *et al.*[113] investigated thermal stability and role of the support of sandwich-type Pt core@shell catalysts (SiO_2@Pt@TiO_2 and SiO_2@Pt@SiO_2) compared with supported Pt NP on either mesoporous SiO_2 or TiO_2 catalysts. The four catalysts were tested in n-Hexane reforming at 240−500°C (**Figure 10**).The support Pt/TiO_2 catalyst represents the highest reaction rate and isomerization selectivity 8 times greater than other catalysts and was also resistance to Pt sintering due to strong interaction between Pt and TiO_2. The supported Pt NPs on SiO_2 on the other hand suffered from sintering and gave low reaction rate. The Pt NPs of SiO_2@Pt@SiO_2 core@shell catalyst did not suffer from sintering up to 500°C, however, the reaction was lower than Pt/TiO_2 while TiO_2 layer of the SiO_2@Pt@TiO_2 did not protect the Pt NPs completely from sintering (**Figure 10**).

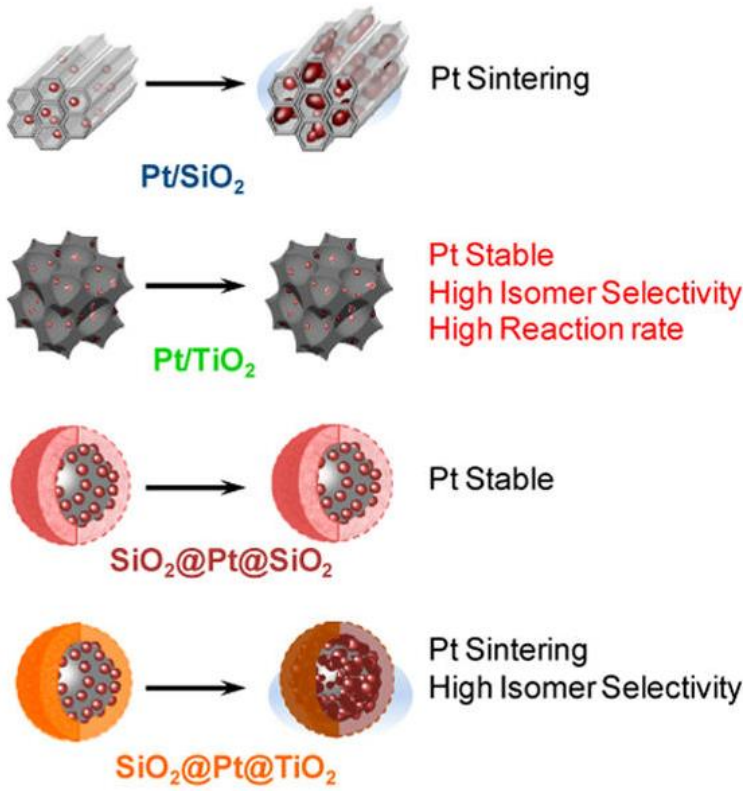

Figure 10. Schemes of Pt/SiO_2, Pt/TiO_2, $SiO_2@Pt@SiO_2$, and $SiO_2@Pt@TiO_2$ before and after reforming reaction at 500°C (adopted from [113]).

Arnal *et al.*[114] have successfully synthesized highly thermal stable (up to 800°C) $Au@ZrO_2$ yolk-shell structure. The $Au@ZrO_2$ was stable against sintering and cursing under static pressure of 1 GPa. To prepare this material $Au@SiO_2$ was first synthesized, then surfactant covered surface of the SiO_2 prior the coating of ZrO_2 layer. After that the SiO_2 was leached out from $Au@SiO_2@ZrO_2$ core-shell structure and surfactants was burned at 900°C creating 2-3 nm porous layer of ZrO_2. Cargnello *et al.*[46] reported enhanced metal-support interactions of $Pd@CeO_2$ gave exceptional activity in methane combustion compared with

supported Pd/CeO_2. The Pd cores of Pd@CeO_2 remained isolated even after heating the catalyst to 850°C.

Accordingly to previous results, there various features of core-shell material that play vital role in the catalytic activity (**Figure 11**), to mention only few, type of metal core and oxide shell, size of particles, shape of core-shell structure and synthetic procedure used for coating the oxide. Despite the great advancements in the metal core–shell catalysts field, several problems remain unsolved, which are as:

(1) Efficient synthesis procedures of the core–shell structure materials are still limited, and each technique can only be used to fabricate certain catalyst.

(2) The precise control of shell thickness and core size is still challenging.

(3) The mechanism of forming core-shell structure.

(4) The catalytic activity degrade by the shell-blocking effect when a precious metal core is covered by a dense shell.

These issues have restricted the use of the core–shell NPs and meanwhile it gives a lot of room for the extension of the designing of core–shell catalyst.

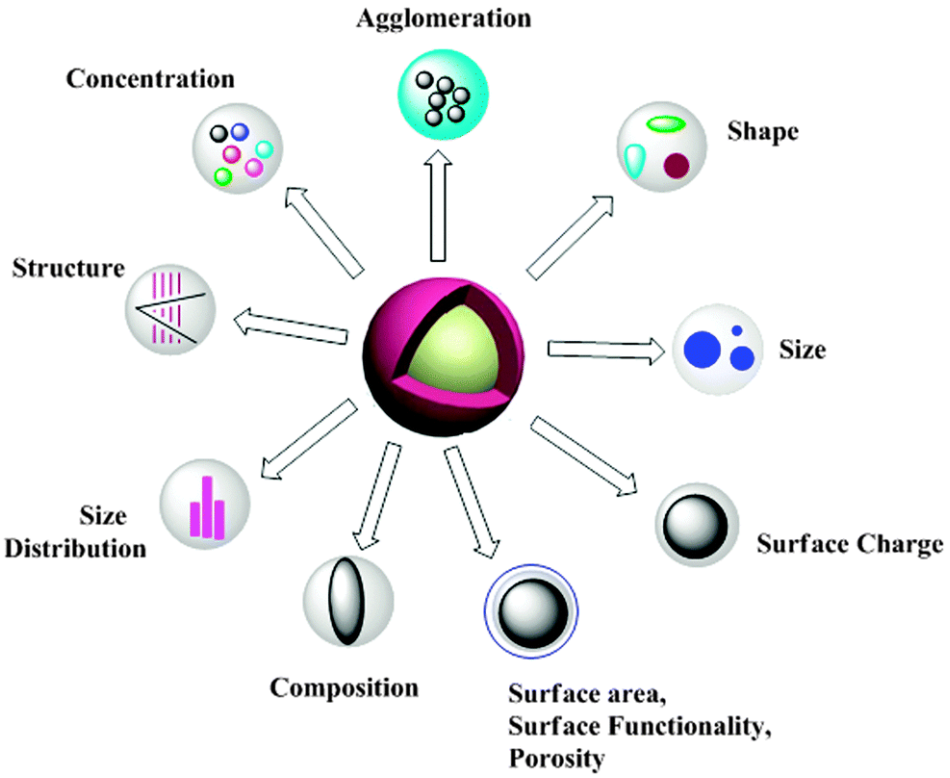

Figure 11. Structural of core-shell NPs and compositional features that can influence their catalytic properties[38]

1.3 Scope of my work

Embedded catalysts design via reverse micro-emulsion procedure for the suppression of catalyst deactivation by metal sintering for various applications such as CO oxidation and dry reforming of methane.

1.3.1 My strategy to overcome deactivation of catalysts by sintering

We want to utilize reverse micro-emulsion procedure to coat oxides layers of SiO_2, TiO_2 and ZrO_2 over metal NPs (Pt or Ni_9Pt) in order to form embedded catalysts. Isolating the metal NPs in a porous oxide layer are expected to prevent direct physical contact between the metals NPs that leads to their aggregation. This can maintain the size and active surface of metal NPs.

Detailed understanding of reverse micro-emulsion system must be done first and the parameters are affecting the formation of embedded catalysts should be determined. Thus, Pt@SiO_2 micro-emulsion system should be studied first, as a model catalyst to identify the effect of ageing time of Pt NPs, the time of adding the SiO_2 precursor, the concentration of Pt salts and water-to-surfactant ratio on the morphologies of the resultant Pt/SiO_2 NPs. Also, the effect of Pt/SiO_2 structure on the catalytic performance in CO oxidation reaction.

Next, we are interested to study the possibility of embedding Pt NPs with other oxides such as TiO_2 and ZrO_2 and the influence of such system on the catalytic activity of CO oxidation reaction.

Lastly, we want to apply the knowledge gained from the previous studies on a more challenging system and harsh catalytic reaction conditions, namely, bimetallic Ni_9Pt NPs and dry reforming of methane (DRM), respectively. Coating the bimetallic Ni_9Pt NPs with an oxide layer (TiO_2 or ZrO_2) and testing their thermal stability and sintering resistance during DRM reaction at 750°C.

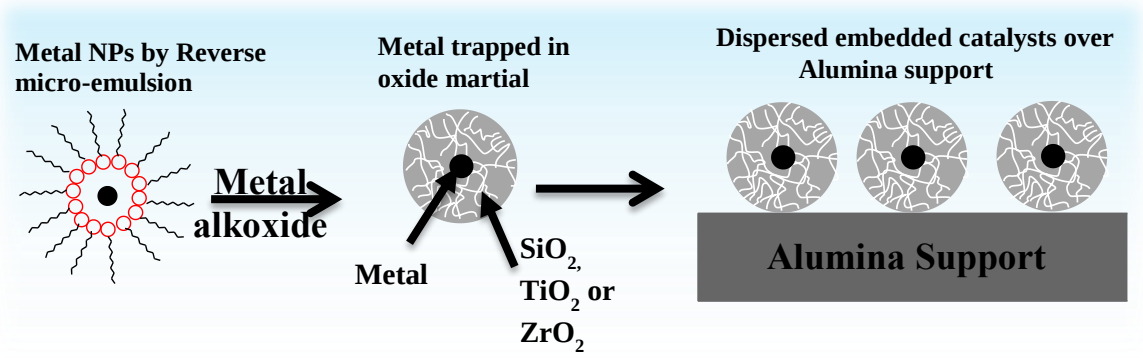

Figure 12. Scheme describes our strategy to overcome the sintering problem.

1.4 References

[1] R. Jin, in *Nanotechnology Reviews, Vol. 1*, **2012**, p. 31.
[2] C. Bartholomew, in *Kirk-Othmer Encyclopedia of Chemical Technology*, John Wiley & Sons, Inc., **2000**.
[3] M. E. Ali, M. M. Rahman, S. M. Sarkar, S. B. A. Hamid, *Journal of Nanomaterials* **2014**, *2014*, 23.
[4] S. Bagheri, N. Muhd Julkapli, S. Bee Abd Hamid, *The Scientific World Journal* **2014**, *2014*, 21.
[5] R. M. Rioux, H. Song, P. Yang, G. A. Somorjai, in *Metal Nanoclusters in Catalysis and Materials Science* (Eds.: G. Schmid, N. Toshima), Elsevier, Amsterdam, **2008**, pp. 149-166.
[6] R. Ghosh Chaudhuri, S. Paria, *Chemical Reviews* **2012**, *112*, 2373-2433.
[7] C. N. R. Rao, A. Müller, A. K. Cheetham, in *The Chemistry of Nanomaterials*, Wiley-VCH Verlag GmbH & Co. KGaA, **2005**, pp. 1-11.
[8] A. Henglein, *Chemical Reviews* **1989**, *89*, 1861-1873.
[9] L. Spanhel, H. Weller, A. Henglein, *Journal of the American Chemical Society* **1987**, *109*, 6632-6635.
[10] C. F. Hoener, K. A. Allan, A. J. Bard, A. Campion, M. A. Fox, T. E. Mallouk, S. E. Webber, J. M. White, *The Journal of Physical Chemistry* **1992**, *96*, 3812-3817.
[11] I. Honma, T. Sano, H. Komiyama, *The Journal of Physical Chemistry* **1993**, *97*, 6692-6695.
[12] H. S. Zhou, H. Sasahara, I. Honma, H. Komiyama, J. W. Haus, *Chemistry of Materials* **1994**, *6*, 1534-1541.
[13] H. Wang, L. Chen, Y. Feng, H. Chen, *Accounts of Chemical Research* **2013**, *46*, 1636-1646.
[14] F. Caruso, *Advanced Materials* **2001**, *13*, 11-22.
[15] J. R. Kitchin, J. K. Nørskov, M. A. Barteau, J. G. Chen, *Physical Review Letters* **2004**, *93*, 156801.
[16] W. Cha, N. C. Jeong, S. Song, H.-j. Park, T. C. Thanh Pham, R. Harder, B. Lim, G. Xiong, D. Ahn, I. McNulty, J. Kim, K. B. Yoon, I. K. Robinson, H. Kim, *Nat Mater* **2013**, *12*, 729-734.
[17] L. Adijanto, D. A. Bennett, C. Chen, A. S. Yu, M. Cargnello, P. Fornasiero, R. J. Gorte, J. M. Vohs, *Nano Letters* **2013**, *13*, 2252-2257.
[18] D. Wang, Y. Li, *Advanced Materials* **2011**, *23*, 1044-1060.
[19] J. Zhang, Y. Tang, K. Lee, M. Ouyang, *Nature* **2010**, *466*, 91-95.
[20] X. Yu, J. Wan, Y. Shan, K. Chen, X. Han, *Chemistry of Materials* **2009**, *21*, 4892-4898.
[21] L. Wang, C. Clavero, Z. Huba, K. J. Carroll, E. E. Carpenter, D. Gu, R. A. Lukaszew, *Nano Letters* **2011**, *11*, 1237-1240.
[22] X. Gong, S. Peng, W. Wen, P. Sheng, W. Li, *Advanced Functional Materials* **2009**, *19*, 292-297.
[23] S. Laurent, D. Forge, M. Port, A. Roch, C. Robic, L. Vander Elst, R. N. Muller, *Chemical Reviews* **2008**, *108*, 2064-2110.
[24] W. S. Seo, J. H. Lee, X. Sun, Y. Suzuki, D. Mann, Z. Liu, M. Terashima, P. C. Yang, M. V. McConnell, D. G. Nishimura, H. Dai, *Nat Mater* **2006**, *5*, 971-976.
[25] P. V. Kamat, B. Shanghavi, *The Journal of Physical Chemistry B* **1997**, *101*, 7675-7679.
[26] A. Mews, A. Eychmueller, M. Giersig, D. Schooss, H. Weller, *The Journal of Physical Chemistry* **1994**, *98*, 934-941.

[27] L. Qi, J. Ma, H. Cheng, Z. Zhao, *Colloids and Surfaces A: Physicochemical and Engineering Aspects* **1996**, *111*, 195-202.

[28] L. A. Fredin, Z. Li, M. A. Ratner, M. T. Lanagan, T. J. Marks, *Advanced Materials* **2012**, *24*, 5946-5953.

[29] N. V. Long, Y. Yang, C. Minh Thi, N. V. Minh, Y. Cao, M. Nogami, *Nano Energy* **2013**, *2*, 636-676.

[30] G. Huizhang, C. Yuanzhi, C. Xiaozhen, W. Ruitao, Y. Guang-Hui, P. Dong-Liang, *Nanotechnology* **2011**, *22*, 195604.

[31] J.-M. Yan, X.-B. Zhang, T. Akita, M. Haruta, Q. Xu, *Journal of the American Chemical Society* **2010**, *132*, 5326-5327.

[32] J.-H. Lin, V. V. Guliants, *Applied Catalysis A: General* **2012**, *445–446*, 187-194.

[33] Y. Chen, B. Zhu, M. Yao, S. Wang, S. Zhang, *Catalysis Communications* **2010**, *11*, 1003-1007.

[34] H. Peng, L. Xu, L. Zhang, K. Zhang, Y. Liu, H. Wu, P. Wu, *Journal of Materials Chemistry* **2012**, *22*, 14219-14227.

[35] J.-c. Qu, C.-l. Ren, Y.-l. Dong, Y.-p. Chang, M. Zhou, X.-g. Chen, *Chemical Engineering Journal* **2012**, *211–212*, 412-420.

[36] T.-Y. Chen, T.-J. M. Luo, Y.-W. Yang, Y.-C. Wei, K.-W. Wang, T.-L. Lin, T.-C. Wen, C. H. Lee, *The Journal of Physical Chemistry C* **2012**, *116*, 16969-16978.

[37] Q. Tan, C. Du, G. Yin, P. Zuo, X. Cheng, M. Chen, *Journal of Catalysis* **2012**, *295*, 217-222.

[38] M. B. Gawande, A. Goswami, T. Asefa, H. Guo, A. V. Biradar, D.-L. Peng, R. Zboril, R. S. Varma, *Chemical Society Reviews* **2015**, *44*, 7540-7590.

[39] W. Han, L. Yi, N. Zhao, A. Tang, M. Gao, Z. Tang, *Journal of the American Chemical Society* **2008**, *130*, 13152-13161.

[40] Z. Libor, Q. Zhang, *Materials Chemistry and Physics* **2009**, *114*, 902-907.

[41] M. Min, C. Kim, H. Lee, *Journal of Molecular Catalysis A: Chemical* **2010**, *333*, 6-10.

[42] A. Radi, D. Pradhan, Y. Sohn, K. T. Leung, *ACS Nano* **2010**, *4*, 1553-1560.

[43] H. H. Park, K. Woo, J.-P. Ahn, *Scientific Reports* **2013**, *3*, 1497.

[44] L. J. Lauhon, M. S. Gudiksen, D. Wang, C. M. Lieber, *Nature* **2002**, *420*, 57-61.

[45] M. Cargnello, N. L. Wieder, T. Montini, R. J. Gorte, P. Fornasiero, *Journal of the American Chemical Society* **2010**, *132*, 1402-1409.

[46] M. Cargnello, J. J. D. Jaén, J. C. H. Garrido, K. Bakhmutsky, T. Montini, J. J. C. Gámez, R. J. Gorte, P. Fornasiero, *Science* **2012**, *337*, 713-717.

[47] K. Hori, H. Matsune, S. Takenaka, M. Kishida, *Science and Technology of Advanced Materials* **2006**, *7*, 678-684.

[48] K. A. Dahlberg, J. W. Schwank, *Chemistry of Materials* **2012**, *24*, 2635-2644.

[49] S. Takenaka, H. Umebayashi, E. Tanabe, H. Matsune, M. Kishida, *Journal of Catalysis* **2007**, *245*, 392-400.

[50] Z. Li, L. Mo, Y. Kathiraser, S. Kawi, *ACS Catalysis* **2014**, *4*, 1526-1536.

[51] S. Takenaka, K. Hori, H. Matsune, M. Kishida, *Chemistry Letters* **2005**, *34*, 1594-1595.

[52] J. Wang, Z. H. Shah, S. Zhang, R. Lu, *Nanoscale* **2014**, *6*, 4418-4437.

[53] D. Zhang, X. Song, R. Zhang, M. Zhang, F. Liu, *European Journal of Inorganic Chemistry* **2005**, *2005*, 1643-1648.

[54] C. M. Y. Yeung, S. C. Tsang, *Journal of Molecular Catalysis A: Chemical* **2010**, *322*, 17-25.

[55] C. M. Y. Yeung, F. Meunier, R. Burch, D. Thompsett, S. C. Tsang, *The Journal of Physical Chemistry B* **2006**, *110*, 8540-8543.

[56] B. Liu, H. Xu, Z. Zhang, *Catalysis Communications* **2012**, *26*, 159-163.
[57] C. Destrée, J. B.Nagy, *Advances in Colloid and Interface Science* **2006**, *123–126*, 353-367.
[58] C. Tojo, D. Buceta, #xf3, M. A. pez-Quintela, *Journal of Nanomaterials* **2015**, *2015*, 10.
[59] F. J. Arriagada, K. Osseo-Asare, *Journal of Colloid and Interface Science* **1999**, *211*, 210-220.
[60] L. Yao, G. Xu, W. Dou, Y. Bai, *Colloids and Surfaces A: Physicochemical and Engineering Aspects* **2008**, *316*, 8-14.
[61] S. Thachepan, M. Li, S. A. Davis, S. Mann, *Chemistry of Materials* **2006**, *18*, 3557-3561.
[62] J. Eastoe, B. Warne, *Current Opinion in Colloid & Interface Science* **1996**, *1*, 800-805.
[63] L. M. Magno, D. G. Angelescu, W. Sigle, C. Stubenrauch, *Physical Chemistry Chemical Physics* **2011**, *13*, 3048-3058.
[64] I. Capek, *Advances in Colloid and Interface Science* **2004**, *110*, 49-74.
[65] R. Y. Parapat, V. Parwoto, M. Schwarze, B. Zhang, D. S. Su, R. Schomacker, *Journal of Materials Chemistry* **2012**, *22*, 11605-11614.
[66] Z. Yin, D. Ma, X. Bao, *Chemical Communications* **2010**, *46*, 1344-1346.
[67] H. P. Wu, J. F. Liu, M. Y. Ge, L. Niu, Y. W. Zeng, Y. W. Wang, G. L. Lv, L. N. Wang, G. Q. Zhang, J. Z. Jiang, *Chemistry of Materials* **2006**, *18*, 1817-1820.
[68] S. Nassos, E. E. Svensson, M. Nilsson, M. Boutonnet, S. Järås, *Applied Catalysis B: Environmental* **2006**, *64*, 96-102.
[69] T. Herranz, S. Rojas, M. Ojeda, F. J. Pérez-Alonso, P. Terreros, K. Pirota, J. L. G. Fierro, *Chemistry of Materials* **2006**, *18*, 2364-2375.
[70] T. Herranz, S. Rojas, F. J. Pérez-Alonso, M. Ojeda, P. Terreros, J. L. G. Fierro, *Applied Catalysis A: General* **2006**, *311*, 66-75.
[71] Z. You, I. Balint, K.-i. Aika, *Applied Catalysis B: Environmental* **2004**, *53*, 233-244.
[72] J. Eastoe, M. J. Hollamby, L. Hudson, *Advances in Colloid and Interface Science* **2006**, *128–130*, 5-15.
[73] M.-P. Pileni, *Nat Mater* **2003**, *2*, 145-150.
[74] M. A. López-Quintela, *Current Opinion in Colloid & Interface Science* **2003**, *8*, 137-144.
[75] M. A. López-Quintela, C. Tojo, M. C. Blanco, L. García Rio, J. R. Leis, *Current Opinion in Colloid & Interface Science* **2004**, *9*, 264-278.
[76] H.-K. Chiu, I. C. Chiang, D.-H. Chen, *Journal of NP Research* **2009**, *11*, 1137-1144.
[77] M.-L. Wu, D.-H. Chen, T.-C. Huang, *Chemistry of Materials* **2001**, *13*, 599-606.
[78] E. Larios, L. Calderón, K. Guerrero, E. Pinedo, A. Maldonado, J. Tanori, *Journal of Dispersion Science and Technology* **2012**, *33*, 1360-1367.
[79] Y. Wang, Y. Zhai, D. Pierre, M. Flytzani-Stephanopoulos, *Applied Catalysis B: Environmental* **2012**, *127*, 342-350.
[80] D.-S. Bae, Han, K.-S. and Adair, J. H., *Journal of the American Ceramic Society* **2002**, *85* 1321–1323.
[81] Y. Hu, Y. Wang, Z.-H. Lu, X. Chen, L. Xiong, *Applied Surface Science* **2015**, *341*, 185-189.
[82] S. H. Joo, J. Y. Park, C.-K. Tsung, Y. Yamada, P. Yang, G. A. Somorjai, *Nat Mater* **2009**, *8*, 126-131.

[83] A. Guerrero-Martínez, J. Pérez-Juste, L. M. Liz-Marzán, *Advanced Materials* **2010**, *22*, 1182-1195.
[84] M. Jae Kwon, H. Jung, J. Hoon Park, *Journal of Physics and Chemistry of Solids* **2012**, *73*, 1448-1451.
[85] Y. Yang, M. Y. Gao, *Advanced Materials* **2005**, *17*, 2354-2357.
[86] D. B. Zhang, H. M. Cheng, J. M. Ma, Y. P. Wang, X. Z. Gai, *Journal of Materials Science Letters*, *20*, 439-440.
[87] M. L. Viger, L. S. Live, O. D. Therrien, D. Boudreau, *Plasmonics* **2008**, *3*, 33-40.
[88] S.-H. Wu, C.-T. Tseng, Y.-S. Lin, C.-H. Lin, Y. Hung, C.-Y. Mou, *Journal of Materials Chemistry* **2011**, *21*, 789-794.
[89] C. H. Bartholomew, *Applied Catalysis A: General* **2001**, *212*, 17-60.
[90] A. K. Neyestanaki, F. Klingstedt, T. Salmi, D. Y. Murzin, *Fuel* **2004**, *83*, 395-408.
[91] J. Yang, V. Tschamber, D. Habermacher, F. Garin, P. Gilot, *Applied Catalysis B: Environmental* **2008**, *83*, 229-239.
[92] A. K. Datye, Q. Xu, K. C. Kharas, J. M. McCarty, *Catalysis Today* **2006**, *111*, 59-67.
[93] T. W. Hansen, A. T. DeLaRiva, S. R. Challa, A. K. Datye, *Accounts of Chemical Research* **2013**, *46*, 1720-1730.
[94] D. D. Beck, C. J. Carr, *Journal of Catalysis* **1988**, *110*, 285-297.
[95] P. Wynblatt, N. A. Gjostein, *Progress in Solid State Chemistry* **1975**, *9*, 21-58.
[96] U. Lassi, University of Oulu, Faculty of Technology (http://urn.fi/urn:isbn:9514269543), **2003**.
[97] J. A. Moulijn, A. E. van Diepen, F. Kapteijn, *Applied Catalysis A: General* **2001**, *212*, 3-16.
[98] K. C. Taylor, *Catalysis Reviews* **1993**, *35*, 457-481.
[99] H. Shinjoh, H. Muraki, Y. Fujitani, *Effect of severe thermal ageing on noble metal catalysts.*

In: Catalysis and Automotive Pollution Control II, Elsevier, Amsterdam, **1991**.
[100] R. M. J. Fiedorow, B. S. Chahar, S. E. Wanke, *Journal of Catalysis* **1978**, *51*, 193-202.
[101] H. S. A. de Sousa, A. N. da Silva, A. J. R. Castro, A. Campos, J. M. Filho, A. C. Oliveira, *International Journal of Hydrogen Energy* **2012**, *37*, 12281-12291.
[102] J. L. C. a. G. A. Fuentes, *Methods and Products, Dr. Volodymyr Shatokha (Ed.)* **2012**.
[103] B. Coq, in *Metal-Ligand Interactions in Chemistry, Physics and Biology* (Eds.: N. Russo, D. R. Salahub), Springer Netherlands, Dordrecht, **2000**, pp. 49-71.
[104] A. J. Forman, J.-N. Park, W. Tang, Y.-S. Hu, G. D. Stucky, E. W. McFarland, *ChemCatChem* **2010**, *2*, 1318-1324.
[105] L. Li, S. He, Y. Song, J. Zhao, W. Ji, C.-T. Au, *Journal of Catalysis* **2012**, *288*, 54-64.
[106] P. Jung-Nam, Z. Peng, H. Yong-Sheng, W. M. Eric, *Nanotechnology* **2010**, *21*, 225708.
[107] S. H. Joo, J. Y. Park, C. K. Tsung, Y. Yamada, P. Yang, G. A. Somorjai, *Nat Mater* **2009**, *8*, 126-131.
[108] J.-N. Park, A. J. Forman, W. Tang, J. Cheng, Y.-S. Hu, H. Lin, E. W. McFarland, *Small* **2008**, *4*, 1694-1697.
[109] S. Takenaka, Y. Orita, H. Umebayashi, H. Matsune, M. Kishida, *Applied Catalysis A: General* **2008**, *351*, 189-194.
[110] J. W. Han, C. Kim, J. S. Park, H. Lee, *ChemSusChem* **2014**, *7*, 451-456.

[111] J. T. Tompkins, R. Mokaya, *ACS Applied Materials & Interfaces* **2014**, *6*, 1902-1908.
[112] D. Pakhare, J. Spivey, *Chemical Society Reviews* **2014**, *43*, 7813-7837.
[113] K. An, Q. Zhang, S. Alayoglu, N. Musselwhite, J.-Y. Shin, G. A. Somorjai, *Nano Letters* **2014**, *14*, 4907-4912.
[114] P. M. Arnal, M. Comotti, F. Schüth, *Angewandte Chemie International Edition* **2006**, *45*, 8224-8227.

CHAPTER 2

2. Design of Core-Shell Pt-SiO_2 Catalyst in Reverse Micro-emulsion System: Distinctive Kinetics on CO Oxidation at Low Temperature

2.1. Introduction

Core-shell catalysts that consist of active metal particles surrounded by porous oxides have drawn much attention because of their enhanced catalytic activity and stability in water-gas shift reactions,[1-3] dry reforming of methane,[4-9] hydrocarbon oxidation,[10] electrocatalysis,[11-16] photocatalytic water-splitting,[17,18] and hydrogenation reactions.[19-21] A water-in-oil reverse micro-emulsion system consists of thermodynamically stable nano-sized aqueous micelles surrounded by self-assembled surfactant dispersed in an organic solvent.[22] These micelles work as nano-reactors to produce different types of nanomaterials without high pressure and high temperature. The confined space of the nano-reactor environment has the ability to produce mono-dispersed metal and alloy particles in principle smaller than the nanodroplets.[22] There are crucial parameters that play vital roles in this procedure, affecting the size, shape and stability of micelles and eventually the morphology of the synthesized materials.[22-25] These parameters are the surfactant and organic solvent type, water-to-surfactant molar ratio, and type and concentration of reactants.[22-25]

One of the most prominent advantages of the micro-emulsion technique is the possibility to perform sequential reactions using the confined environment by adding new reactants and reagents; e.g., the first reaction includes formation of the uniform seeds of metal particles (core), followed by adding other separate reactants to proceed to coat those cores (shell).[22] For instance, micro-emulsion methods were applied to fabricate an extra uniform layer of NPs with a very precise size control, forming different morphologies such as 'onion-like', 'yolk-shell', and core-shell structures.[26] Not only is the coating of an additional layer of metallic NPs on the primary metal possible by micro-emulsion, but also a metal oxide layer can be delicately added around the metal. Indeed, many metal NPs were protected against sintering at high temperatures by encapsulation within porous SiO_2,[26,27] CeO_2[1,3,28,29] or $Ce_xZr_{1-x}O_2$[28] forming core@shell structures prepared by micro-emulsion for different catalytic reactions.[30,31] Isolation of the metal NPs in an inert porous shell prevents the direct physical contact of the metals between themselves that leads to their aggregation, which can maintain the size and active surface of metal NPs.[32] The importance of the core-shell structure for high-temperature catalysis was emphasized by Joo et al., who used a Pt metallic particle core with mesoporous SiO_2 shell to protect metals from sintering while maintaining accessibility to the active metal surfaces.[20]

CO oxidation is our choice as a model reaction to test the synthesized materials because it has been widely studied owing to its industrial importance and relevance to environmental issues.[33] The reaction has been extensively reported for single-crystal Pt surfaces[34-39] and supported Pt NPs.[40-44] Two

distinct kinetic regimes were reported for CO-covered or CO-uncovered Pt surfaces, depending on the O_2/CO reactant ratio.[38] At low O_2/CO (around unity), the Pt surface is covered mostly with CO molecules (negative order in CO pressure).[42] Tremendous rate enhancement is measured once the O_2/CO ratio becomes larger than a threshold, where high CO coverage can no longer be maintained.[38,42] At such high O_2/CO, light-off behavior in which the rate of reaction improves drastically can be obtained without detectable CO coverage (positive order in CO). The other way to improve the CO oxidation rate is to use a reducible oxide such as CeO_2[45] or FeO_x[46] as a support. It is considered that mobile oxygens are provided by the reducible oxide which would react directly with CO at metal-support perimeter,[45] even if Pt surface is fully covered with CO at a steady state. The literature also discusses another method to improve the rate, which uses atomically-dispersed “single site” on oxidic support,[46-48] but these results are contradictory to other findings in which such sites offer CO-strongly bound sites and act as spectators.[43]

Herein, we report a detailed characterization on each individual synthesis step to identify the critical parameters during the multiple sequential synthesis steps for the formation of Pt@SiO_2 core-shell NPs using water-in-oil (w/o) micro-emulsions. Only NH_4OH was used for the formation of Pt colloids and the SiO_2 spheres, as reported by Kishida and co-workers.[10,27] No additional reducing agent such as N_2H_4 or $NaBH_4$ was used in this study, which allow metal hydroxide to grow slowly. These various synthesized materials were applied as catalysts for low-temperature CO oxidation reaction. Our current study reports a novel

approach to enhance the turnover rate of Pt by having a microporous SiO_2 shell covering the Pt particle core. Whereas conventional supported Pt NPs show negative order in CO (CO reversibly poisons the Pt surface at the steady state), the core-shell catalysts exhibit one order of magnitude higher rate and has a positive order with respect to the CO pressure. The characterization of the core shell structure is conducted regardless of whether the nature of Pt is altered or any other parameter, such as gas diffusion. Such effects of the Pt-SiO_2 structure on the catalytic performance of CO oxidation are discussed.

2.2. Material and methods

2.2.1 Chemicals

The surfactant used for this study was polyoxyethylene (5) nonylphenyl ether with 5 oxyethylene per molecule (known as NP5 or IGEPAL®CO-520, Sigma Aldrich). Cyclohexane was selected for this study as an organic solvent. The following chemicals were used as received: cyclohexane (GPR REACTAPUR®100%, VWR chemicals), ethanol (absolute ≥99.8%, Sigma Aldrich), platinum (IV) chloride (≥99.9%, Sigma Aldrich), tetraethyl orthosilicate (TEOS, 99.999% trace metals basis) and ammonium hydroxide solution (28% NH_3 in H_2O, ≥99.99% trace metals basis). Pt/Al_2O_3 pellets (micromeritics) were crushed to a fine powder and used as a standard for the CO oxidation reaction. γ-Al_2O_3 pellets (bimodal, Alfa Aesar) were crushed to a fine powder and calcined at 850 °C for 12 h before use, and γ-Al_2O_3 (PURALOX TH 100/150, Sasol) was

calcined at 900 °C for 24 h before use as diluent for the CO oxidation kinetic study. Milli-Q water (18.2 MΩ cm) was used.

2.2.2 Catalyst synthesis

The Pt@SiO_2 NPs were prepared by a reverse micro-emulsion method. Two sets of water-in-oil micro-emulsion solutions were prepared in a 250 ml round flask, and both contain 17.2 mg of NP5, 3.5 ml of water and 54 ml of cyclohexane, corresponding to an NP5/water/cyclohexane molar ratio of 1/4/17. Micro-emulsion solution I contains aqueous phase with 86.3 mg or 256 μmol of platinum (IV) chloride dissolved in 3.5 ml of water, and micro-emulsion solution II contains 3.5 ml of ammonia in aqueous phase (28%). Before mixing the two micro-emulsion solutions, they were separately stirred until a transparent mixture was obtained. The two micro-emulsion solutions were then mixed all at once (solution III). In the first part of the study, the aging time of Pt colloids was varied (immediate, 2 days and 1 week) before adding 1.2 ml of TEOS. The TEOS was then left to hydrolyze by stirring for 3 days.

For the second part of the study, varying thickness of the SiO_2 shell, the core-shell sample with 2 days aging was chosen with different TEOS amounts of 0.14, 0.3, 0.57 or 1.2 ml, which gives molar ratios of SiO_2/Pt = 2.5, 5, 10 and 20, respectively. The samples were stirred for 3 days to allow complete hydrolysis of TEOS to form SiO_2.

One Pt@SiO_2 sample was synthesized in a similar manner for 2 days of aging, with the same amounts of cyclohexane and NP5 but with 1 ml of water and 5 mg of Pt salt for solution I and 1.4 ml of ammonia in aqueous phase (28%) for solution II. The same amount of TEOS was used (1.2 ml).

Another Pt@SiO_2 sample exposed to immediate TEOS addition was further decorated with extra SiO_2 layer by adding additional 1.86 ml TEOS to the micro-emulsion solution containing Pt@SiO_2 species.

For the synthesis of supported Pt/SiO_2, SiO_2 spheres were first synthesized by adding 1.2 ml of TEOS to the micro-emulsion solution II and was left stirring for 3 days. Micro-emulsion solution I containing the Pt salts was then mixed with the abovementioned solution with the SiO_2 spheres with ammonia and left stirring overnight to form Pt colloids.

For the further characterization of the samples at this stage, the powder was separated by centrifuge and washed with ethanol three times. To prepare the γ-Al_2O_3-supported Pt@SiO_2 sample (total 1% Pt) for catalytic reaction, the resultant micro-emulsion solution III was added dropwise to 200 m of ethanol with 500 mg of γ-Al_2O_3 powder suspension in a 500 ml round-bottom flask. The mixture was stirred for 4 h and then separated by centrifuge and washed with ethanol twice.

Later, all obtained powder (with or without γ-Al_2O_3) was dried in the oven at 120 °C overnight. The samples were treated in a muffle furnace in static air at

500 °C for 1 h with a ramping rate of 1 °C min^{-1}. The reduction (4% H_2 in Ar) was performed in a tubular reactor at 250 °C for 1 h at a ramping rate of 1 °C min^{-1}.

For a reference sample, 0.5 wt% Pt/Al_2O_3 catalysts were obtained from Micromeritics (part number: 004/16825/00 Lot: SE10767).

2.2.3 Characterization

The samples were characterized by transmission electron microscopy (TEM) and scanning TEM (STEM) to study the structure and morphology of the NPs and obtain the Pt particle size distribution. TITAN ST (for STEM) and TITAN CT (FEI company), operated at 300 kV and 120 kV, respectively, were effectively used for imaging. The specimens were prepared by dispersing them in ethanol and placing them on the copper grid.

The X-ray diffraction (XRD) patterns of the catalysts were recorded after the reduction test on a Bruker DMAX 2500 X-ray diffractometer with Cu Kα radiation (λ = 0.154 nm).

N_2 physisorption was measured by using a Micrometrics ASAP 2420. The surface area and pore size distribution were calculated by the Brunauer–Emmett–Teller (BET) and density functional theory (DFT) methods, respectively. Before the measurements, the samples were degassed at 200 °C for 2 h.

X-ray photoelectron spectroscopy (XPS) studies were carried out in a Kratos Axis Ultra DLD spectrometer equipped with a monochromatic Al Kα X-ray

source (*hv* = 1486.6 eV) operating at 150 W, a multichannel plate and delay line detector under a vacuum of 1×10^{-9} mbar. The survey and high-resolution spectra were collected at fixed analyzer pass energies of 160 eV and 20 eV, respectively. Binding energies were referenced to the C 1s binding energy of adventitious carbon contamination, which was taken to be 284.8 eV. The data were analyzed with commercially available software, CASAXPS.

Inductively coupled plasma atomic emission spectroscopy (ICP-AES) - ICAP6500 Duo (Thermo Instruments) was conducted to measure the exact content of Pt. The solid samples (20-30 mg) were first digested in a mixture of (HF, HCl and HNO_3) at 180 °C for 25 min.

The Pt dispersion of the samples was estimated by the CO pulse chemisorption, assuming a CO/Pt stoichiometry of the unity. The sample was heated at 300 °C for 30 min with a ramping rate of 10 °C min^{-1} in a He flow. The sample was then cooled to 250 °C under He followed by exposure to 4% H_2 in Ar for 1 h. The gas was switched at 250 °C to He to remove the remaining H_2, and the sample was finally cooled to 40 °C before CO pulses were injected. The gas detection was carried out in a SHIMADZU GC-8A equipped with a thermal conductivity detector. The volume of the sample pulse loop was 250 µl containing 0.9% CO in He (92 nmol CO per pulse). The CO uptake was determined by the difference from the intact CO amount.

Diffuse-reflectance infrared Fourier transform (DRIFT) spectroscopy was used to monitor the infrared spectra of chemisorbed CO on catalysts during the

flow of 1% CO in Ar, 20 ml min^{-1} at 35 °C. Spectra (4000-650 cm^{-1}; 4 cm^{-1} resolution) were measured with a Nicolet 6700 FT-IR spectrometer using a Hg-Cd-Te (MCT-B) detector and 32 scan averages. Samples were pretreated in situ by flowing Ar with 20 ml min^{-1} flow at 300 °C for 30 min and then reduced at 250 °C for 1 h with a 20 ml min^{-1} flow of 10% H_2-in Ar.

2.2.4 Catalytic test

The CO oxidation reaction was conducted in a fixed bed reactor at atmospheric pressure. The gas detection for CO, O_2 and CO_2 was conducted using an Agilent technologies 3000A Micro GC. The Pt@SiO_2/Al_2O_3 catalyst bed was supported using quartz wool in a U-shaped quartz tube with an internal diameter of 4 mm. The catalyst was pretreated by flowing 10% O_2-90% He with 100 ml min^{-1} flow at 300 °C for 30 min with a ramping rate of 10 °C min^{-1}. The catalyst was then treated in 40% H_2-60% He with a 100 ml min^{-1} flow at 250 °C for 1 h. The catalyst was 14× diluted with Al_2O_3 (PURALOX TH 100/150, Sasol) to avoid a temperature increase due to this exothermic reaction.[61] The amount of catalyst was varied (2-10 mg) to maintain the CO conversion lower than 4%.

2.3. Results and Discussion

2.3.1 Control of Pt particle size within SiO_2 matrix and Pt/SiO_2 morphology

The typical synthesis protocol for a Pt core oxide shell structure in the literature involves the reduction of Pt salts by a reducing agent such as N_2H_4 or

$NaBH_4$.[30] The choice of reducing agent was critical to maintain both the stability of the micelles during the synthesis and the composition of the resultant Pt NPs. For instance, we observed a slight destabilization of the micelles when N_2H_4 was used as a reducing agent, which eventually led to the agglomeration of Pt NPs and affected the uniformity of their size. However, $NaBH_4$ can form the byproduct $NaBO_2$, which may cause poisoning of the metal surfaces.[49] In the first part of our study, we utilized ammonium hydroxide (NH_4OH) solution for the preparation of both Pt NPs (without introducing a reducing agent) and SiO_2 from TEOS. The detailed reaction steps are depicted in **Scheme 1**. In our synthesis, the $PtCl_4$ salt was dissolved in the water phase of *micro-emulsion* I, and the micelles containing NH_4OH aq. were prepared in *micro-emulsion* II. Once these two micro-emulsions were mixed, the pH was shifted to ~11, and finely dispersed Pt seeds were formed (*micro-emulsion* III). TEOS was added in different timing intervals (immediate, 2 days and 1 week, denoted as Pt@SiO_2(*time*)) to vary the size of the Pt seeds. **Figure 1 A-C** show transmission electron microscopy (TEM) images of the synthesized samples after drying at 120 °C. When TEOS was added immediately after the Pt seeds were formed, very fine NPs (~0.7 nm) were captured within SiO_2 matrix and were supported on the SiO_2 spheres. After 2 days of aging, the multicore Pt species in the SiO_2 shell started to be formed with fine Pt species (~2 nm) dispersed within the SiO_2 matrix. Further aging of 1 week led to mostly aggregated multicore Pt species in the core of SiO_2 shell, all of which have relatively similar particle sizes (~2 nm). The sample also contained some

unprotected Pt outside the SiO_2 layer. Regardless of aging time, a SiO_2 sphere with a diameter of 25-30 nm was obtained.

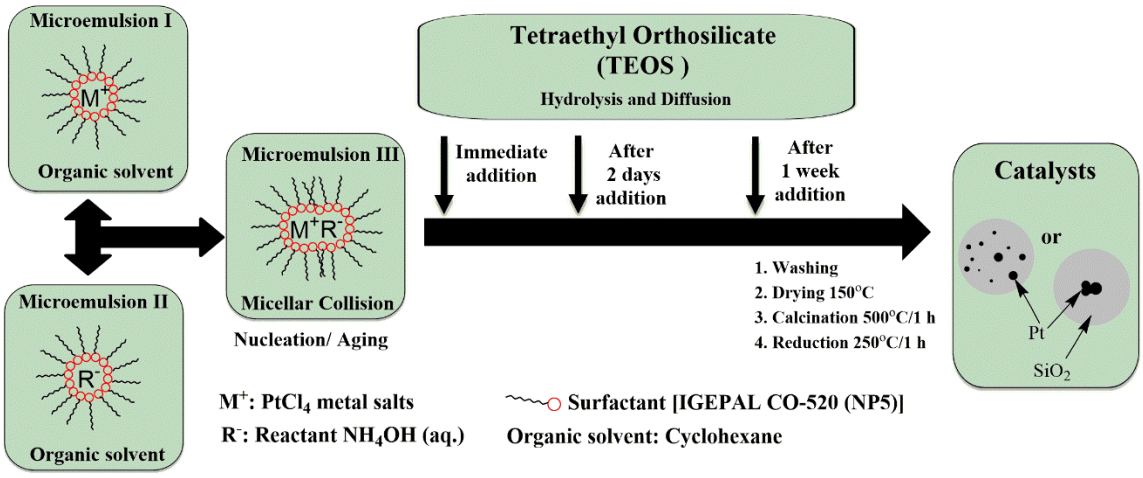

Scheme 1. General synthesis scheme using the reverse micro-emulsion system applied in this study.

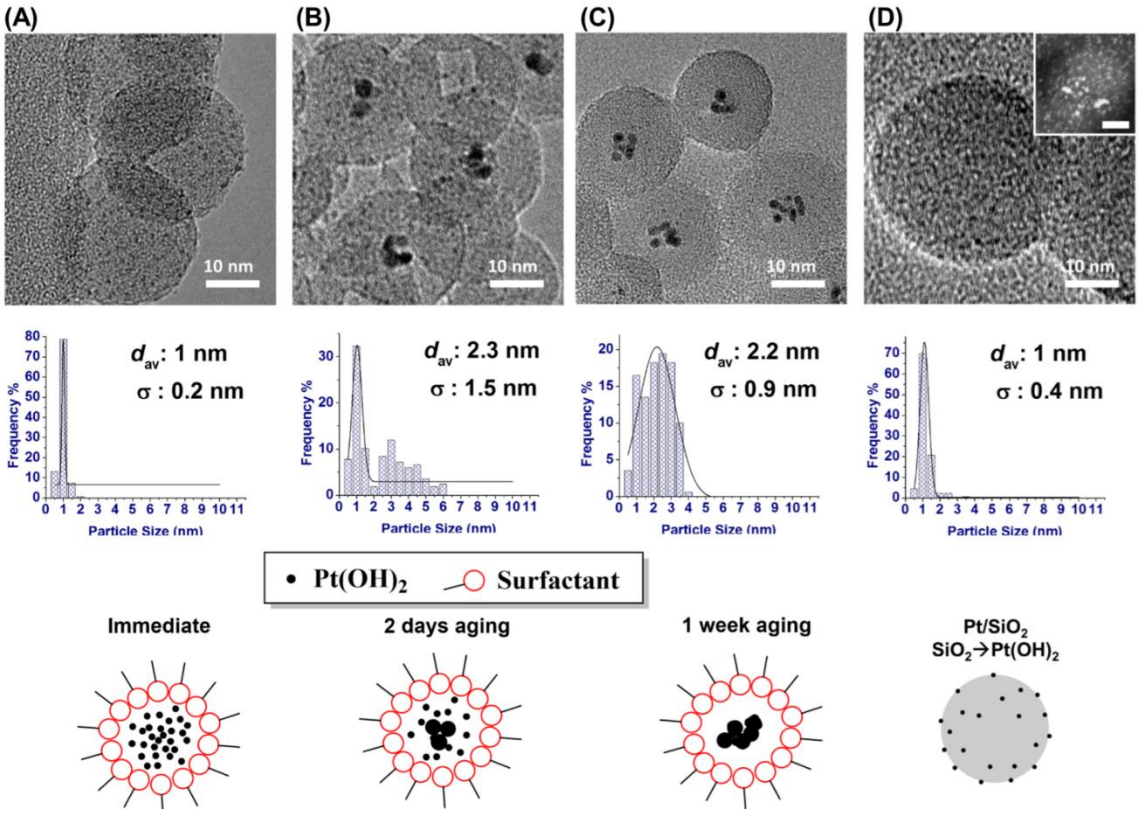

Figure 1. High-resolution TEM images of as-prepared samples together with histogram of particle size distribution and schematic images for (A) Pt@SiO_2(immediate), (B) Pt@SiO_2(2 days), (C) Pt@SiO_2(1 week), and (D) Pt/SiO_2.

Next, these samples were subjected to thermal treatment under static air at 500 °C for 1 h to remove organic residue. TEM and STEM images of the samples are shown in **Figure 2** in the supporting information. The average Pt size for the Pt@SiO_2(immediate) was ~2 nm. Most of the Pt NPs embedded within the SiO_2 matrix maintained small particle sizes of ~1 nm, and there were a few supported particles that became 4-6 nm at the outer surface of SiO_2. Regarding the Pt@SiO_2(2 days), the multicore species (each core below <1 nm) was transformed into one crystalline Pt NP of approximately 4 nm in average size and

~10 nm in SiO_2 shell thickness. The Pt@SiO_2(1 week), which had more Pt aggregates inside the SiO_2 core, produced a larger Pt NP of approximately 6 nm in the core. In addition, large Pt NPs (7-20 nm) outside the SiO_2 spheres were also observed. The SiO_2 thickness of ~10 nm did not change with the thermal treatment.

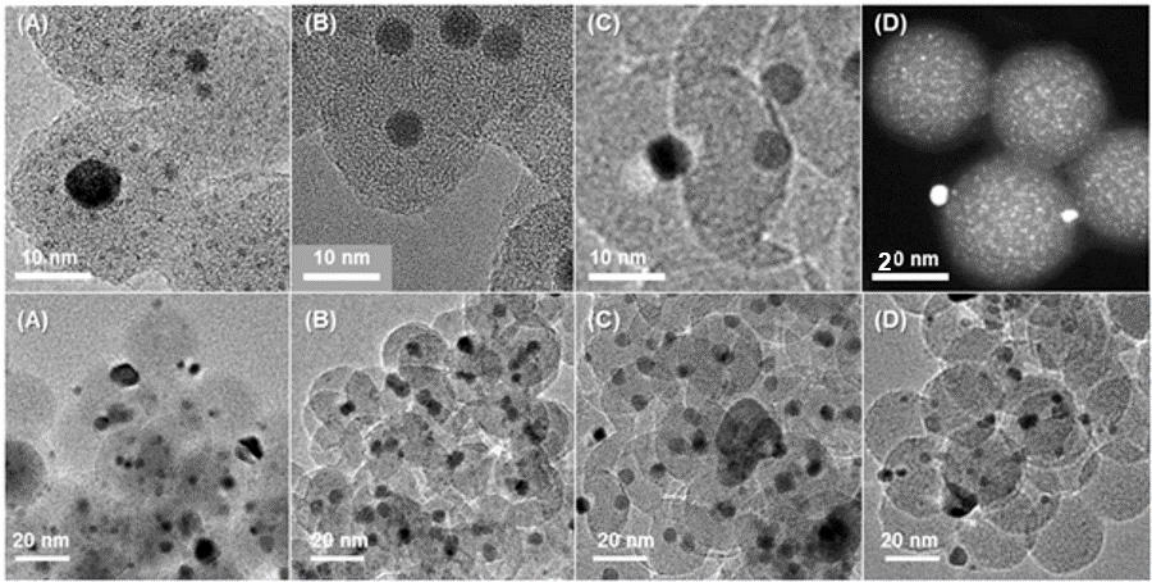

Figure 2. High-resolution TEM and scanning TEM images of samples treated at 500°C in two different scales for (A) Pt@SiO_2(immediate), (B) Pt@SiO_2(2 days), (C) Pt@SiO_2(1 week), and (D) Pt/SiO_2.

The oxidized samples were subsequently treated in diluted H_2 at 250 °C. TEM images of these reduced samples are shown in **Figure 3 A-C**. The aggregated Pt particles were formed outside the SiO_2 spheres for the Pt@SiO_2(immediate). The Pt@SiO_2(2 days) maintained its core-shell structure, in which most of the Pt NPs with a size of ~4 nm were encapsulated in the SiO_2 sphere. Some void space was apparent between the Pt particle and the SiO_2 core,

and it likely formed as a result of Pt hydroxide reduction to the metallic state, which reduces its volume. For the Pt@SiO_2(1 week), the core shell structure was similarly obtained with most of the particles, but some aggregated Pt particles were also observed as already evident from the sample before the reduction (**Figure 2C**). Consequently, a broad particle size distribution (between 1.5 and 10 nm) was obtained for this sample owing to a combination of supported Pt NPs and embedded Pt NPs within the SiO_2 matrix. The SiO_2 size was not significantly affected by the reduction treatment.

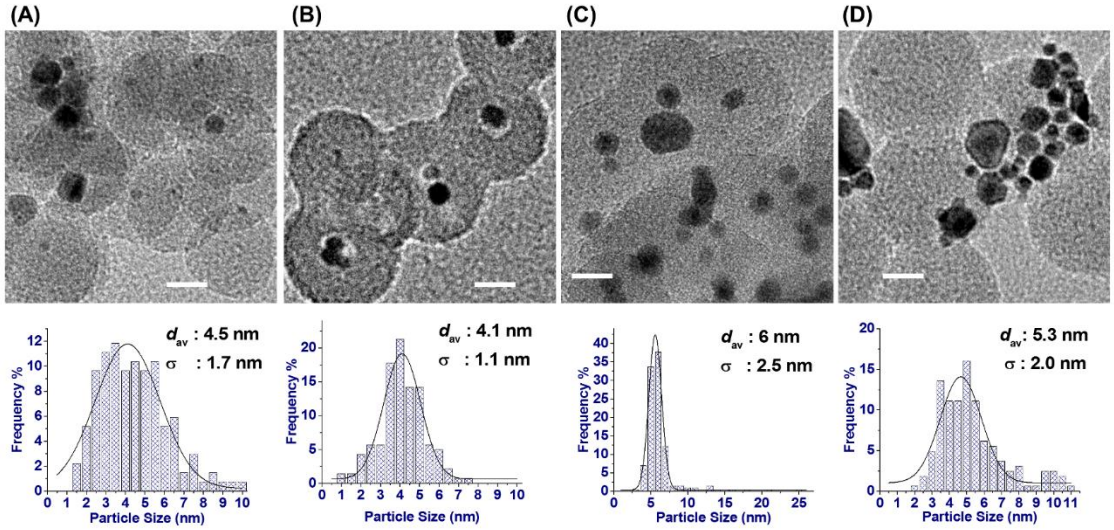

Figure 3. High-resolution TEM images of the samples reduced at 250 °C together with histogram of particle size distribution for (A) Pt@SiO_2(immediate), (B) Pt@SiO_2(2 days), (C) Pt@SiO_2(1 week), and (D) Pt/SiO_2. Scale bar: 10 nm.

For comparison, supported Pt species on SiO_2 spheres were synthesized by preparing first the SiO_2 spheres followed by the Pt colloid deposition in the same micro-emulsion condition using the same quantity of Si and Pt precursors

(denoted as Pt/SiO_2). By this method, Pt NPs embedded within the SiO_2 matrix can be avoided, and all Pt NPs are to be supported on the SiO_2 surface. **Figures 1-3 (D)** show TEM images of the sample as synthesized and reductive treatment, respectively. SiO_2 spheres with an average diameter of ~30 nm were uniformly obtained, consistent with the size obtained for the Pt@SiO_2 samples. Highly dispersed Pt species (as small as 1 nm) were formed on the SiO_2 spheres before and after oxidative treatment at 500 °C; however, the Pt particles experienced severe sintering after reduction at 250 °C with particle size of approximately 10 nm.

The synthesized samples at different stages were characterized by X-ray photoelectron spectroscopy (XPS). **Figure 4** shows XPS spectra of Pt 4f, O 1s, C 1s and Si 2p for the Pt@SiO_2(immediate) as representative data at each treatment step. The spectrum for the sample before heat treatment shows only Pt^{2+} peaks at 72.8 eV, which are assignable to $Pt(OH)_2$ phase.[71] The very minor peak for Pt^{4+} at 75 eV was observed, corresponding to PtO_2 species.[50] This result suggests that the particle growth of Pt at different aging times was as a consequence of the relatively slow agglomeration process of $Pt(OH)_2$ in the scale of days. After heat treatment, a large Pt^0 peak at 70.7 eV was observed, indicating the formation of metallic Pt state,[50] along with a decrease in the Pt^{2+} signal accompanied by a slight increase in PtO_2.[50] It is considered that heat treatment even in air led to disproportionation of $Pt(OH)_2$ into Pt^0 and a small quantity of PtO_2. Further reduction led to a predominant peak of metallic Pt with a further

decline of Pt^{2+} and Pt^{4+} peaks; however, these species were still present, possibly because of the adsorption of O_2 when the samples were exposed to air.

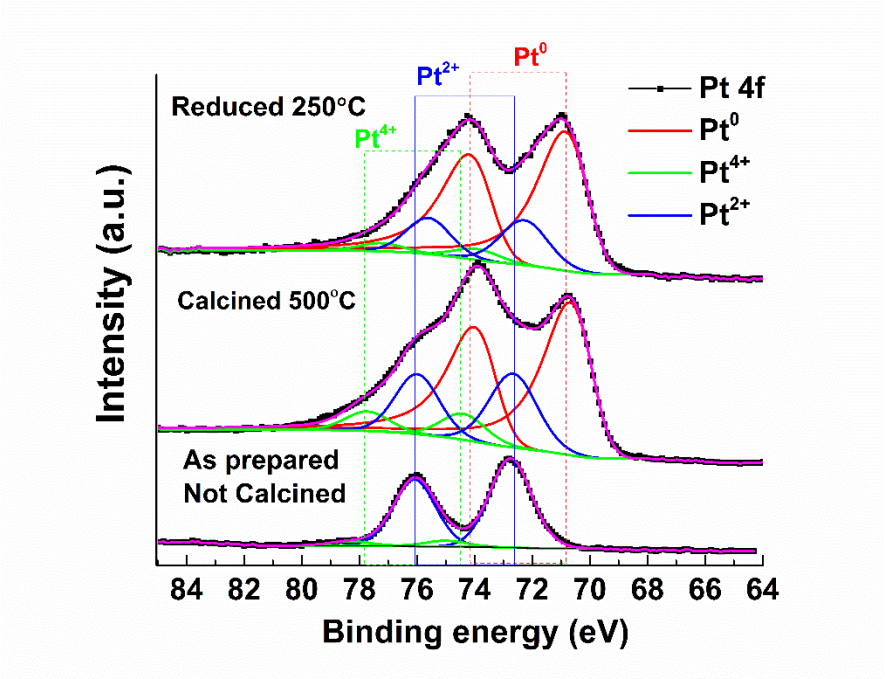

Figure 4. XPS spectra of Pt 4f for Pt@SiO_2(immediate) as a representative after each treatment.

X-ray diffraction (XRD) was performed on the as-prepared and reduced Pt@SiO_2 particles with varying time of Pt aging. For all samples before heat treatment, no apparent peaks were observed (thus, the figure is omitted), which is consistent with the lack of crystalline structures of $Pt(OH)_2$ and SiO_2 in the samples. For the reduced samples (**Figure 5**), the peaks located at 2θ = 39.7, 46 and 67.6 correspond to the (111), (200) and (220) Pt crystal planes, respectively, for the face-centered cubic (fcc) structure.[51] The formation of metallic Pt is

consistent with XPS data (**Figure 4**). The average crystallite sizes of Pt were estimated from (111) diffraction using Scherrer's equation, and the results are listed in **Table 1**. A similar crystallite size (~5.6 ± 0.4 nm) that can be detected by XRD was obtained. This average crystallite size was consistent with the statistics from counting the Pt size in the more than 150 particles (**Figures 3**).

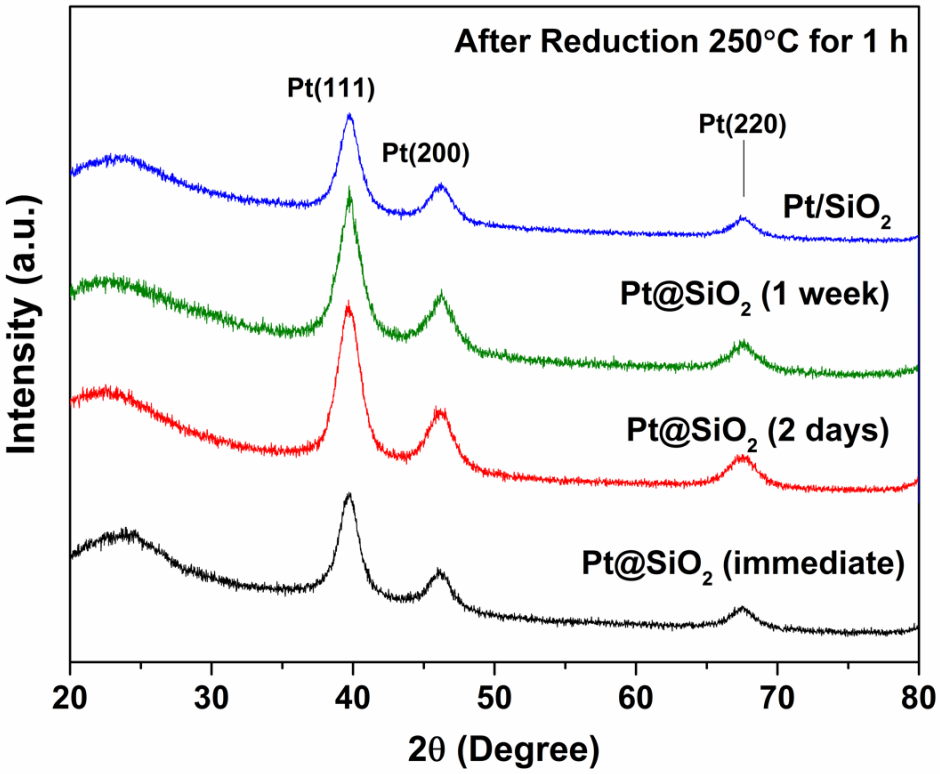

Figure 5. XRD patterns for various samples reduced at 250 °C.

There are also other factors that change thickness of SiO_2 layer, the morphology of Pt@SiO_2, including water content, H_2O/NP5 ratio, and Pt salt concentration. The additional results with different SiO_2 thickness, different H_2O/NP5 and additional SiO_2 coating on the Pt/SiO_2 sample are discussed further in the coming sections. Overall, the setting of such reaction conditions leads to a

highly reproducible synthesis protocol and resultant synthesized materials ($Pt@SiO_2$) in terms of dimensions and morphology.

2.3.2 Control of SiO_2 thickness in the core-shell Pt-SiO_2 structure

We examined the effects of the amount of added TEOS on the SiO_2 shell thickness of the $Pt@SiO_2$ NPs. The $Pt(OH)_2$ aging time was fixed for 2 days before adding TEOS to obtain the core-shell structure. The amounts of surfactant, solutions and Pt (50 mg) were maintained for all samples, but the amount of TEOS was varied to give SiO_2/Pt molar ratios of 2.5, 5, 10 and 20. **Figure 6** shows the TEM images of the synthesized samples. For the SiO_2/Pt molar ratio of 2.5, the thin SiO_2 shell with thickness of approximately 3 nm was observed, as were Pt particles without attaching SiO_2. For the SiO_2/Pt molar ratio of 5, the thickness of SiO_2 shell was increased to 6 nm, and all of the observed Pt particles were covered by the SiO_2. With further increases in the SiO_2/Pt molar ratio to 10 and 20, gradual growth of the SiO_2 shell was achieved with thicknesses of 7 and 10 nm, respectively. While varying the SiO_2 thickness, the size of Pt NPs was maintained at a similar level (~5 nm), indicating that the primary size of the Pt was determined in the process before the TEOS addition, as thoroughly discussed in the previous section. The different timescale of this synthesis for $Pt(OH)_x$ aggregation and SiO_2 particles enables us to synthesize various $Pt@SiO_2$ in a highly controllable manner.

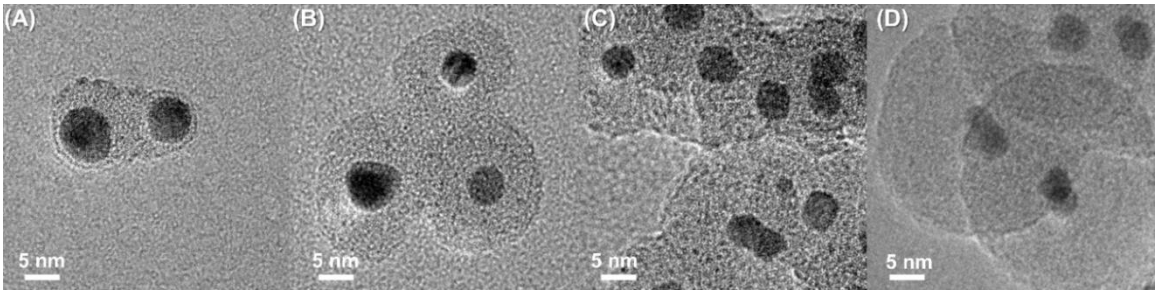

Figure 6. High-resolution TEM images of Pt@SiO_2(2 days) after oxidative treatment at 500 °C with various Si/Pt precursor molar ratios of (A) 2.5, (B) 5, (C) 10, and (D) 20 (corresponding sample shown in **Figure 2B**).

2.3.3 Effects of water and Pt content on the core-shell structure

One Pt@SiO_2 sample was synthesized in a similar manner for 2 days of aging, with the same amounts of cyclohexane and NP5 but with 1 ml of water (a H_2O/NP5 ratio from 4 to 1.4) and 5 mg of Pt salt (instead of 50 mg) for solution I and 1.4 ml of ammonia in aqueous phase (28%) for solution II. The same amount of TEOS was used (1.2 ml). A TEM image of the synthesized sample after heat treatment at 500°C for 1 h is shown in **Figure 7**. Under this new condition, the size of Pt NPs did not change drastically (~4 nm), and a similar structure of the Pt@SiO_2 core-shell NPs was present. Interestingly, some of the SiO_2 spheres without Pt NPs in the core were observed. These Pt@SiO_2 and SiO_2 sphere NPs seemed to be effectively separated as a result of reduced number of micelles in the micro-emulsion system. In summary, the low H_2O/NP5 ratio led to a reduced number of micelles. Previous and extensive studies were conducted on changing the size of SiO_2 by varying the H_2O/NP5 ratio, and the controversial result remains to predict the precise size of the SiO_2 spheres.[S1-S5] The fact that Pt particles had the same

size after the same aging time (2 days) suggests that a given aging time led the aggregation of $Pt(OH)_2$ colloids in a similar manner. Lowering the Pt amount in the system is considered to reduce the number of such aggregates, so not all of the micelles contain Pt colloids after aging. The remaining micelles without Pt colloids led to the formation of SiO_2 spheres.

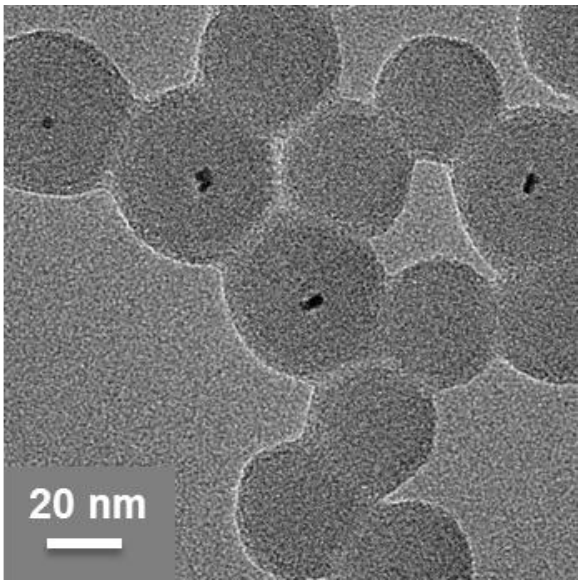

Figure 7. High-resolution TEM images of $Pt@SiO_2$(2 days) with different H_2O and Pt contents mentioned above.

2.3.4 Decorating an additional layer of SiO_2 on supported Pt/SiO_2 NPs

Another $Pt@SiO_2$ sample exposed to immediate TEOS addition was further decorated with extra SiO_2 layer by adding additional 1.86 ml TEOS to the micro-emulsion solution containing $Pt@SiO_2$ species. Supported Pt NPs decorated on an outer surface of SiO_2 spheres were subjected to sintering when the sample was reduced at high temperatures (**Figures 2A**, **8A** and **3A**). We employed an

additional thin SiO_2 layer with controlled thickness to avoid sintering of the Pt particles. We utilized the knowledge from the results: The diameters of the SiO_2 spheres obtained from 1.2 ml TEOS addition were consistently ~30 nm, as observed in the TEM images. In this part of the study, we targeted the formation of an extra layer of SiO_2 with 5 nm thickness on 30 nm SiO_2 spheres. A scheme in **Figure 8** illustrates the deposition of an additional layer of SiO_2. **Figure 8A** (the image corresponding to the sample shown in **Figure 2A**) shows the high resolution TEM image of the Pt/SiO_2 NPs without the SiO_2 layer, and **Figure 8B** shows a scanning TEM image of the Pt/SiO_2 NPs with the additional 5-nm-thick layer of SiO_2 both after heat treatment at 500°C. It can be noted from the images (compare **Figure 8A** and **B**) that the unprotected Pt particles went through sintering (~2 nm) upon thermal treatment; however, the additional SiO_2 layer protected the Pt particle from agglomeration (1.1 ± 0.2 nm). This confirms that the one-pot synthesis of SiO_2@(Pt/SiO_2) in the same micro-emulsion system can be achieved to form various Pt NP sizes, its dispersion in SiO_2 matrix, and further protection with additional SiO_2.

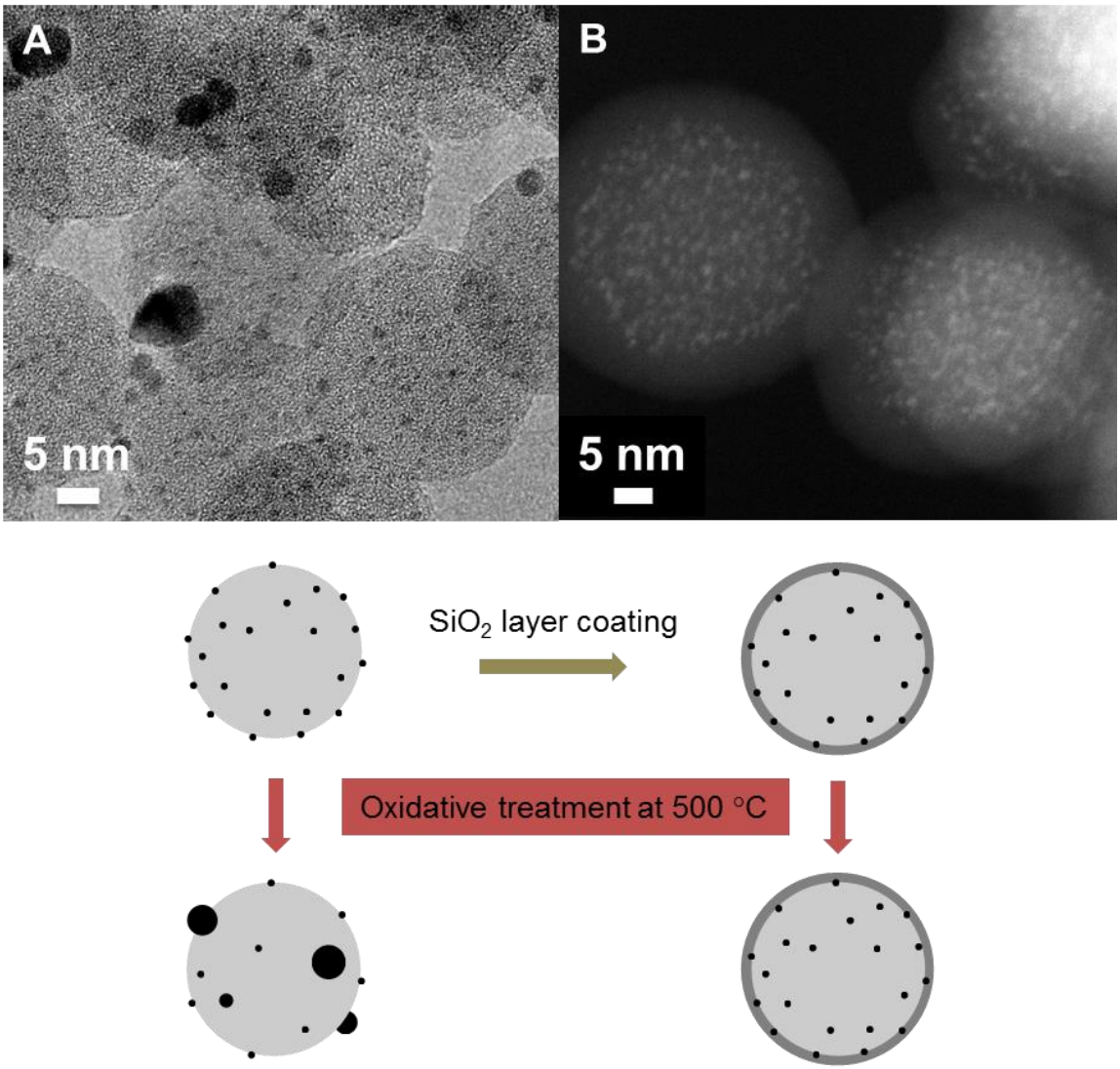

Figure 8. High-resolution TEM and scanning images of Pt@SiO_2(immediate) with and without additional SiO_2 coating mentioned above.

In summary, the structural evaluation of $Pt@SiO_2$ NPs can be described as follows: the ultrafine mono-dispersed $Pt(OH)_2$ seeds (below <1 nm) were rapidly formed in the first stage, when the two micro-emulsion solutions of $PtCl_4$ salts and ammonium aq. solution were mixed. Aggregation of these $Pt(OH)_2$ colloids occurs in the timescale of days. An increase in the aging time accumulates more aggregated seeds in the micelles, whereas fine particles remain dispersed elsewhere inside the micelles. Subsequently, the hydrolysis of TEOS is initiated at the interface of the micelles, rapidly generating hydrophilic species.[52] The TEOS addition at different timing intervals will protect such $Pt(OH)_2$ aggregates, resulting in different $Pt@SiO_2$ samples with various Pt sizes.

2.3.5 Accessibility of Pt surface in $Pt@SiO_2$ nanostructures

The porosity of the $Pt@SiO_2$ core shell structure was investigated using N_2 physisorption for $Pt@SiO_2$(immediate) and (2 days) samples. The BET surface areas were 109 and 105 $m^2\ g^{-1}$ for $Pt@SiO_2$(immediate) and (2 days) after calcination at 500 °C, respectively**. Figure 9** shows N_2 isotherm and inset shows pore size distribution using density functional theory interpretation. H_2 treatment at 250 °C caused slight reduction of the surface area for $Pt@SiO_2$(2 days) (93 $m^2\ g^{-1}$). Mesoporous nature (6–30 nm) is unambiguously assigned to inter-particle voids, consistent with the TEM image shown in **Figure 3B**. The presence of the microporous feature for the structure was evident (~1.4 nm) from the N_2 isotherm results, which may provide gas-permeation capability accessibility to the metal

core through the shell layer. The formation of such micropore within SiO_2 layer (~1 nm) was also reported in the literature.[26]

Table 1. Measured properties of Pt in various catalysts.

Sample	Crystallite size[a] [nm]	Pt particle size (TEM) [nm]	%D[b] CO chem. (TEM)	Pt loading[c] [wt%]
Immediate	5.9	4.5±1.7	12 (17)	0.72
2 days	5.2	4.1±1.1	26 (22)	0.60
1 week	5.9	6.0±2.5	11 (11)	0.52
Pt/SiO_2	6.1	5.3±2.8	8 (15)	0.71
Pt/Al_2O_3	-[d]	1.8±0.6	35 (52)	0.50

[a] Estimated from Pt(111) XRD diffraction peak. [b] Dispersion measured by CO pulse chemisorption and (TEM using %D = 100/(particle size in nm). [c] Pt loading in Al_2O_3-supported $Pt@SiO_2$ samples used for CO oxidation. [d] XRD pattern of the Al_2O_3 peak overlapped with Pt(111) diffraction peak, not enabled to estimate the crystallite size.

To make a catalyst bed using $Pt@SiO_2$ NPs with different aging times, the $Pt@SiO_2$ NPs were dispersed on Al_2O_3 as described in the Experimental section. The metal loading of Pt measured by inductively coupled plasma (ICP) and CO pulse chemisorption results for $(Pt@SiO_2)/Al_2O_3$ are shown in **Table 1.** The

immediate TEOS addition sample had 12% metal dispersion, corresponding to the existence of large Pt NPs (>6 nm) outside the shell and small ones (<2 nm) within the SiO_2 matrix (**Figure 3A**). The Pt@SiO_2(2 days) had the high Pt dispersion (26%), which is due to the small Pt NPs (~4 nm) inside the SiO_2 shell without forming aggregated particles outside the shell (**Figure 3B**). This CO chemisorption capacity proves that the Pt is accessible through the SiO_2 shell. The Pt@SiO_2(1 week) had lower dispersion (11%), which is probably due to the presence of large, unprotected Pt (>6 nm) NPs outside the SiO_2 shell (**Figure 3C**). The Pt/SiO_2 spheres had the lowest dispersion (8%) because all Pt NPs were unprotected and subjected to sintering upon the reduction treatment (**Figure 3D**). The bench-marking Pt/Al_2O_3 sample had highest dispersion of 35% from CO chemisorption measurement. In all cases, metal dispersions estimated from particle diameters measured from TEM images are generally consistent with CO chemisorbed values, indicating that the most of the metal surfaces observed in TEM images are accessible.

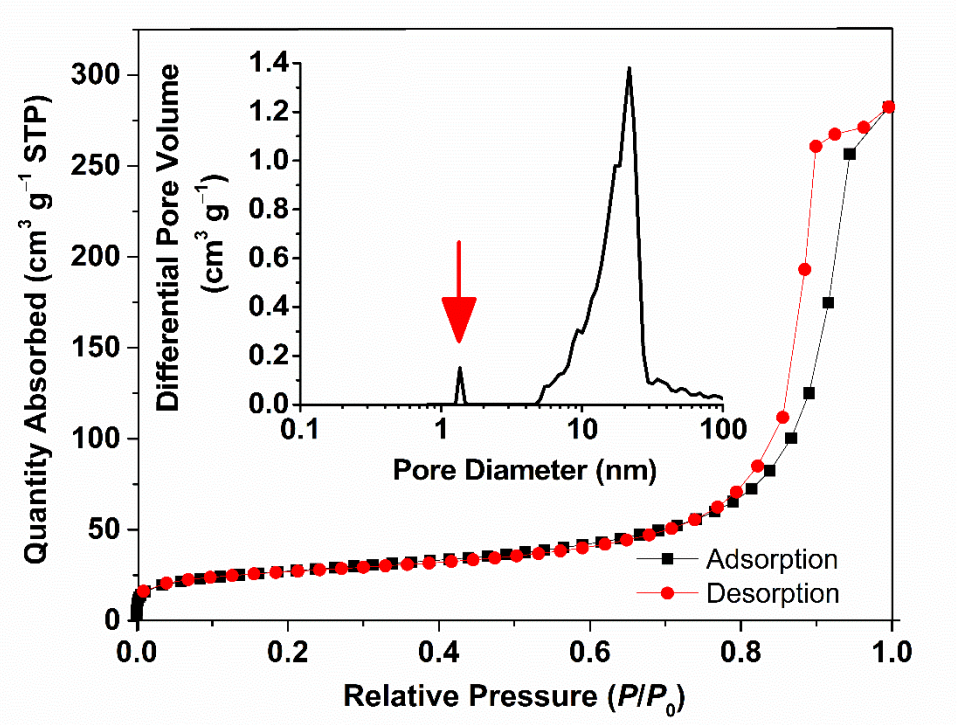

Figure 9. N_2 isotherm and pore size distribution for Pt@SiO_2 (2 days) reduced at 250 °C. The red arrow in inset points at microporous feature.

2.3.6 Low-temperature CO oxidation using Pt@SiO_2 catalysts

Low-temperature CO oxidation was carried out using the Pt@SiO_2, Pt/SiO_2 and Pt/Al_2O_3(reference) catalysts. The catalysts were 14 times diluted with inert Al_2O_3 to avoid influence on the kinetics by the reaction exotherms.[42] **Figure 10A** and **B** shows turnover frequency (TOF) as a function of CO pressure or O_2 pressure, respectively, measured at 170 °C. The results can be classified into two groups of catalysts: the first contains Pt@SiO_2 (2 days) and (1 week), which have clear Pt NPs covered with SiO_2 (*core-shell*), and the second group involves Pt@SiO_2 (immediate), Pt/SiO_2, and Pt/Al_2O_3, i.e., Pt NPs supported on

irreversible oxides (*supported*). The TOF of the *core-shell* samples was one order of magnitude larger than that of the *supported* samples. Table 2 summarizes the kinetic orders of the samples. The kinetics for the *supported* sample were of the negative first order with respect to CO and the positive first order with respect to O_2, which is consistent with the mechanism proposed in the literature, exhibiting O_2 interacting with the CO-covered surface.[53] Comparable TOF with similar pressure dependencies were observed for Pt/SiO_2 and $Pt@SiO_2$(immediate) on which Pt was decorated outside SiO_2. In contrast, the core-shell samples ($Pt@SiO_2$(2 days) and $Pt@SiO_2$(1 week)) exhibit much higher rates and positive orders in both CO and O_2 pressures. This positive orders in CO and O_2 suggests that the Pt surface is not fully covered with CO molecules, which is consistent with the typical Langmuir-Hinshelwood rate where the coverage denominator terms are non-negligible for both CO and O_2.[33] To the best of our knowledge, this rate enhancement due to the irreducible oxide coating of Pt NPs has never been observed. The Arrhenius plot is shown in **Figure 10C** for the various catalysts. It was confirmed that the TOF for the core-shell samples was nearly one order of magnitude higher than the supported samples. The activation energies were also consistently slightly lower for core-shell samples than for the supported ones, likely because of the different coverage and resultant reaction mechanism.[33] On the basis that the comparable Pt loading was used to be ~0.5-0.7 wt% for all samples investigated (Table 1), different metal dispersion (Table 1) does not account for the difference in rates; e.g., Pt/Al_2O_3 possessed higher metal

dispersion (35%) than did the *core-shell* samples (26% and 11% for Pt@SiO_2(2 days) and (1 week), respectively) but CO oxidation was slower on Pt/Al_2O_3.

Next, we discuss the possibility of enhanced activity with *core-shell* samples over *supported* samples. The first possible cause is that the samples contain totally different natures of Pt active sites that leads to different CO coverage at the steady state. To elucidate the Pt nature, infrared (IR) spectroscopy was conducted using CO as a probe molecule and the spectra are shown in **Figure 11**. In the literature, the detailed characterization on the nature of the Pt active sites was accomplished using the CO-IR data.[40,42,54] At high coverage of CO on Pt, linearly adsorbed CO is prevalent, the peak positions of which reflect the Pt particle size significantly influenced by dipole-dipole coupling of adsorbates, although the single-tone frequency is found to be similar among different particle sizes.[42] Larger particles (low Pt dispersion) lead to sharper CO peaks at higher wavenumbers (~2090 cm^{-1}) as a consequence of strong dipole coupling, whereas smaller particles lead to broader CO peaks at relatively lower wavenumbers (<~2080 cm^{-1}).[42] For the highly dispersed “single site” Pt, it was reported that the CO peak appears to show even higher wavenumbers (>~2100 cm^{-1}).[46,48] This was unambiguously attributed to CO adsorption strongly interacted with oxygen species on the small Pt active sites.[54] This study lacks evidence of such high wavenumber peaks, especially for the core-shell samples, which is consistent with the lack of highly dispersed Pt “single-sites” in TEM images (**Figure 3**). From this consideration, it is unlikely that the *core-shell*

samples possess single-site Pt that account for differences in CO oxidation activity.

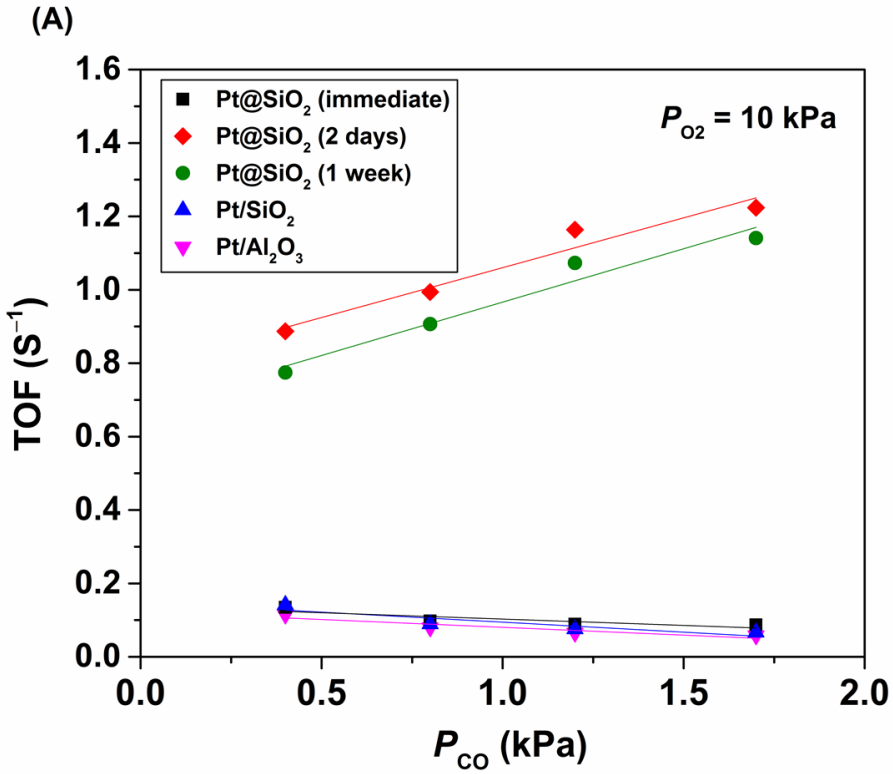
(A)
Pt@SiO2 (immediate)
Pt@SiO2 (2 days)
Pt@SiO2 (1 week)
Pt/SiO2
Pt/Al2O3
PO2 = 10 kPa
TOF (S−1)
PCO (kPa)
0.0
0.2
0.4
0.6
0.8
1.0
1.2
1.4
1.6
0.0
0.5
1.0
1.5
2.0

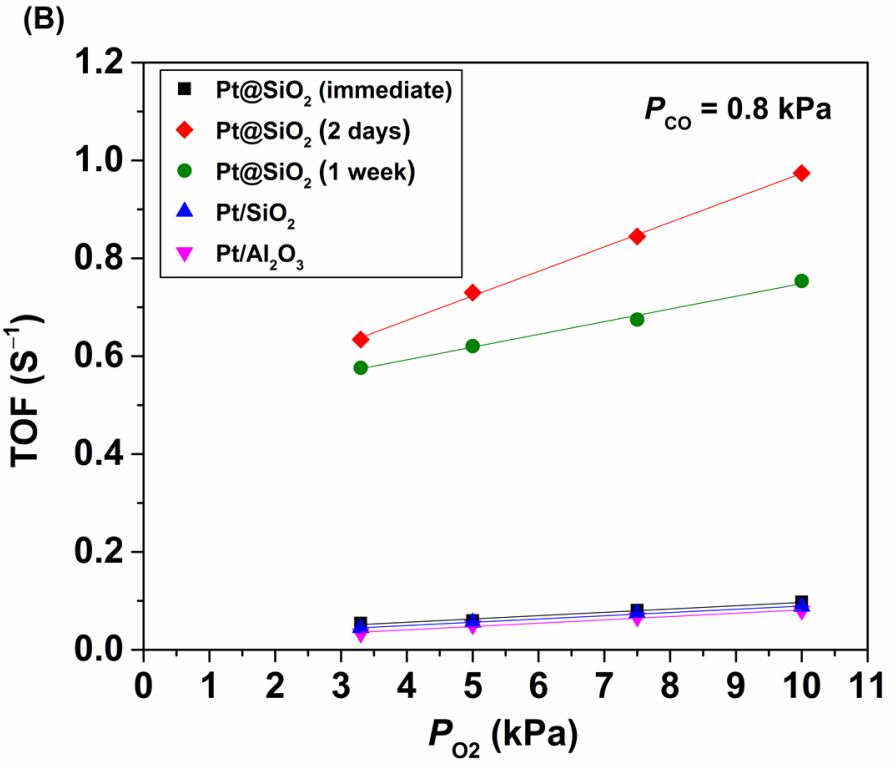
(B)
Pt@SiO2 (immediate)
Pt@SiO2 (2 days)
Pt@SiO2 (1 week)
Pt/SiO2
Pt/Al2O3
PCO = 0.8 kPa
TOF (S−1)
PO2 (kPa)
0.0
0.2
0.4
0.6
0.8
1.0
1.2
0
1
2
3
4
5
6
7
8
9
10
11

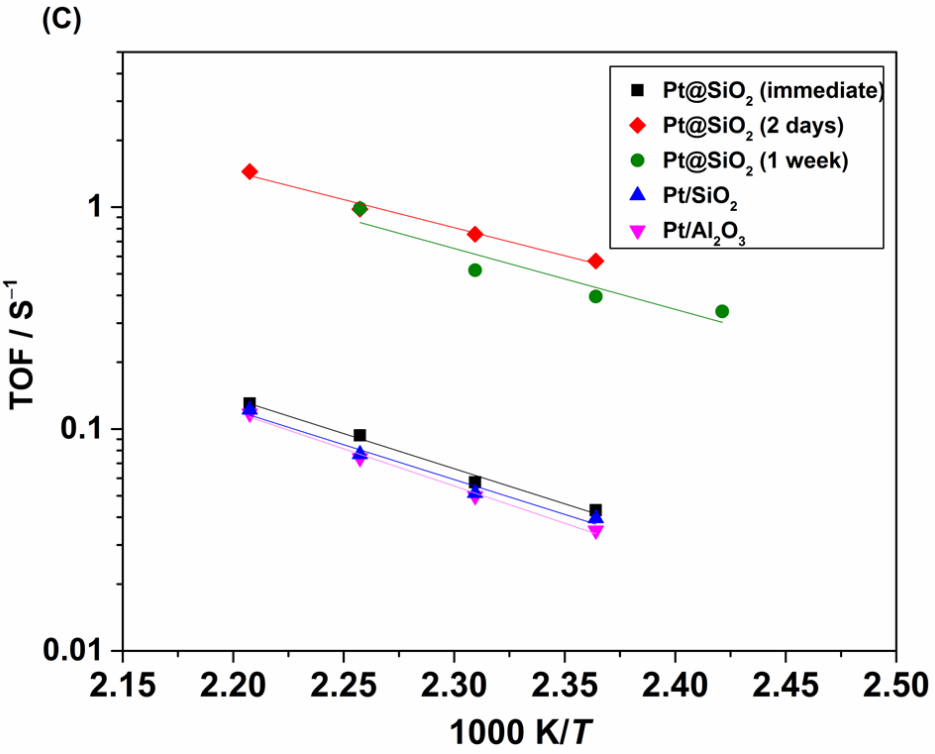

Figure 10. TOFs as a function of (A) CO pressure and (B) O_2 pressure, and (C) Arrhenius plot for CO oxidation using various samples (typically 170 °C, 0.8 kPa CO, 10 kPa O_2, 101 kPa total pressure, balance He).

Table 2. Activation energy, E_a, and kinetic orders for O_2 and CO measured for various catalysts.

Sample	E_a [kJ mol^{-1}]	O_2 order	CO order
Immediate	61±4	0.6	−0.3
2 days	48±3	0.4	0.2
1 week	53±2	0.3	0.3

Pt/SiO_2	60±6	0.6	−0.5
Pt/Al_2O_3	65±1	0.8	−0.5

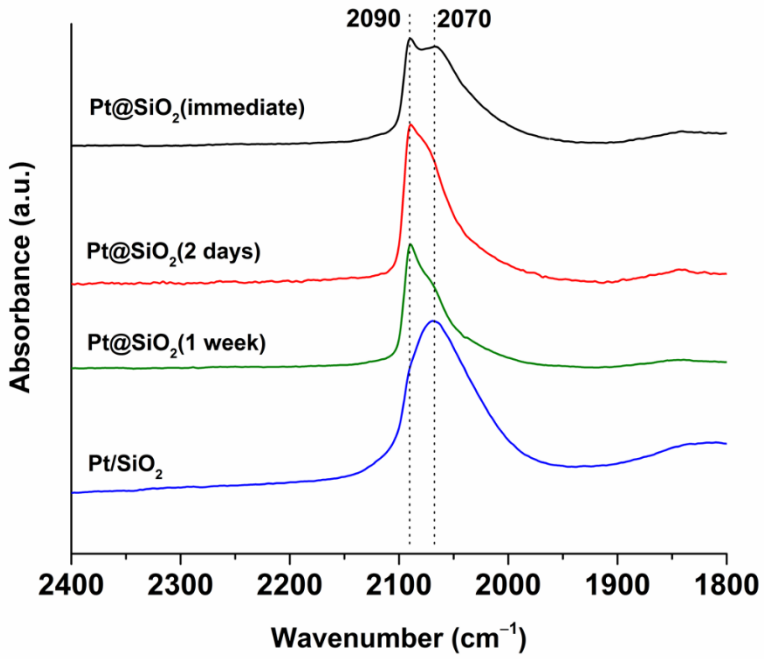

Figure 11. Infrared spectra of CO chemisorbed on the reduced samples at 35 °C.

The next possibility is that the shell affects the diffusion of gases such that the Pt surface sees different pressures of reactants from the set ones. In the literature, gas diffusion through SiO_2 layer in $Pt@SiO_2$ samples affects the selectivity of C_1 to C_4 hydrocarbon oxidation.[10,27] The larger molecule was less reactive, which was ascribed to different extent of gas diffusion in Knudsen region. In the current study, the presence of microporosity in the sample (measured by N_2 sorption, **Figure 9**) suggests that gases may have difficulties passing through

the shell to the core. It is known that there is a threshold O_2/CO ratio at which the surface cannot maintain high CO coverage at a steady state, and O_2 is thus easily accessed on the Pt surface.[33-38,42] This condition provides a highly active surface for CO oxidation.[38] Even at room temperature, alternative introduction of O_2 and CO can continue catalyzing CO_2 formation.[44] To confirm, the O_2/CO was varied to measure this kinetic threshold using the *supported* Pt/Al_2O_3 sample. The result is shown in **Figure 12**. The O_2/CO ratio lower than 25 start to drastically improve TOF at 170 °C, consistent with the literature.[38] This result suggests that the SiO_2 shell may function as a membrane to provide a higher O_2/CO ratio, resulting in high TOF.

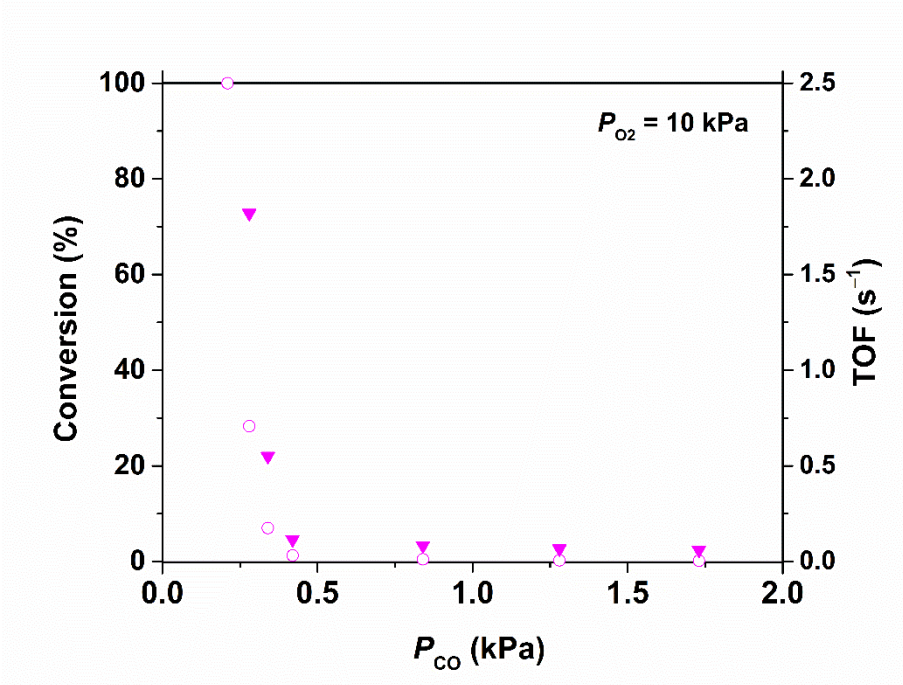

Figure 12. Conversion (circle) and TOF (triangle) as a function of CO pressure for Pt/Al_2O_3 (170 °C, 10 kPa O_2, 101 kPa total pressure, balance He).

Upon H_2 reduction treatment, Pt was able to be reduced (as observed in XPS, **Figure 4**) and the capability of CO chemisorption (**Table 1**) suggests that gas can reach the core. N_2 physisorption result confirmed the presence of micropore in Pt@SiO_2 (**Figure 9**). It is most likely that CO diffusion to the core gets slower compared to O_2 diffusion (kinetic diameter: CO 330 pm[55] vs. O_2 346 pm[56]), which give a lower O_2/CO ratio to provide active Pt surface without CO inhibition at the steady state. We demonstrated that it is a fully novel way to improve the catalytic performance of Pt for CO oxidation using an irreversible oxide shell. There should be many more applications for such a unique core shell structure to control diffusion and to enhance the reaction rate. This study opens the new possibility for a potential application as an active catalyst utilizing the core-shell structure.

2.4. Conclusion

The formation mechanism of Pt@SiO_2 core-shell NPs via water-in-oil (w/o) micro-emulsions was investigated, and the parameters affecting the development of this material were identified. By shifting the pH to alkaline condition using NH_3 aq., Pt ions tend to form nano-$Pt(OH)_2$ colloids. The subsequent aging for this nano-colloid gradually occurred, thus successfully controlling the dispersion of the Pt particle size from sub-nano size to 4-5 nm. There was also a strong dependence of Pt/SiO_2 NP morphologies on the aging time of Pt NPs prior to the addition of TEOS as a SiO_2 source. For example, the highly uniform Pt@SiO_2 *core-shell* structure could be produced when Pt nano-colloid were aged for 2 days and 1

week before adding TEOS. Such synthesized *core-shell* Pt@SiO_2 had distinctively high activities for CO oxidation (one order of magnitude higher turnover rate) compared with conventional *supported* Pt catalysts. There was no evidence for “single-site” Pt species by IR measurement with these samples. The positive CO kinetic order for the *core-shell* sample (in contrast to the negative order for the *supported* one) suggests that the reaction mechanism is totally altered by the *core-shell* structure. The alteration of gas diffusion through the micropore of SiO_2 shell is proposed, which may alter O_2/CO ratio on the Pt surface and thus CO oxidation kinetics. This study clearly demonstrated the controllable design of the *core-shell* Pt@SiO_2 materials by providing pedagogic evidence through each synthesis step. The resultant *core-shell* Pt@SiO_2 provided a novel reaction mechanism for low-temperature CO oxidation, which opens a new concept of catalytic applications using the *core-shell* materials. The study was further extended to other catalytic applications by varying the composition of the core as well as the chemical nature of the shell material. In the next chapter, we studied the possibility of embedding the Pt NPs within another oxide matrix such as ZrO_2 and TiO_2 for CO oxidation reaction.

2.5. References

[1] C. M. Y. Yeung, S. C. Tsang, *J. Mol. Catal. A* **2010**, *322*, 17-25.

[2] C. M. Y. Yeung, S. C. Tsang, *J. Phys. Chem. C* **2009**, *113*, 6074-6087.

[3] C. M. Y. Yeung, F. Meunier, R. Burch, D. Thompsett, S. C. Tsang, *J. Phys. Chem. B* **2006**, *110*, 8540-8543.

[4] Z. Li, L. Mo, Y. Kathiraser, S. Kawi, *ACS Catal.* **2014**, *4*, 1526-1536.

[5] S. Takenaka, Y. Orita, H. Umebayashi, H. Matsune, M. Kishida, *Appl. Catal. A* **2008**, *351*, 189-194.

[6] J. Xu, C. M. Y. Yeung, J. Ni, F. Meunier, N. Acerbi, M. Fowles, S. C. Tsang, *Appl. Catal. A* **2008**, *345*, 119-127.

[7] S. Takenaka, H. Umebayashi, E. Tanabe, H. Matsune, M. Kishida, *J. Catal.* **2007**, *245*, 392-400.

[8] T. Montini, A. M. Condò, N. Hickey, F. C. Lovey, L. De Rogatis, P. Fornasiero, M. Graziani, *Appl. Catal. B* **2007**, *73*, 84-97.

[9] T. Montini, L. De Rogatis, V. Gombac, P. Fornasiero, M. Graziani, *Appl. Catal. B* **2007**, *71*, 125-134.

[10] K. Hori, H. Matsune, S. Takenaka, M. Kishida, *Sci. Technol. Adv. Mater.* **2006**, *7*, 678-684.

[11] S. Takenaka, A. Hirata, E. Tanabe, H. Matsune, M. Kishida, *J. Catal.* **2010**, *274*, 228-238.

[12] C. Zhou, F. Peng, H. Wang, H. Yu, C. Peng, J. Yang, *Electrochem. Commun.* **2010**, *12*, 1210-1213.

[13] S. Takenaka, H. Matsumori, T. Arike, H. Matsune, M. Kishida, *Top Catal.* **2009**, *52*, 731-738.

[14] S. Takenaka, H. Matsumori, H. Matsune, E. Tanabe, M. Kishida, *J. Electrochem. Soc.* **2008**, *155*, B929-B936.

[15] Y. Shimazaki, Y. Kobayashi, M. Sugimasa, S. Yamada, T. Itabashi, T. Miwa, M. Konno, *J. Colloid Interface Sci.* **2006**, *300*, 253-258.

[16] M. B. Gawande, A. Goswami, T. Asefa, H. Guo, A. V. Biradar, D.-L. Peng, R. Zboril, R. S. Varma, *Chem. Soc. Rev.* **2015**, *44*, 7540-7590.

[17] T. Takata, C. Pan, M. Nakabayashi, N. Shibata, K. Domen, *J. Am. Chem. Soc.* **2015**, *137*, 9627-9634.

[18] K. Maeda, K. Teramura, D. Lu, N. Saito, Y. Inoue, K. Domen, *Angew. Chem. Int. Ed.,* **2006**, *45*, 7806-7809.

[19] G.-H. Wang, J. Hilgert, F. H. Richter, F. Wang, H.-J. Bongard, B. Spliethoff, C. Weidenthaler, F. Schüth, *Nat. Mater.* **2014**, *13*, 293-300.

[20] S. H. Joo, J. Y. Park, C.-K. Tsung, Y. Yamada, P. Yang, G. A. Somorjai, *Nat. Mater.* **2009**, *8*, 126-131.

[21] S. Ikeda, S. Ishino, T. Harada, N. Okamoto, T. Sakata, H. Mori, S. Kuwabata, T. Torimoto, M. Matsumura, *Angew. Chem. Int. Ed.* **2006**, *45*, 7063-7066.

[22] J. Wang, Z. H. Shah, S. Zhang, R. Lu, *Nanoscale* **2014**, *6*, 4418-4437.

[23] L. Yao, G. Xu, W. Dou, Y. Bai, *Colloid Surf. A* **2008**, *316*, 8-14.

[24] M.-P. Pileni, *Nat. Mater.* **2003**, *2*, 145-150.

[25] V. Uskoković, M. Drofenik, *Surf. Rev. Lett.* **2005**, *12*, 239-277.

[26] K. A. Dahlberg, J. W. Schwank, *Chem. Mater.* **2012**, *24*, 2635-2644.

[27] S. Takenaka, K. Hori, H. Matsune, M. Kishida, *Chem. Lett.* **2005**, *34*, 1594-1595.

[28] B. Liu, H. Xu, Z. Zhang, *Catal. Commun.* **2012**, *26*, 159-163.

[29] M. Cargnello, J. J. Delgado Jaén, J. C. Hernández Garrido, K. Bakhmutsky, T. Montini, J. J. Calvino Gámez, R. J. Gorte, P. Fornasiero, *Science*, **2012**, *337*, 713-717.

[30] L. De Rogatis, M. Cargnell, V. Gombac, B. lorenzut, T. Montini, P. Fornasiero, *ChemSusChem*, **2010**, *3*, 24-42.

[31] K. Bakhmutsky, N. L. Wieder, M. Cargnello, B. Galloway, P. Fornasiero, R. J. Gorte, *ChemSusChem*, **2012**, *5*, 140-148.

[32] C. H. Bartholomew, *Appl. Catal. A* **2001**, *212*, 17-60.

[33] S. Royer, D. Duprez, *ChemCatChem* **2011**, *3*, 24-65.

[34] P. Hugo, *Ber. Bunsenges. Phys. Chem.* **1970**, *74*, 121-127.

[35] M. Jakubith, *Chem. Ing. Tech.* **1970**, *14*, 943-946.

[36] G. Ertl, P. R. Norton, J. Rüstig, Phys. Rev. Lett, 1982, 49, 177.

[37] J. Wintterlin, S. Völkening, T. V. W. Janssens, T. Zanbelli, G. Ertl, *Science*, **1997**, *278*, 1931-1934.

[38] M. S. Chen, Y. Cai, Z. Yan, K. K. Gath, S. Axnanda, D. W. Goodman, *Surf. Sci.* **2007**, *601*, 5326-5331.

[39] F. Tao, S. Dag, L.-W. Wang, Z. Liu, D. R. Butcher, H. Bluhm, M. Salmeron, G. A. Somorjai, *Science*, **2010**, *327*, 850-853.

[40] A. Bourane, D. Bianchi, *J. Catal.* **2001**, *202*, 34-44.

[41] A. Bourane, D. Bianchi, *J. Catal.* **2002**, *209*, 126-134.

[42] A. D. Allian, K. Takanabe, K. L. Fujdala, X. Hao, T. J. Truex, J. Cai, C. Buda, M. Neurock, E. Iglesia, *J. Am. Chem. Soc,* **2011**, *133*, 4498-4517.

[43] K. Ding, A. Gulec, A. M. Johnson, N. M. Schweitzer, G. D. Stucky, L. D. Marks, P. C. Stair, *Science*, **2015**, *350*, 189-192.

[44] M. A. Newton, D. Ferri, G. Smolentsev, V. Marchionni, M. Nachtegaal, *Nat. Commun.* **2015**, *6*, 8675.

[45] M. Cargnello, V. V. T. Doan-Nguyen, T. R. Gordon, R. E. Diaz, E. A. Stach, R. J. Gorte, P. Fornasiero, C. B. Murray, *Science* **2013**, *341*, 771-773.

[46] B. Qiao, A. Wang, X. Yang, L. F. Allard, Z. Jiang, Y. Cui, J. Liu, J. Li, T. Zhang, *Nat. Chem.* **2011**, *3*, 634-641.

[47] E. J. Peterson, A. T. DeLaRiva, S. Lin, R. S. Johnson, H. Guo, J. T. Miller, J. H. Kwak, C. H. F. Peden, B. Kiefer, L. F. Allard, F. H. Ribeiro, A. K. Datye, *Nat. Commun.* **2014**, *5*, 4885.

[48] M. Moses-Debusk, M. Yoon, L. F. Allard, D. R. Mullins, Z. Wu, X. Yang, G. Veith, G. M. Stocks, C. K. Narula, *J. Am. Chem. Soc.* **2013**, *135*, 12634-12645.

[49] Y. Chen, L. Liu, Y. Wang, H. Kim, *Fuel. Process. Technol.* **2011**, *92*, 1368-1373.

[50] J. E. Drawdy, G. B. Hoflund, S. D. Gardner, E. Yngvadottir, D. R. Schryer, *Surf. Interface Anal.* **1990**, *16*, 369-374.

[51] J. W. Guo, T. S. Zhao, J. Prabhuram, C. W. Wong, *Electrochim. Acta* **2005**, *50*, 1973-1983.

[52] Y. Jin, A. Li, S. G. Hazelton, S. Liang, C. L. John, P. D. Selid, D. T. Pierce, J. X. Zhao, *Coord. Chem. Rev.* **2009**, *253*, 2998-3014.

[53] Y.-F. Yu Yao, *J. Catal.* **1984**, *87*, 152-162.

[54] M. Primet, J. M. Basset, M. V. Mathieu, M. Prettre, *J. Catal.* **1973**, *29*, 213-223.

[55] A. F. Ismail, K. Khulbe, T. Matsuura, **2015**, Gas Separation Membranes: Polymeric and Inorganic, Springer.

[56] S. Matteucci, Y. Yampolskii, B. D. Freeman, I. Pinnau, **2006**, "Transport of gases and vapors in glassy and rubbery polymers" in, Y. Yampolskii, B. D. Freeman, I. Pinnau, Materials Science of Membranes for Gas and Vapor Separation, pp. 1-47, John Wiley & Sons.

CHAPTER 3

3. Embedded Pt NPs within Oxide Matrix (Tio_2 or Zro_2) via Reverse Micro-Emulsion Method for CO Oxidation

3.1 Graphical abstract

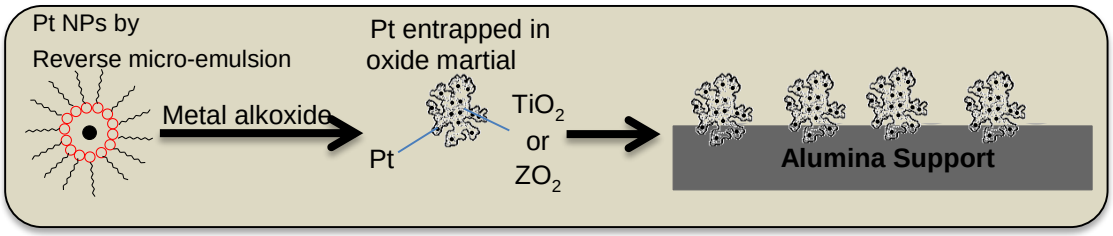

3.2 Introduction

Supported metal NPs usually shows improved catalytic properties compared to the bare metals NPs NPs. This is due to higher dispersion of the metal NPs onto the support compared to unsupported NP and also in certain cases to the so called “metal-support” interactions.[1] Metal-metal oxide contact boundaries may play in some cases an important role in catalytic activity: [2-3] Sometimes, but not always, the higher the number of metal atoms in contact with the metal oxide support, the better the catalyst performances. The strength of support–metal interactions may depend on the size, shape and nature of both the metal of the NPs and the support (acido basic, redox aso).[1-2, 4] For instance, D. Rolison et al.,[5-6] found that the loading Au NPs of 6 nm size onto commercial TiO_2 powders were inactive in CO oxidation while Au NPs of similar size on TiO_2 support

with the size of 10-12 nm showed high activity in CO oxidation due to the formation of Au-TiO_2 mixed oxide. Another study, conducted by X. Zhang et al.,[7] showed that the smaller nanosize (5-15 nm) of ZrO_2 in Au/ZrO_2 catalysts which exhibit higher catalytic performance for CO oxidation compared with a catalyst containing larger ZrO_2 (40-200 nm) and similarly sized Au-metal NPs. Obviously, the interaction at the metal-support ”perimeter” can be altered by reducing the particle size of metal on the oxide support.[7] Minimizing the distance at the metal-support boundaries facilitates the diffusion of the adsorbed reactant intermediates over the surface between the metal and its support.[7]

Another possible way to maximize the interaction at the metal-support interfaces is embedding the active metal NPs in oxides cavities. Recently, researchers have shown more and more interest in the design of embedded metal NPs in oxide matrix such as (SiO_2, TiO_2, CeO_2, Fe_2O_3, ZrO_2, etc.); due to the unique properties of these embedded NPs and their ability to prevent metal sintering at high temperatures. For example, metal@SiO_2[8-17] core-shell systems have been intensively reported in the literature since the coating of the SiO_2 layer over various metals or bimetallic NPs can be easily controlled due to their slow hydrolysis behavior. There are only a few reports on the coating of metal NPs on other oxides such as TiO_2[18] and CeO_2[19-20] and ZrO_2[21]; owing to their rapid hydrolysis that makes their coating more challenging to control. Coating the metal particles with ZrO_2 and TiO_2 layer can greatly enhance the interaction between the metal and metal oxide by the formation of metal-O-M (M= ZrO_2 and TiO_2) and the dispersion of metal NPs.[22] Moreover, the use of TiO_2 in Pt/TiO_2 catalyst for CO

oxidation reaction can promote the dissociation of O_2 molecules, reduce CO poising and increase the CO mobility on Pt NP which increases CO production.[23]

Therefore, herein we successfully report the synthesis and characterization of highly dispersed Pt NPs embedded within TiO_2 and ZrO_2 matrix via reverse micro-emulsion procedure. This synthesis method will involve fewer and easier steps than previously published.[18, 21] In this chapter we will discuss the challenges of designing embedded Pt@oxide structure with different oxides (TiO_2 and ZrO_2). CO oxidation was used as a model reaction to evaluate these metal-oxide hybrid catalysts.

3.3 Material and methods

3.3.1 Chemicals

The following chemicals were used as received: Cyclohexane (GPR REACTAPUR®100%, VWR chemicals), IGEPAL®CO-520 (Sigma Aldrich) Polyoxyethylene (5) nonylphenylether a nonionic surfactant also referred to as (NP5), ethanol (absolute ³ 99.8, Sigma Aldrich), platinum (IV) chloride (³ 99.9%, Sigma Aldrich), hydrazine monohydrate (64%, Sigma Aldrich), titanium (IV) butoxide (97%, Sigma Aldrich), zirconium (IV) butoxide (76%-80% diluted in n-butanol, Stream chemicals) and sodium hydroxide (≥97.0%, pellets). ɣ-Alumina pellets (bimodal, Alfa Aesar) was crushed to a fine powder and calcined at 850°C for 12 h before used. 18.2 MΩ.cm deionized water was used.

3.3.2 Pt NP synthesis

First, platinum (IV) chloride was dissolved in 3.5 ml water to prepare the stock solution of Pt salts. The amount of platinum (IV) chloride added was varied (86 mg / 256 µmol) or (17.3 mg / 51 µmol) depending on the weight ratio of (MO_2/Pt= 0.2 or 1; M=Ti and Zr), respectively. Then, two sets of reverse micro-emulsion solutions were prepared and both contained 17.2 mg NP5 and 54 ml cyclohexane. The molar ratio of NP5/water/cyclohexane in both micro-emulsion mixtures was fixed to (1/5/17). 3.5 ml Pt stock solution was added to micro-emulsion solution I and a mix solution containing hydrazine (16 mol vs Pt), NaOH (1 M, 2 mL) and 1 mL of water was added to the micro-emulsion solution II. Before mixing the two micro-emulsion solutions together, they were separately stirred until a transparence mixture was obtained thus the stability of the micro-emulsion was reached. After that, the two micro-emulsion solutions were mixed and the transparent greenish micro-emulsion turned to black upon stirring after one day indicating the formation of bimetallic NPs.

3.3.3 Pt@TiO_2 and Pt@ZrO_2 core-shell structure synthesis

To coat the Pt with a TiO_2 or ZrO_2 layer, 45 µl titanium (IV) butoxide or 41µl zirconium (IV) butoxide was added directly to the Pt micro-emulsion mixture. The metal (IV) butoxide was left to hydrolyze in the micro-emulsion solution for 1 day under continuous stirring. Next, Pt/MO_2 micro-emulsion mixture was divided into two sections: the first one was kept for the Alumina deposition and the second

portion was separated by centrifuge, the resulting powder was washed twice with cyclohexane and twice with ethanol. Later, the Pt@MO_2 powder was dried in the oven at 120°C overnight and calcined after that in a conventional oven at 400°C for 3 h with heating ramp 2°C/min. The reduction (4% H_2 in 96% He) was performed at 800°C for 3 h with heating ramp 10°C/min.

3.3.4 Deposition of Pt@TiO_2 and Pt@ZrO_2 NPs on Al_2O_3

To prepare γ-Al_2O_3 supported Pt@MO_2 (MO_2= TiO_2 or ZrO_2) sample (total 1% Pt) for catalytic reaction, the resultant micro-emulsion solution III was added dropwise to 200 mL of ethanol with 500 mg of γ-Al_2O_3 powder suspension in 500 ml round-bottom flask. The mixture was kept under stirring for 4 h then separated by centrifuge and washed with ethanol twice. Later, all the obtained powder (with or without γ-Al_2O_3) was dried in the oven at 120°C overnight. The samples were treated in a muffle furnace in static air at 400°C for 3 h with ramping rate of 1°C min^{-1}. The reduction (4% H_2 in Ar) was performed in a tubular reactor at 250°C for 1 h with a ramping rate of 1°C min^{-1}. The metal loading was confirmed by elemental analysis.

3.3.5 Characterization

The synthesized Pt@TiO_2 and Pt@ZrO_2 samples were characterized by transmission electron microscopy (TEM) before deposition on Alumina to study the catalysts without the support and obtain the particle size distribution. TITAN ST

(FEI company), machines was mainly used for the characterization, operated at 300kV and 120kV respectively. X-ray energy dispersive spectroscopy (EDS) was used under the scanning transmission electron microscopy (STEM) mode with a 1 nm spot size to capture the profile of element composition. The specimens were prepared for the TEM by dissolving the sample in ethanol and placing a single drop to the TEM grid. The TEM grid that was used is a carbon film on 300 mesh copper grids.

The X-ray diffraction (XRD) patterns of the catalysts were recorded after the calcination 400°C for 3 h on a Bruker DMAX 2500 X-ray diffractometer with Cu Kα radiation (λ=0.154 nm).

Temperature program reduction (TPR) was used to study the reducibility of the catalysts after calcination at 400°C for 3 h. The samples were heated from 40°C to 250°C with a ramp of 1°C/min under 4%H_2 in He with 20 mL/min flow rate. Thermal conductivity detector (TCD) was used to record the signals.

3.3.6 Catalytic test

The CO oxidation reaction was conducted in a fixed bed reactor at atmospheric pressure. The gas detection for CO, O_2 and CO_2 was conducted using Agilent Technologies 3000A Micro GC. The Pt@TiO_2/Al_2O_3, and Pt@ZrO_2/Al_2O_3catalyst bed were supported using quartz wool in a U-shaped quartz tube with an internal diameter of 4 mm. The catalyst was pretreated by flowing 10% O_2-90% He with 100 ml min^{-1} flow at 300 °C for 30 min with a ramping

rate of 10°C min^{-1}. Then the catalyst was activated by reduction with 100 ml min^{-1} flow of H_2-He (respective molar ratio 40/60) at 250°C for 1 h. For the CO oxidation reaction, ~30 mg of catalyst was used, and the total gas flow was 60 ml min^{-1} of 1% CO and 10% O_2 diluted in He giving a gas hourly space velocity (GHSV) of ~120,000 mL g^{-1} h^{-1}. The reaction started at 80°C and heated to 300°C with a ramping rate of 1°C min^{-1}.

3.4 Results and discussion

3.4.1 Structural characterization

Pt NPs (50 mg) with uniform size were synthesis first via micro-emulsion method (**Figure 13**) to form 1.6±0.3 nm NPs (**Figure 14**). A small amount of metal alkoxide ($Ti(OC_4H_9)_4$ and $Zr(OC_4H_9)_4$) were added to the Pt micro-emulsion solutions to produce ~10 mg of the oxides and giving a weight ratio of (MO_2/Pt=~0.2; M=Ti or Zr). The Pt@MO_2 samples (M=Ti or Zr) were separated by centrifuge and washed several times to remove the surfactant. The Pt@MO_2 samples were further subjected to thermal treatment at 400°C for 3 h under air to remove the surfactant completely which was confirmed by TGA (data of TGA not shown). TEM was performed on the Pt@TiO_2 and Pt@ZrO_2 NPs without alumina support samples to observe the structure and morphology of the NPs. (**Figure 15 A and B**) and (**Figure 15C and D**) represent the TEM images of Pt@TiO_2 and Pt@ZrO_2, respectively, after calcination at 400°C for 3 h. The TEM images of Pt@TiO_2 sample clearly show condensation of Pt NPs and a large part of Pt NPs

were aggregated with each other. Some of Pt NPs was embedded within TiO_2 matrix, and only small amount of amorphous TiO_2 was observed in the sample. Pt@ZrO_2 sample had more Pt NPs embedded within the amorphous ZrO_2 matrix than in the case of TiO_2. However, obviously, from the TEM images, the amount of Pt NPs (50 mg) exceeded the amount of TiO_2 and ZrO_2 oxide (10 mg). Consequently, the oxide (TiO_2 or ZrO_2) did not covered all the Pt NPs, and a large part of Pt NPs have aggregated away from the oxide. Therefore, the amount of Pt was reduced from 50 mg to ~10 mg to make the quantity of Pt equal to that of the oxides, accordingly the weight ratio MO_2/Pt changed from 0.2 to 1 (M=Ti or Zr). Cyclohexane, NP5, water, and TiO_2 or ZrO_2 amounts were maintained constant. TEM images of Pt@TiO_2 and Pt@ZrO_2 samples (MO_2/Pt=~1; M=Ti or Zr) after calcination at 400°C for 3 h are shown in (**Figure 16A**) and (**Figure 17A**), respectively, and STEM figures of Pt@TiO_2 and Pt@ZrO_2 samples are represented in (**Figure 16C**) and (**Figure 17C**), respectively. TEM and STEM images show that mono-dispersed Pt NPs with uniform size around 1.8 nm in both Pt@TiO_2 and Pt@ZrO_2 samples. These Pt particles were completely surrounded by amorphous layers and theses layers were identified by EDX analysis under STEM mode. EDX analysis (**Figure 16C**) of Pt@TiO_2 sample shows the layer around Pt NPs contained Ti, and Zr was present in the layer of Pt@ZrO_2 sample (**Figure 17C**). Therefore, these results confirm that all Pt NPs (1.8 nm) were embedded within the amorphous TiO_2 or ZrO_2 oxides matrix. Next, the samples heat-treated at 400°C were subsequently treated in H_2 at 250°C. TEM images of the reduced samples are shown in **Figure 18** and **Figure 19**. The size of Pt NPs

in the Pt@TiO_2 sample was 2 nm after reduction. Clearly, the Pt NPs were protected against sintering by the TiO_2 layer. Whereas, the Pt NPs in the Pt@ZrO_2 sample were slightly larger than the ones in the Pt@TiO_2 sample; giving a size of 2.8 nm. No structure and morphology change was observed in the embedded Pt@TiO_2 and Pt@ZrO_2 samples after reduction at 250°C.

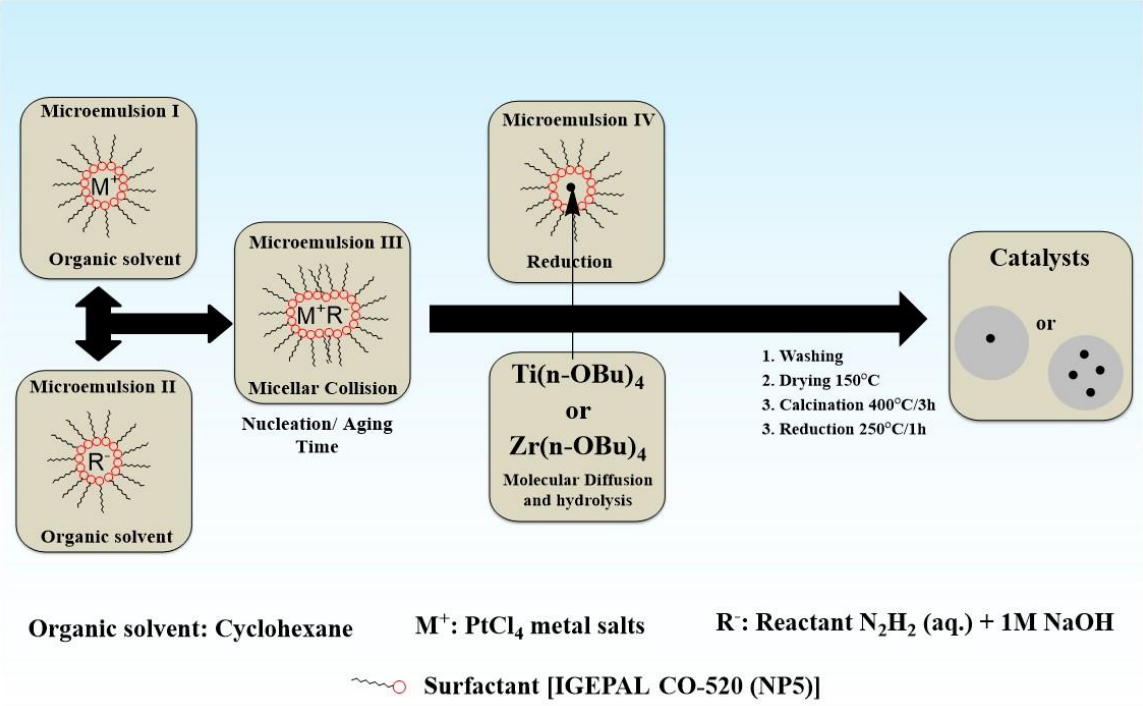

Figure 13. Diagram of the general methodology of Pt@TiO_2 or Pt@ZrO_2 synthesis via reverse micro-emulsion procedure.

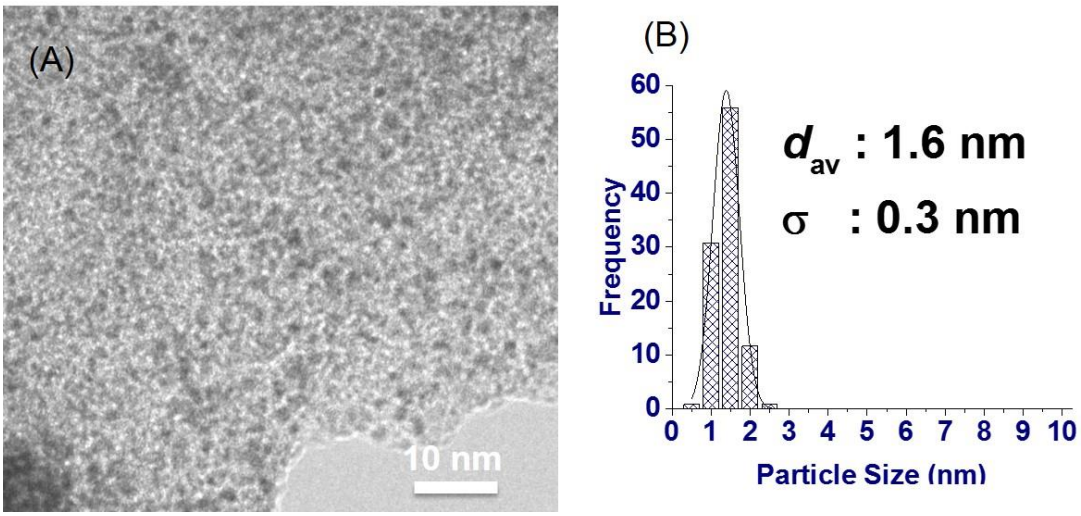

Figure 14. HRTEM images of Pt NPs as-prepared (A) together with histogram of Pt particle size distribution (B).

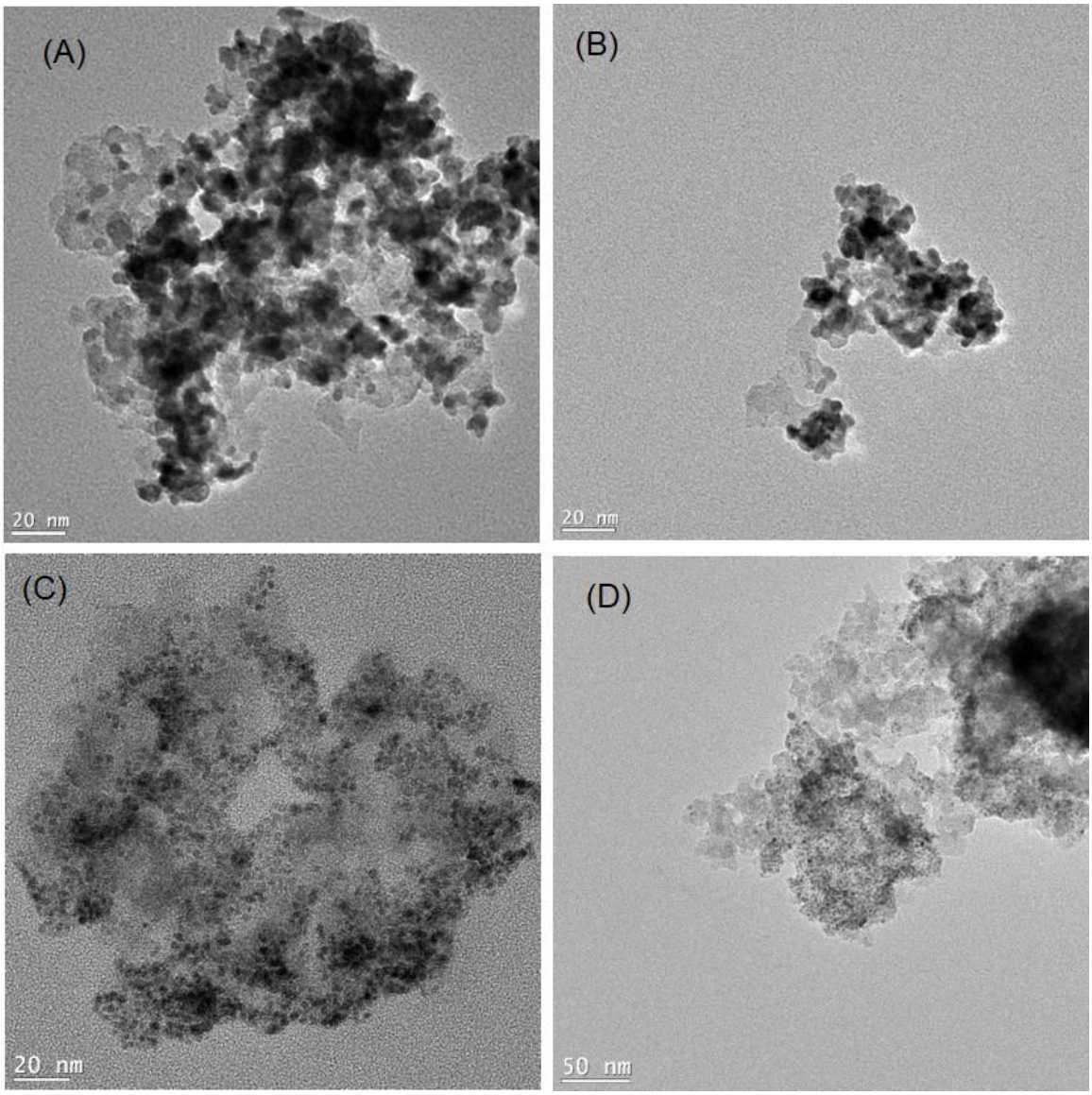

Figure 15. HRTEM images of Pt@MO_2 NPs (M=Ti or Zr) (weight ratio=MO_2/Pt=0.2) after calcination at 400°C for 3 h: Pt@TiO_2 NPs (A) and (B) Pt@ZrO_2 NPs (C) and (D).

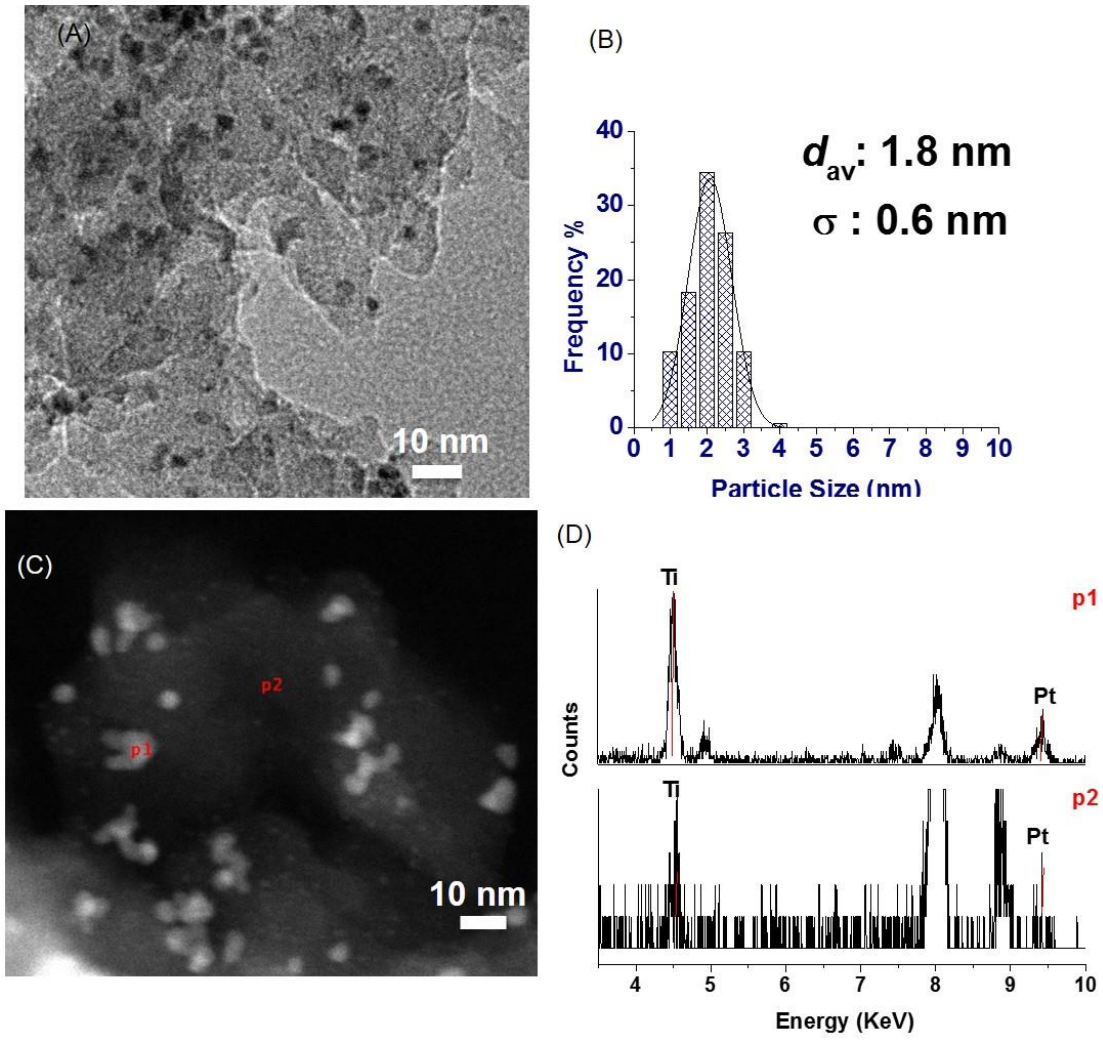

Figure 16. HRTEM images of Pt@TiO_2 NPs (weight ratio=TiO_2/Pt=1) after calcination at 400°C for 3 h (A) together with histogram of Pt particle size distribution (B). STEM images of the same sample along with (C) spot EDX analysis (D).

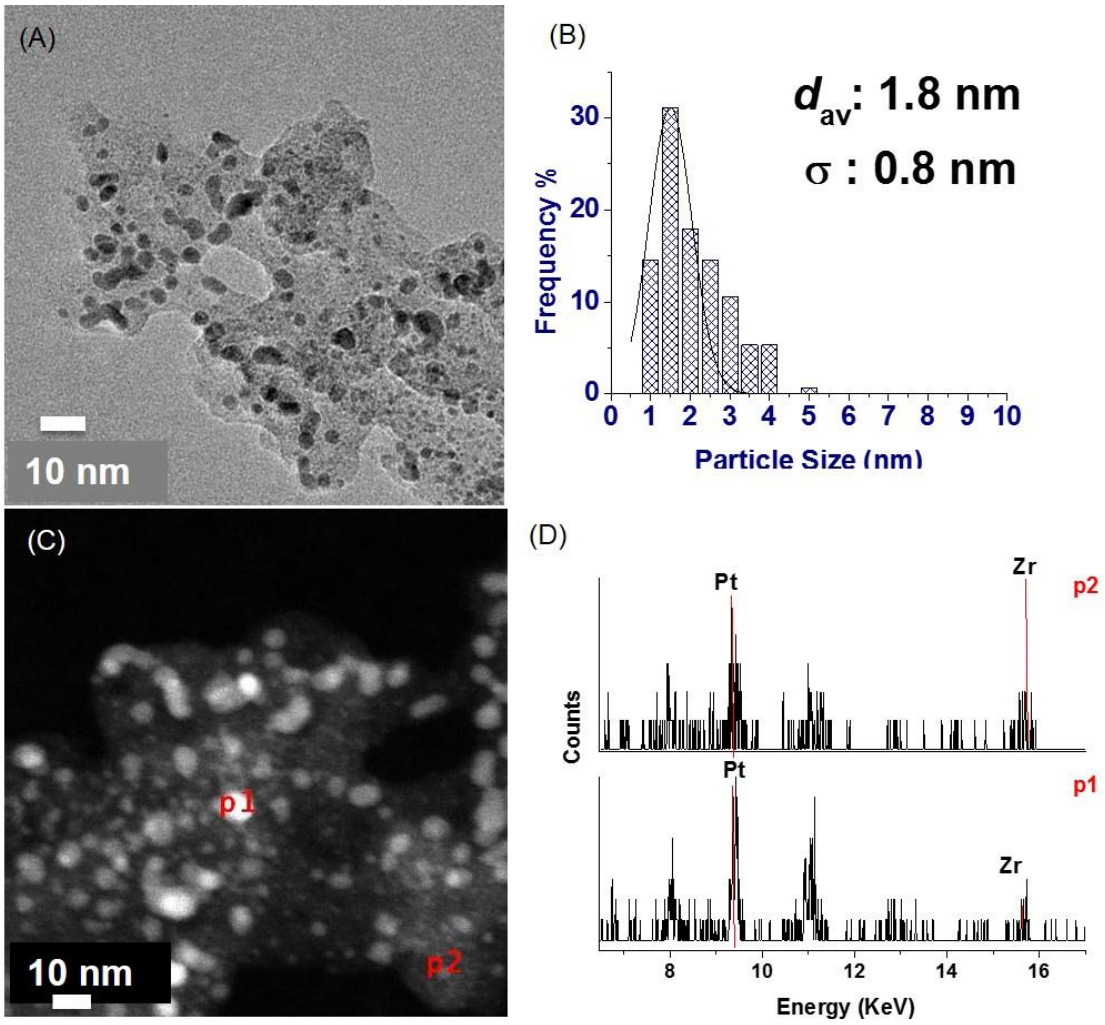

Figure 17. HRTEM images of Pt@ZrO_2 NPs (weight ratio=ZrO_2/Pt=1) after calcination at 400°C for 3 h (A) together with histogram of Pt particle size distribution (B). STEM images of the same sample along with (C) spot EDX analysis (D).

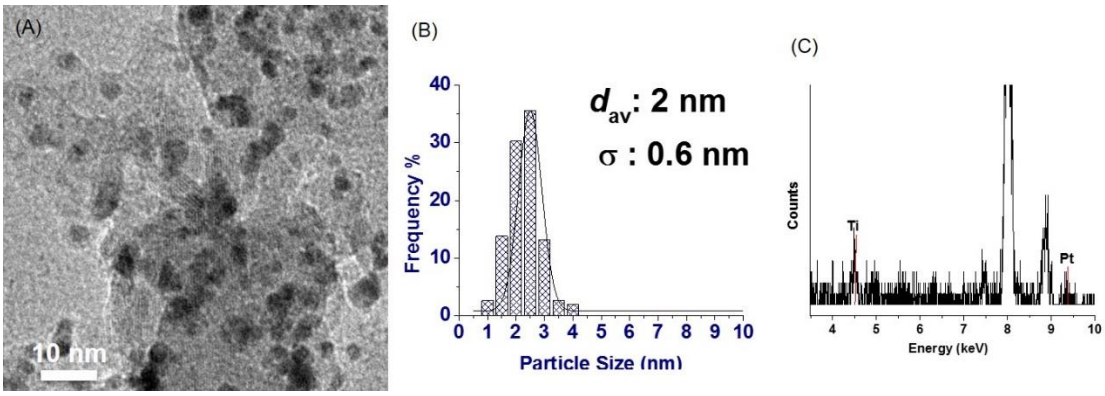

Figure 18. HRTEM images of Pt@TiO_2 NPs (weight ratio=TiO_2/Pt=1) after reduction at 250°C for 3 h (A) together with histogram of Pt particle size distribution (B) and EDX survey (C).

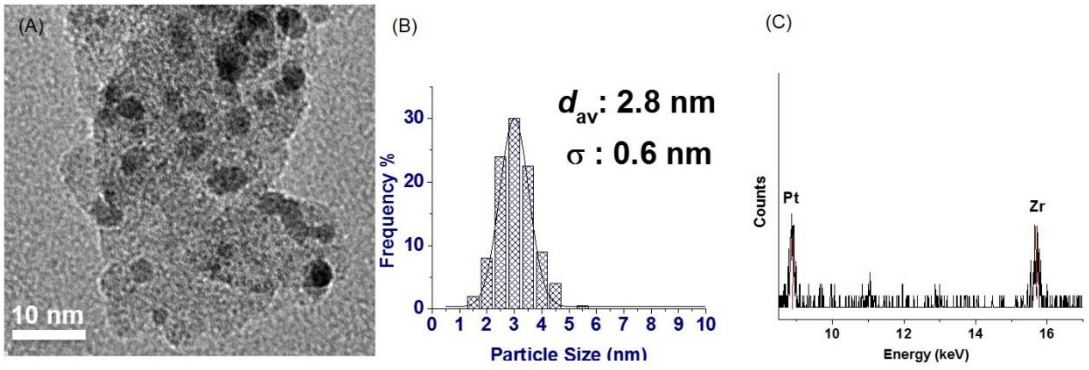

Figure 19. HRTEM images of Pt@ZrO_2 NPs (weight ratio=ZrO_2/Pt=1) after reduction at 250°C for 3 h (A) together with histogram of Pt particle size distribution (B) and EDX survey (C).

The structural evaluation of embedded Pt NPs within the TiO_2 and ZrO_2 matrix can be explained from the TEM images results as follows: the fine Pt NPs (1.8 nm) formed at the first stage, when the two micro-emulsion solutions of $PtCl_4$ salts and hydrazine were mixed, were ultrafine monodisperse inside the micelle structure. Next, the metal butoxide $M(OC_4H_9)_4$ (M=Ti or Zr) diffuses through the

micelles and starts to hydrolyze once it contacted the water present inside the micelle when it was added to the micro-emulsion containing Pt NPs. The metal butoxide $M(OC_4H_9)_4$ hydrolyzes rapidly inside the micelles forming aggregates that deposited around the Pt NPs, as results, Pt NPs was surrounding by the oxides (TiO_2 or ZrO_2). When the amount of Pt NPs exceeded the amount of TiO_2 and ZrO_2 oxide (weight ratio of MO_2/Pt=~0.2; M=Ti or Zr), the Pt NPs was not fully covered by the oxide and tend to aggregate due to incomplete protection. Having the equivalent amount of Pt NPs to the oxide (weight ratio of MO_2/Pt=~1; M=Ti or Zr) have fully covered the Pt NPs with oxides forming embedded Pt@MO_2 structure. Therefore, further characterizations were conducted on the samples with the higher weight ratio of MO_2/Pt=~1. The size of Pt NPs embedded within TiO_2 matrix after reduction at 250°C weight ratio of MO_2/Pt=~1 (M=Ti or Zr) were slightly smaller (2 nm) than those within ZrO_2 matrix (2.8 nm). The smaller size of metal particles on TiO_2 support compared with ZrO_2 was also reported for supported Au/TiO_2 and Au/ZrO_2.[24] This might be due to the strong interaction between the metal andTiO_2.[25-26]

The X-ray diffraction (XRD) analysis was done on the Pt@TiO_2 and Pt@ZrO_2 (MO_2/Pt ratio= 1) samples calcined in the air at 400°C for 3 h (**Figure 20**). For both samples, peaks located at 2θ = 39.7, 46 and 67.6 corresponds to (111), (200) and (220) Pt crystal planes, respectively, for the face-centered cubic (fcc) structure.[27-28] Also, the peaks at 2θ = 24.8 and 30.8 measured by XRD ascribed to TiO_2 and ZrO_2,[29] respectively, which confirms the presence of TiO_2 and ZrO_2.

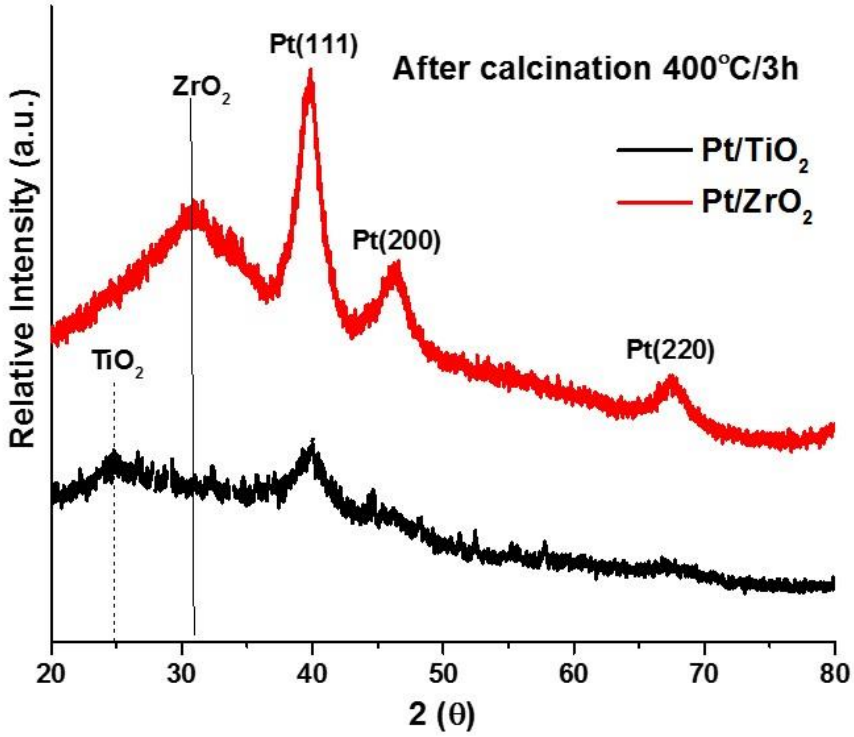

Figure 20. XRD pattern of $Pt@TiO_2$ and $Pt@ZrO_2$ NPs (weight ratio=MO_2/Pt=1) after calcination at 400°C for 3 h.

Temperature program reduction (TPR) was conducted to study the reduction behavior of $Pt@TiO_2$ and $Pt@ZrO_2$ (MO_2/Pt ratio= 1) samples calcined in the air at 400°C for 3 h. **Figure 21** illustrates the TPR profiles of $Pt@TiO_2$ and $Pt@ZrO_2$ NPs. The Pt NPs were reduced completely at 120°C and 194°C for $Pt@TiO_2$ and $Pt@ZrO_2$ samples, respectively, which confirms the reduction of Pt NPs. The temperature peaks are in good agreement with those reported for supported Pt/ZrO_2 and Pt/TiO_2.[30-32]

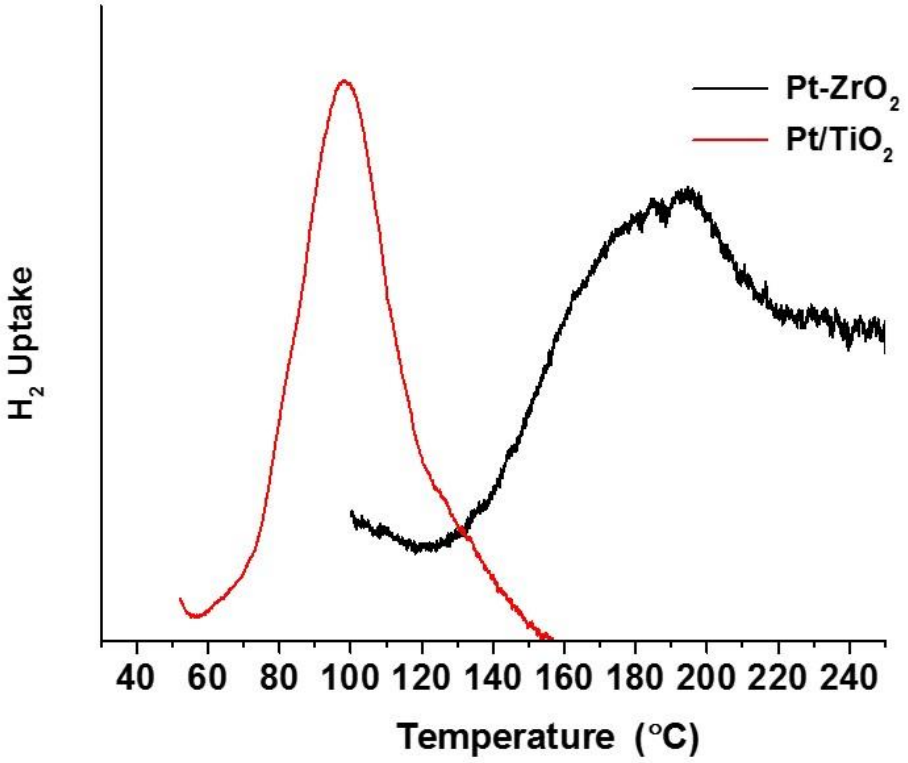

Figure 21. TPR profiles of $Pt@TiO_2$ and $Pt@ZrO_2$ NPs (weight ratio=MO_2/Pt=1) after calcination at 400°C for 3 h.

3.4.2 Catalytic performance characterization

The amount of synthesized embedded $Pt@TiO_2$ and $Pt@ZrO_2$ sample were less than 10 mg. Therefore, it was not possible to check the porosity of the $Pt@TiO_2$ and $Pt@ZrO_2$ nanostructures using N_2 physisorption. To investigate the accessibility of Pt NPs in $Pt@TiO_2$ and $Pt@ZrO_2$ catalysts, these samples were dispersed on Al_2O_3 as described in the Experimental section; giving a 0.8% Pt loading over Al_2O_3 for both catalysts as confirmed by inductively coupled plasma

(ICP) (**Table 3**). The samples were tested for CO oxidation and the CO conversion with respect to temperature as shown in Figure 22 for Pt(0.8%)@MO_2/Al_2O_3 (M= Ti and Zr) catalysts. Indeed, the Pt@TiO_2 catalyst had the higher initial activity CO conversion compared with the Pt@ZrO_2 giving a value of 7% and 0.4%, respectively; however, both catalysts gave full CO conversion at 165°C. Importantly, the catalytic activity results prove the Pt NPs are accessible within the oxide layer. Next, Low-temperature CO oxidation was carried out using the Pt(0.8%)@MO_2/Al_2O_3 (M= Ti and Zr) catalysts. The catalysts were 14 times diluted with inert Al_2O_3 to avoid influence on the kinetics by the reaction exotherms.[33] The Arrhenius plot is shown in **Figure 23** for the various catalysts. Clearly, the catalyst activity per surface atom can be ranked in the order of Pt@TiO_2>Pt@ZrO_2. It was confirmed that the TOF for the Pt@TiO_2 catalyst was nearly twice as high as Pt@ZrO_2 samples. The activation energies were also consistently slightly lower for the Pt@TiO_2 sample than for the Pt@ZrO_2 one (**Table 4**), likely because of the different coverage and resultant reaction mechanism.[34]

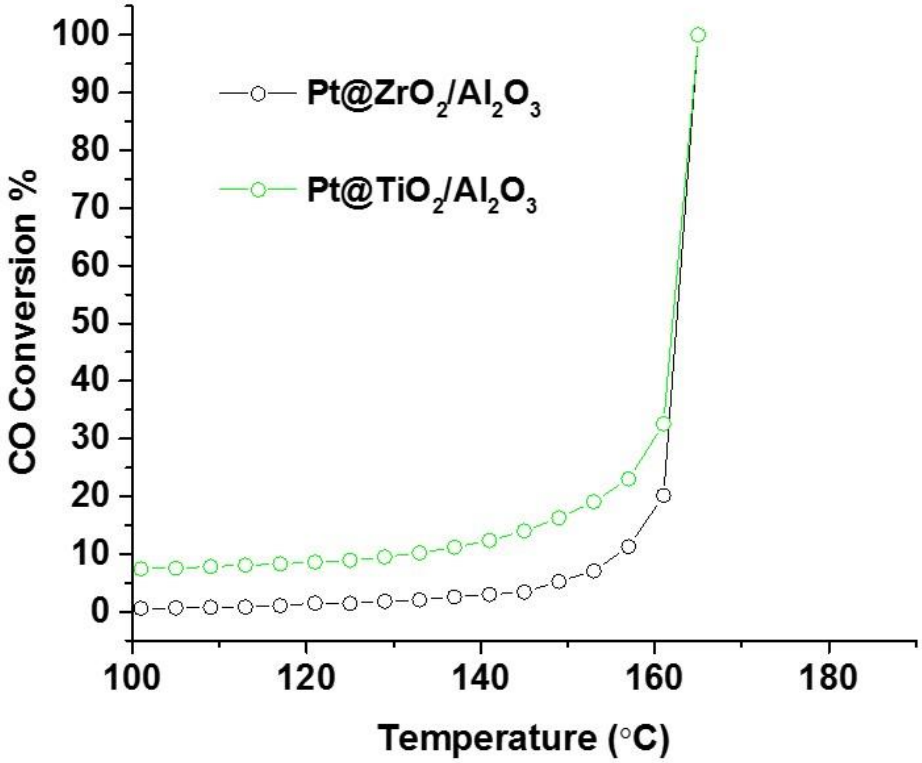

Figure 22. CO oxidation catalytic activity on Pt(0.8%)/MO_2/Al_2O_3 catalysts (M= TiO_2 and ZrO_2).

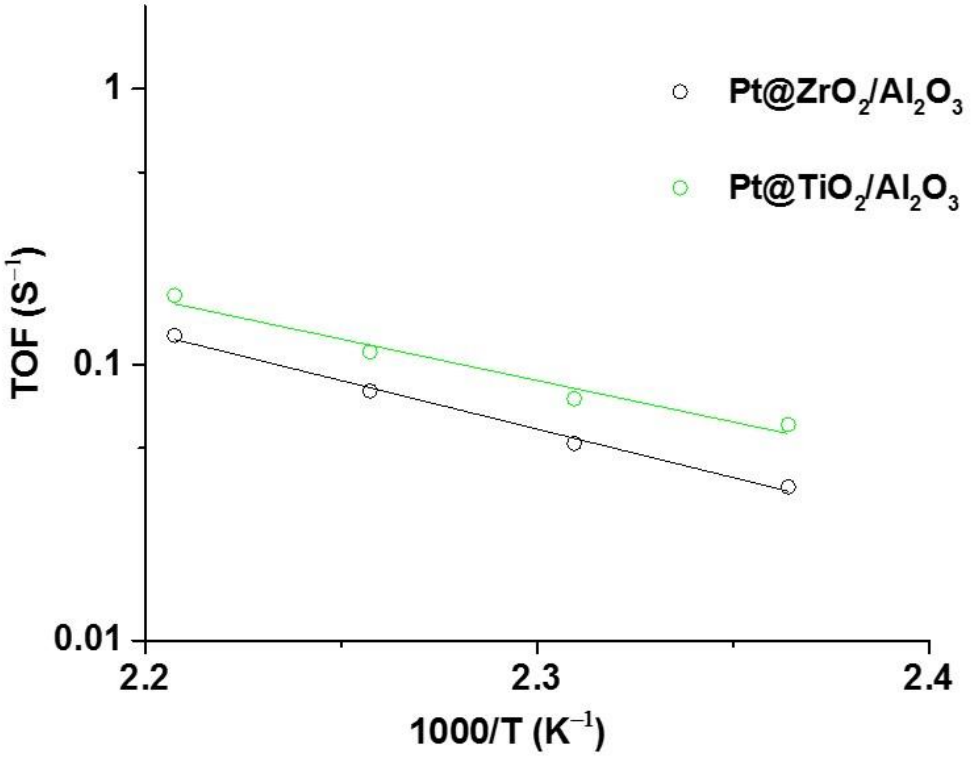

Figure 23. Arrhenius plot for CO oxidation using $Pt@TiO_2$ and $Pt@ZrO_2$ catalysts.

Table 3.

Measured properties of Pt in various catalysts

Sample	Pt loading[a] [wt%]	Pt particle size (TEM) [nm]	Dispersion[b] [%]
$Pt@TiO_2$	0.8	2±0.6	39

$Pt@ZrO_2$	0.8	2.8±0.6	30
[a] Pt loading in Al_2O_3-supported $Pt@MO_2$ samples used for CO oxidation [b] Dispersion measured by TEM using %D = 100/(particle size in nm)			

Table 4.

Activation energy, *E*a, for various catalysts.

Sample	E_a [kJ mol^{-1}]
$Pt@TiO_2$	58
$Pt@ZrO_2$	67

It has been previously reported that the CO oxidation reaction proceeds via a Langmuir-Hinshelwood mechanism involving the reaction between CO and dissociated-O_2 adsorbed on Pt surfaces[34-35], and that high oxygen coverage of Pt surfaces is favorable for CO oxidation whereas high CO coverage limits catalytic performance ("self-poisoning")[34, 36]. One way to improve the CO oxidation rate is to use a reducible oxide such as CeO_2[4, 34]or TiO_2[35] as a support. It is considered that mobile oxygens are provided by the reducible oxide which would react directly with CO at the metal-support perimeter,[4, 35] even if Pt surface is fully covered with CO at a steady state. This could explain the catalyst activity improvement in the

case of Pt@TiO_2 compared with Pt@ZrO_2 since TiO_2 stabilized or provides highly reactive oxygen species at the Pt-TiO_2 interface.[35]

3.5 Conclusion

Mono-dispersed Pt NPs (1.8 nm) were synthesized by reverse micro-emulsion procedure. Upon addition of the metal butoxide $M(OC_4H_9)_4$ (M=Ti or Zr) into the micro-emulsion system containing Pt NPs, these precursors diffuse through the micelles and hydrolyze rapidly once it contacts with the water present in the micelles. As a result, amorphous oxides were formed as aggregated and deposited around the Pt NPs. By controlling weight ratio of MO_2/Pt=~1 (M=Ti or Zr) the Pt NPs were fully covered within TiO_2 and ZrO_2 layer. The obtained Pt@TiO_2 and Pt@ZrO_2 core-shell samples showed high tolerance of Pt sintering when the samples were subjected to thermal treatment at 400°C for 3 h under air so as to remove the surfactant completely. XRD patterns of the Pt@TiO_2 and Pt@ZrO_2 samples after the heat treatment confirmed the presence of metallic Pt crystals with the face-centered cubic (fcc) structure as well as the existence of TiO_2 and ZrO_2. The reduction peaks in TPR measurement confirmed full reduction of Pt in the Pt@TiO_2 and Pt@ZrO_2 samples. The Pt@TiO_2 and Pt@ZrO_2 NPs were dispersed on Al_2O_3 support to give a Pt loading of 0.8% with dispersion of 39% and 30% for Pt@TiO_2 and Pt@ZrO_2 samples, respectively. The Pt@TiO_2 catalyst showed improved catalytic activity towards CO oxidation per active metal than Pt@ZrO_2 catalyst. It is postulated that TiO_2 could be considered as oxygen reservoir which can provide with oxygen that reacts directly with CO at the metal-

support perimeter and thus promotes CO oxidation. The study was further extended to other catalytic applications by varying the composition of the core as well as the chemical nature of the shell material. Therefore in the next chapter, a more challenging system, namely, bimetallic Ni_9Pt NPs embedded in TiO_2 and ZrO_2 matrix were investigated for dry reforming of methane reaction at high temperatures. The challenges of designing Ni_9Pt@oxide core-shell structure with TiO_2 and ZrO_2 and their tolerance of the structure to the conditions of dry reforming of methane will be discussed.

3.6 References

[1] A. Satyanarayana Reddy, S. Kim, H. Young Jeong, S. Jin, K. Qadir, K. Jung, C. Ho Jung, J. Yeul Yun, J. Yeong Cheon, J.-M. Yang, S. Hoon Joo, O. Terasaki, J. Young Park, *Chemical Communications* **2011**, *47*, 8412-8414.

[2] G. A. Somorjai, J. Y. Park, *Angewandte Chemie International Edition* **2008**, *47*, 9212-9228.

[3] M. Haruta, *Catalysis Today* **1997**, *36*, 153-166.

[4] M. Cargnello, V. V. T. Doan-Nguyen, T. R. Gordon, R. E. Diaz, E. A. Stach, R. J. Gorte, P. Fornasiero, C. B. Murray, *Science* **2013**, *341*, 771-773.

[5] J. J. Pietron, R. M. Stroud, D. R. Rolison, *Nano Letters* **2002**, *2*, 545-549.

[6] D. R. Rolison, *Science* **2003**, *299*, 1698-1701.

[7] X. Zhang, H. Wang, B.-Q. Xu, *The Journal of Physical Chemistry B* **2005**, *109*, 9678-9683.

[8] J.-N. Park, A. J. Forman, W. Tang, J. Cheng, Y.-S. Hu, H. Lin, E. W. McFarland, *Small* **2008**, *4*, 1694-1697.

[9] S. Takenaka, Y. Orita, H. Umebayashi, H. Matsune, M. Kishida, *Applied Catalysis A: General* **2008**, *351*, 189-194.

[10] S. H. Joo, J. Y. Park, C. K. Tsung, Y. Yamada, P. Yang, G. A. Somorjai, *Nat Mater* **2009**, *8*, 126-131.

[11] A. J. Forman, J.-N. Park, W. Tang, Y.-S. Hu, G. D. Stucky, E. W. McFarland, *ChemCatChem* **2010**, *2*, 1318-1324.

[12] L. Li, S. He, Y. Song, J. Zhao, W. Ji, C.-T. Au, *Journal of Catalysis* **2012**, *288*, 54-64.

[13] D.-S. Bae, Han, K.-S. and Adair, J. H., *Journal of the American Ceramic Society* **2002**, *85*, 1321–1323.

[14] S. Takenaka, H. Umebayashi, E. Tanabe, H. Matsune, M. Kishida, *Journal of Catalysis* **2007**, *245*, 392-400.

[15] Y. Wang, Y. Zhai, D. Pierre, M. Flytzani-Stephanopoulos, *Applied Catalysis B: Environmental* **2012**, *127*, 342-350.

[16] Z. Li, L. Mo, Y. Kathiraser, S. Kawi, *ACS Catalysis* **2014**, *4*, 1526-1536.

[17] Y. Hu, Y. Wang, Z.-H. Lu, X. Chen, L. Xiong, *Applied Surface Science* **2015**, *341*, 185-189.

[18] H. Sakai, T. Kanda, H. Shibata, T. Ohkubo, M. Abe, *Journal of the American Chemical Society* **2006**, *128*, 4944-4945.

[19] M. Cargnello, N. L. Wieder, T. Montini, R. J. Gorte, P. Fornasiero, *Journal of the American Chemical Society* **2010**, *132*, 1402-1409.

[20] X. Wang, D. Liu, S. Song, H. Zhang, *Journal of the American Chemical Society* **2013**, *135*, 15864-15872.

[21] P. M. Arnal, M. Comotti, F. Schüth, *Angewandte Chemie International Edition* **2006**, *45*, 8224-8227.

[22] M.-Y. Kim, J.-S. Choi, T. Toops, E.-S. Jeong, S.-W. Han, V. Schwartz, J. Chen, *Catalysts* **2013**, *3*, 88.

[23] S. Bagheri, N. Muhd Julkapli, S. Bee Abd Hamid, *The Scientific World Journal* **2014**, *2014*, 21.

[24] J.-D. Grunwaldt, M. Maciejewski, O. S. Becker, P. Fabrizioli, A. Baiker, *Journal of Catalysis* **1999**, *186*, 458-469.

[25] S. J. Tauster, S. C. Fung, R. L. Garten, *Journal of the American Chemical Society* **1978**, *100*, 170-175.

[26] B. Coq, in *Metal-Ligand Interactions in Chemistry, Physics and Biology* (Eds.: N. Russo, D. R. Salahub), Springer Netherlands, Dordrecht, **2000**, pp. 49-71.

[27] E. Gharibshahi, E. Saion, *International journal of molecular sciences* **2012**, *13*, 14723-14741.

[28] J. W. Guo, T. S. Zhao, J. Prabhuram, C. W. Wong, *Electrochimica Acta* **2005**, *50*, 1973-1983.

[29] M. E. Manríquez, T. López, R. Gómez, J. Navarrete, *Journal of Molecular Catalysis A: Chemical* **2004**, *220*, 229-237.

[30] C. Zhang, H. He, K.-i. Tanaka, *Applied Catalysis B: Environmental* **2006**, *65*, 37-43.

[31] K. Ebitani, H. Hattori, *Bulletin of the Chemical Society of Japan* **1991**, *64*, 2422-2427.

[32] M. A. Vannice, L. C. Hasselbring, B. Sen, *Journal of Catalysis* **1985**, *95*, 57-70.

[33] A. D. Allian, K. Takanabe, K. L. Fujdala, X. Hao, T. J. Truex, J. Cai, C. Buda, M. Neurock, E. Iglesia, *Journal of the American Chemical Society* **2011**, *133*, 4498-4517.

[34] S. Royer, D. Duprez, *ChemCatChem* **2011**, *3*, 24-65.

[35] N. S. Resende, C. A. Perez, J. G. Eon, M. Schmal, *Catalysis Letters* **2011**, *141*, 1685-1692.

[36] M. Bär, C. Zülicke, M. Eiswirth, G. Ertl, *The Journal of Chemical Physics* **1992**, *96*, 8595-8604.

CHAPTER 4

4. Oxide coating (TiO_2 or ZrO_2) on Ni_9Pt NPs by reverse micro-emulsion for dry reforming of methane

4.1. Graphical abstract

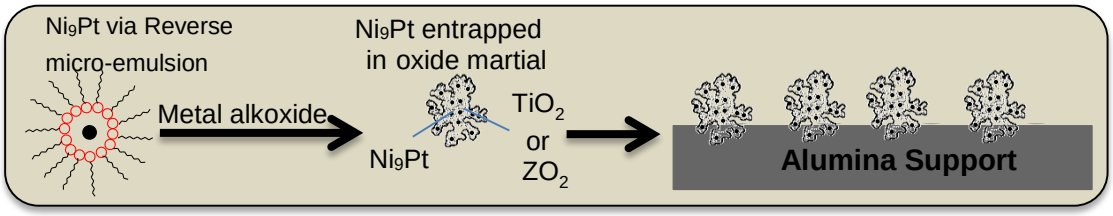

4.2. Introduction

Syngas production is gaining increasing attention in the oil/gas industry, as it is an essential feedstock for producing useful chemicals such as synthetic petroleum, methanol[1] or dimethyl ether[2-4]. Methane reforming is one of the most economical technologies to produce syngas (H_2 and CO). There are different processes to reform methane either by H_2O (steam reforming),[5] O_2 (partial oxidation),[6] or CO_2 (dry reforming). [6-8] Dry reforming of methane is environmentally attracting between these various methane-reforming technologies since it consumes greenhouse gases[9-10] (CH_4 and CO_2) and also gives the best H_2/CO ratios for Fischer-Tropsch synthesis[1, 6, 8, 11] by the following reaction Eq. (1):

$$CH_4 + CO_2 \rightarrow 2H_2 + 2\,CO \qquad \Delta H = +247\ kJ\ mol^{-1} \qquad (1)$$

However, the main drawback of dry reforming process is coke formation,[12] which deactivates the catalysts and plugs the reactor. Coke is generated through methane dissociation Eq. (2) and CO disproportionation reactions Eq. (3).[11, 13]

$$CH_4 \rightarrow C + 2H_2 \qquad \Delta H = +75\ kJ\ mol^{-1} \qquad (2)$$

$$2CO \leftrightarrow C + CO_2 \qquad \Delta H = -173\ kJ\ mol^{-1} \qquad (3)$$

It was previously reported that the coke formation can be reduced by performing dry reforming of methane at high temperature (≈900 °C).[7, 13-14] Yet high-temperature operation condition is industrially unfavorable and gives low catalyst lifetime due to sintering of the metallic particles. Sintering of metal NPs can occur due to crystallite or atoms migration on the surface of the support;[15-16] it will not only reduce the activity of the catalyst, by lowering the number of active surface atoms available but it will also build up large size particles that favor coke formation.[17]

The common metals used for the dry reforming reaction are Rh, Ru, Pt, Ni [6, 10, 18-20] and Co and they are usually supported on thermal stable metal oxide such as alumina, zirconia or silica, or others mixed oxides.[4, 12-13] Noble metals (Rh, Ru, Pt) are known to form less coke and to be more active compared with the non-noble metals (Ni and Co).[18] However, their cost and limited availability make them non affordable, impractical catalyst for industrial scale. Accordingly, catalysts based on Ni or Co is the favorable choice for large-scale applications because of

their relatively cheap prices and high activity.[7] Nevertheless, they are sensitive to high temperature and more subject to sintering since they have lower melting points than the noble metals.[21] Moreover, it has been reported in the literature that carbon rate formation is highly influenced by the Ni particles size. It requires four to six Ni atoms ensembles to grow filamentous carbon suggesting that carbon deposition can be avoided by smaller Ni particles.[2, 17, 22-23]

Therefore, entrapment of Ni NPs in a thin porous layer of oxide may reduce the extent of sintering at high temperature while preventing the formation of filamentous carbon. Recently, many researchers reported the protection of metal NPs against sintering at high temperature by encapsulation within a porous SiO_2 shell forming core-shell structures for different oxidation and reforming reactions.[24-29] For instance, Han *et al.*[30] showed that supported Ni catalysts coated with additional mesoporous SiO_2 layer were resistant for coke and sintering under DRM conditions. However, SiO_2 is well-known to be unstable under the steam condition; besides, SiO_2 is relatively an inert oxide that follows a mono-functional pathway (purely metallic activation of both CO_2 and CH_4) for the mechanism of DRM, where the metal only activates both reactants leading to carbon formation and deactivation.[31] TiO_2 and ZrO_2 materials, on the other hand, are supposed to go through bi-functional mechanism: CH_4 decompose on the metal, and CO_2 adsorbs first on the oxide.[11, 32] The adsorb CO_2 then dissociate close to the metal and metal oxide interface forming CO and O, the latter can be utilized for the oxidation of C generated from CH_4 decomposition. The balance between these two reactions sets the stability of the catalysts.[32-34] ZrO_2 is

amphoteric in nature, contains weak Lewis acid and weak basic sites, where the Lewis acid sites are supposed to increase the interaction with metal at metal-ZrO_2 interface, and Lewis base sites promote the activation of CO_2.[33, 35-36] As results, ZrO_2 would facilitate the oxidation of carbon dissociated from CH_4 on the metal surface and thus reduce amount of coke.[33, 37] Additionally, reducible oxide such as TiO_2 contain oxygen vacancies that can accommodate oxygen from CO_2, which would also promote the oxidation of the accumulated carbon from methane dissociation.[37]

Minimizing the distance at the metal-support boundaries facilitate the diffusion of the adsorbed reactant species over the surface between the metal and support.[38] The interaction at the metal-support perimeter can be altered by reducing the particle size of metal or support.[38] For example, Wei et al.[39] reported that the use of 6 nm fine particle of $Zr(OH)_2$ as support for the Ni/ZrO_2 catalyst had enhanced the reduction of coke formation and also the activity for dry reforming of methane remarkably with no deactivation during 600 h compared with 18 nm particle size of $Zr(OH)_2$ support that deactivated rapidly (26% activity loss after 50h). Another possible way to increase the interaction at metal-support perimeter is embedding the metal support in theses oxides matrix. Few researches[40-41] have successfully entrapped noble metal NP within porous TiO_2 or ZrO_2 matrix due to their rapid hydrolysis which makes it challenging to control the coating of these oxide on the metal NPs. However, the entrapment of Ni NPs in TiO_2 or ZrO_2 layer have not been reported.

Therefore, herein we report the successful synthesis of embedded Ni_9Pt

bimetallic NPs within TiO_2 and ZrO_2 matrix via reverse micro-emulsion procedure. Reverse micro-emulsion method consists in the formation of nano-size droplets of water in a mixture of organic solvent (cyclohexane) and surfactant (IGEPAL CO-520). In these colloids the polar end of the surfactant molecule is directed inside the interior part of the colloid so that water molecules can be selectively entrapped inside the micelle (**Figure 24B**). To precisely control the size and thickness of the metal@oxide NPs, different parameters play a role in this synthesis, such as the surfactant and organic solvent type, water/surfactant molar ratio, pH, metal oxide/metal molar ratio and reducing agent. [42-44] This paper will discuss the challenges of designing embedded Ni_9Pt@oxide structure with different oxides (TiO_2 and ZrO_2) and their tolerance to the conditions of dry reforming of methane.

4.3. Material and methods

4.3.1 Chemicals

The following chemicals were used as received: Cyclohexane (GPR REACTAPUR®100%, VWR chemicals), IGEPAL®CO-520 (Sigma Aldrich) Polyoxyethylene (5) nonylphenylether a nonionic surfactant also referred to as (NP5), ethanol (absolute ³ 99.8, Sigma Aldrich), nickel (II) nitrate hexahydrate (99.999% Sigma Aldrich), platinum (IV) chloride (³ 99.9%, Sigma Aldrich), hydrazine monohydrate (64%, Sigma Aldrich), titanium (IV) butoxide (97%, Sigma Aldrich), zircounium (IV) butoxide (76%-80% in n-butanol, Stream chemicals) and sodium hydroxide (≥97.0%, pellets). ɣ-Alumina pellets (bimodal, Alfa Aesar) was

crushed to a fine powder and calcined at 850°C for 12 h before used. 18.2 MΩ.cm deionized water was used.

4.3.2 Ni_9Pt NP synthesis

First, (186 mg / 640 µmol) nickel nitrate and (22 mg / 65 µmol) platinum (IV) chloride was dissolved in 3.5 ml water to prepare the stock solution of Ni and Pt salts. Then, two sets of reverse micro-emulsion solutions were prepared and both contain 17.2 mg NP5 and 54 ml cyclohexane. 3.5 ml of Ni and Pt stock solution was added to micro-emulsion solution I and a mix solution containing hydrazine (575 µL), NaOH (1 M, 2 mL) and 1 mL of water was added to the micro-emulsion solution II. The molar ratio of NP5/water/cyclohexane in both micro-emulsion mixtures was fixed to (1/5/17 molar ratio). Before mixing the two micro-emulsion solutions together, they were separately stirred until a transparence mixture was obtained thus the stability of the micro-emulsion was reached. After that, the two micro-emulsion solutions were mixed and the transparent greenish micro-emulsion turns to black after one day upon stirring indicating the formation of bimetallic NPs.

4.3.3 $Ni_9Pt@TiO_2$ and $Ni_9Pt@ZrO_2$ NPs synthesis

To coat the Ni_9Pt with a TiO_2 or ZrO_2 layer, an adequate amount of titanium (IV) butoxide or zircounium (IV) butoxide was added directly the Ni_9Pt micro-emulsion mixture. For weight ratio of MO_2/ Ni_9Pt= 1 (MO_2= TiO_2 or ZrO_2), 243 µl or 316 µl of titanium (IV) butoxide or zircounium (IV) butoxide was added, respectively

and for the various weight ratios of MO_2/ Ni_9Pt= 0.2, 60.7 µl or 31.6 µl of titanium (IV) butoxide or zircounium (IV) butoxide was added, respectively. The metal (IV) butoxide was left to hydrolyze in the micro-emulsion solution for 1 day under continuous stirring. Next, Ni_9Pt/MO_2 micro-emulsion mixture was divided into two sections: the first one was kept for the Alumina deposition and the second portion was separated by centrifugation, the resulting powder was washed twice with cyclohexane and twice with ethanol. Later, the Ni_9Pt/MO_2 powder was dried in the oven at 120°C overnight and then calcined in a conventional oven at 400°C for 3 h with a heating ramp of 2°C/min. The reduction (4% H_2 in 98% He) was performed at 800°C for 3 h with a heating ramp of 10°C/min.

4.3.4 Deposition of $Ni_9Pt@TiO_2$ and $Ni_9Pt@ZrO_2$ NPs on Al_2O_3

To get 5% Ni_9Pt metal and 1% TiO_2 or ZrO_2 loading on Alumina, 500 mg of Alumina were added directly to the half remaining (Ni_9Pt/TiO_2 or Ni_9Pt/ZrO_2) micro-emulsion mixture, which contain 25 mg of Ni_9Pt NPs. They were left under vigorous stirring for 1 day to allow the $Ni_9Pt@TiO_2$ or $Ni_9Pt@ZrO_2$ NPs to completely deposit on the Alumina. Then, the powders were collected by centrifugation and washed twice with cyclohexane and twice with the ethanol to remove the surfactant. After that, the samples were dried at 120°C overnight and calcined at 400°C for 3 h with heating ramp of 2°C/min. Finally, the samples were reduced (4% H_2 in 98% He) at 800°C for 3 h with a heating ramp 10°C/min. The metal loading was confirmed by elemental analysis.

4.3.5 Characterization

The synthesized Ni_9Pt/TiO_2 and Ni_9Pt/ZrO_2 samples were characterized by transmission electron microscopy (TEM) before and after deposition on Alumina to study the existence of a core shell structure without the support and obtain the particle size distribution. Two TEM machines were mainly used for the characterization namely a TITAN ST and a TECNAI SPIRIT (FEI company), operating at 300kV and 120kV respectively. X-ray energy dispersive spectroscopy (EDS) was used under the scanning transmission electron microscopy (STEM) mode with a 1 nm spot size to capture the profile of element composition. The specimens were prepared for the TEM by dissolving the sample in ethanol and placing a single drop to the TEM grid. The TEM grid that was used is carbon film on 300 mesh copper grids.

The X-ray diffraction (XRD) patterns of the catalysts were recorded before and after the catalytic tests on a Bruker DMAX 2500 X-ray diffractometer with Cu Kα radiation (λ=0.154 nm). The amount of coke after dry reforming of methane was measured using a Flash 2000 Thermo Scientific CHNS/O elemental analyzer.

Temperature program oxidation (TPO) was used to measure the amount of carbon accumulated on the catalysts surface after DRM run. The experiment carried out in 1% O_2 in He with 20 mL/min flow rate. The carbon amount was estimated from the CO_2 and CO released by carbon oxidation and detected by flame ionization detector (FID).

Temperature program reduction (TPR) was used to study the reducibility of the catalysts after calcination at 400°C for 3 h. The samples were heated from 40°C to 800°C with a ramp of 10°C/min under 4%H_2 in He with 20 mL/min flow rate. Thermal conductivity detector (TCD) was used to record the signals.

4.3.6 Catalytic test

Dry reforming of methane reaction was performed on the synthesized catalysts in a stainless steel fixed bed reactor (9 mm i.d). Approximately 50 mg of the reduced Al_2O_3 supported samples were diluted with 150 mg of SiC (0.250 mm) as inert particles. The catalysts were heated up in flowing N_2 (80 ml/min) with heating ramp of 5°C/min until they reach 700°C and they were then reduced (20 ml/min H_2 in 80ml/min N_2) for 30 min. Then, the temperature was increased again under flowing N_2 to reach 750°C, which is the temperature at which the dry reforming of methane was performed. The conditions that were used for dry reforming of methane are 750°C, $CH_4/CO_2/N_2$= 1/1/8, WHSV= 120 $L.h^{-1}.g^{-1}$.

4.4. Results and discussion

4.4.1 Structural characterization

Ni_9Pt alloy NPs with uniform size were synthesized first via micro-emulsion method (Figure 24**A**) to form NPs with the size of 3.4±1.5 nm (**Figure 25**). The Ni_9Pt alloy NPs have grown (~ 20 nm) after reduction at 800°C (**Figure 26**) thus these NPs need protection against sintering at high temperature. The first part of

our study was the synthesis of $Ni_9Pt@TiO_2$ and $Ni_9Pt@ZrO_2$ with a weight ratio of $MO_2/Ni_9Pt=1$ (M= Ti or Zr). The weight ratio of $MO_2/Ni_9Pt= 1$ was selected, to get identical amount of oxide to the amount of Ni_9Pt NPs (same ratio as $Pt@MO_2$ from chapter 3). An adequate amount of metal alkoxide ($Ti(OC_4H_9)_4$ or $Zr(OC_4H_9)_4$) were added to the Ni_9Pt (50 mg) micro-emulsion solutions to produce metal oxide TiO_2 or ZrO_2, respectively. The Ni_9Pt $@MO_2$ (M=Ti or Zr) samples were further subjected to thermal treatment at 400°C for 3 h under air to remove the surfactant completely which was confirmed by TGA (data of TGA not shown). TEM micrograph was performed on the $Ni_9Pt@TiO_2$ and $Ni_9Pt@ZrO_2$ NPs without alumina support samples to clearly observe the structure and morphology of the NPs. TEM images of $Ni_9Pt@TiO_2$ and $Ni_9Pt@ZrO_2$ NPs after calcination at 400°C for 3 h are represented in (**Figure 27**) and (**Figure 28**), respectively. The TEM images showed uniform Ni_9Pt NP with size of 6 nm that were mono-dispersed and embedded within amorphous oxide structure. The Ni_9Pt NP were completely surrounded and covered by excessive amount of the oxides. The samples heated were subsequently treated in H_2 at 800°C for 3 h. The 800°C was selected because the supported catalysts had been activated under H_2 at 800°C before testing them for DRM at 750°C. **Figure 29** and **Figure 30** show the TEM and STEM images of $Ni_9Pt@TiO_2$ and $Ni_9Pt@ZrO_2$ NPs, respectively after reduction at 800°C. TEM and STEM images (**Figure 29)** of $Ni_9Pt@TiO_2$ show the formation of encapsulated large spherical NPs (2-20 nm) within long crystalline nanorods (width= 0.1-0.4 µm). EDX analysis under STEM mode (**Figure 29D**) indicates that these nanorods are TiO_2 and the encapsulated NPs are Ni_9Pt alloy. Apparently, the TiO_2 material in

the $Ni_9Pt@TiO_2$ sample had sintered at high temperature under reducing atmosphere forming nanorods. The TEM and STEM images (**Figure 30**) of $Ni_9Pt@ZrO_2$ display crystalline material with irregular structures encapsulating spherical NPs. From EDX analysis under STEM mode (**Figure 30D**), it was confirmed that theses crystalline material are ZrO_2 embedding Ni_9Pt NPs alloy (5-25 nm). The sintering of ZrO_2 in the $Ni_9Pt@ZrO_2$ sample was slightly less than the TiO_2 but still the ZrO_2 aggregated forming irregular structures. Therefore, the amount of ZrO_2 and TiO_2 was reduced giving a weight ratio of MO_2/Ni_9Pt= ~0.2 to avoid the oxide sintering.

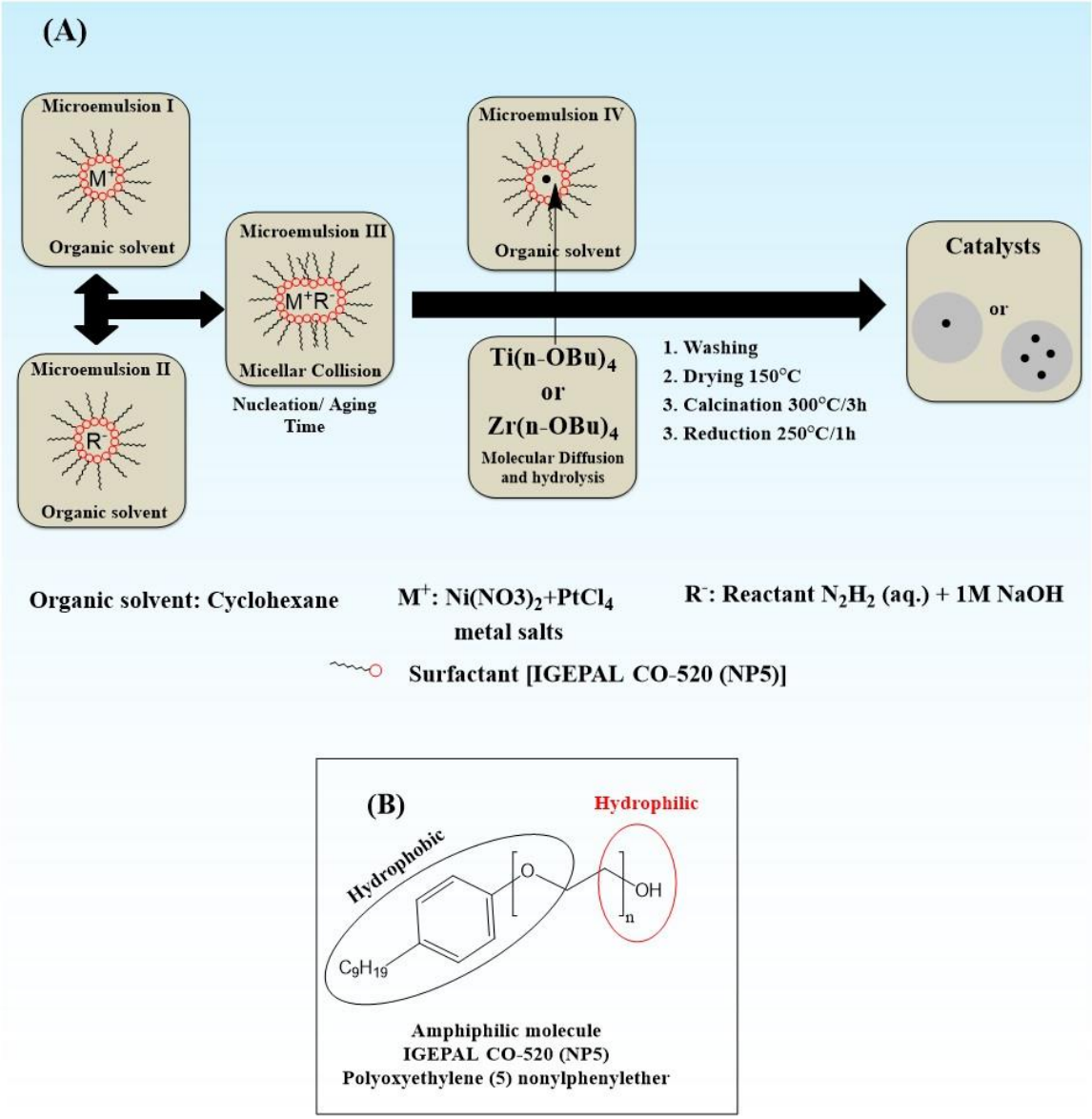

Figure 24. (A) Diagram of the general methodology of $Ni_9Pt@TiO_2$ or $Ni_9Pt@ZrO_2$ synthesis via reverse micro-emulsion procedure (B) IGEPAL CO-520 (NP5) surfactant structure used in this synthesis.

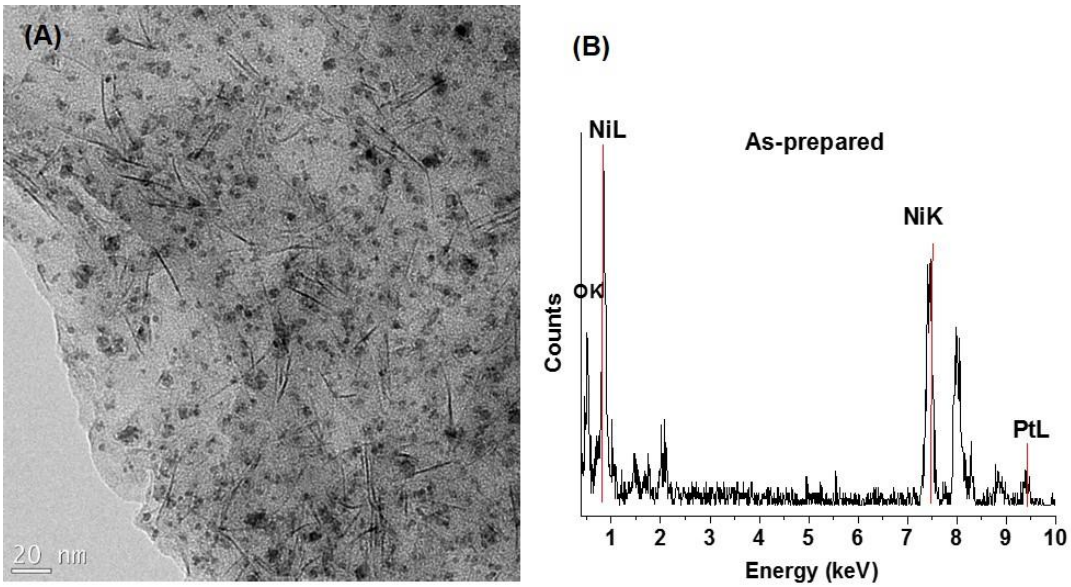

Figure 25. HRTEM images of Ni_9Pt NPs as prepared (A) together with EDX elemental survey (B).

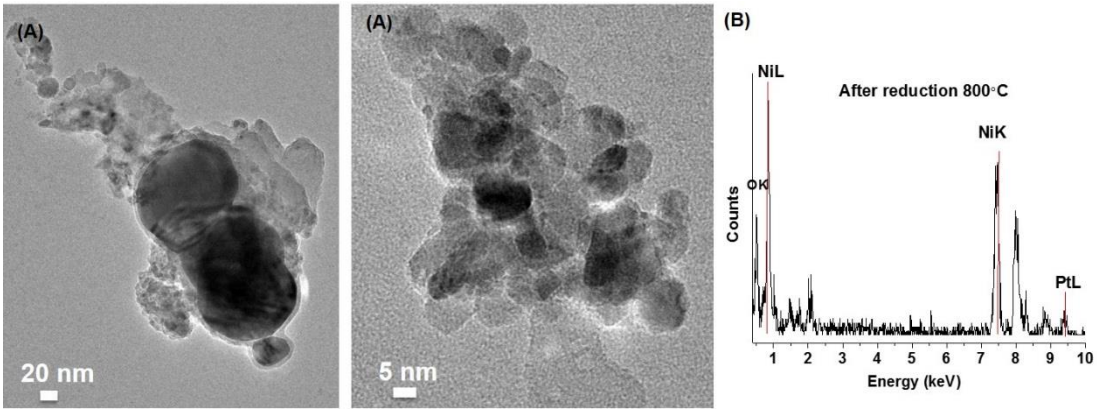

Figure 26. HRTEM images of Ni_9Pt NPs after reduction at 800°C for 3 h (A) together with EDX elemental survey (B).

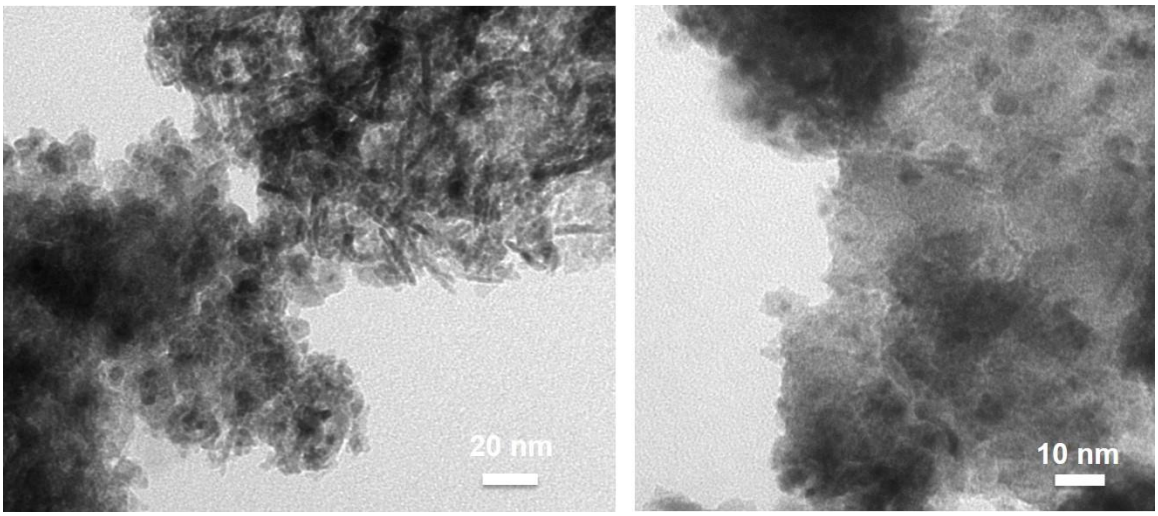

Figure 27. HRTEM images of $Ni_9Pt@TiO_2$ NPs (weight ratio=TiO_2/Ni_9Pt=1) after calcination at 400°C for 3 h.

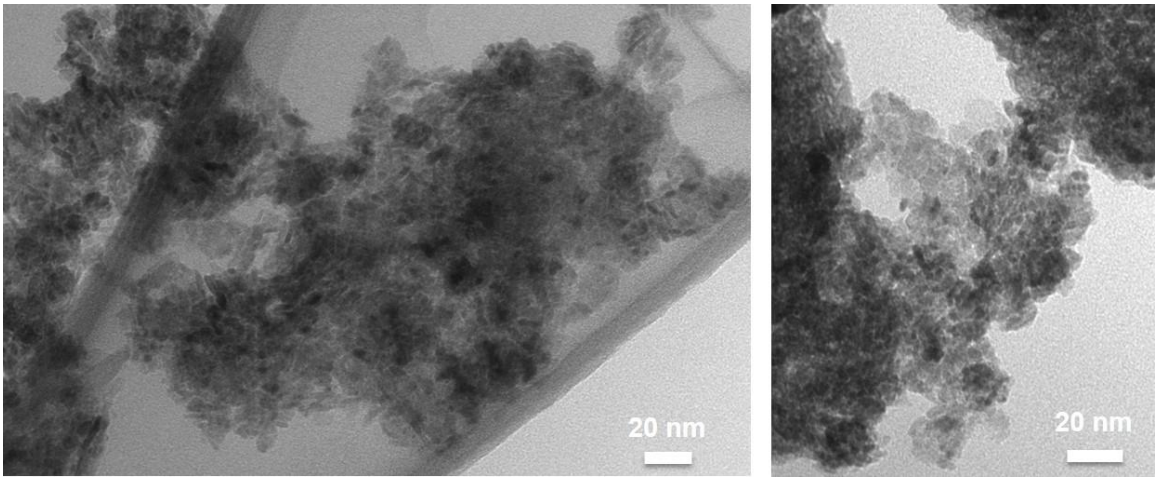

Figure 28. HRTEM images of $Ni_9Pt@ZrO_2$ NPs (weight ratio=ZrO_2/Ni_9Pt=1) after calcination at 400°C for 3 h.

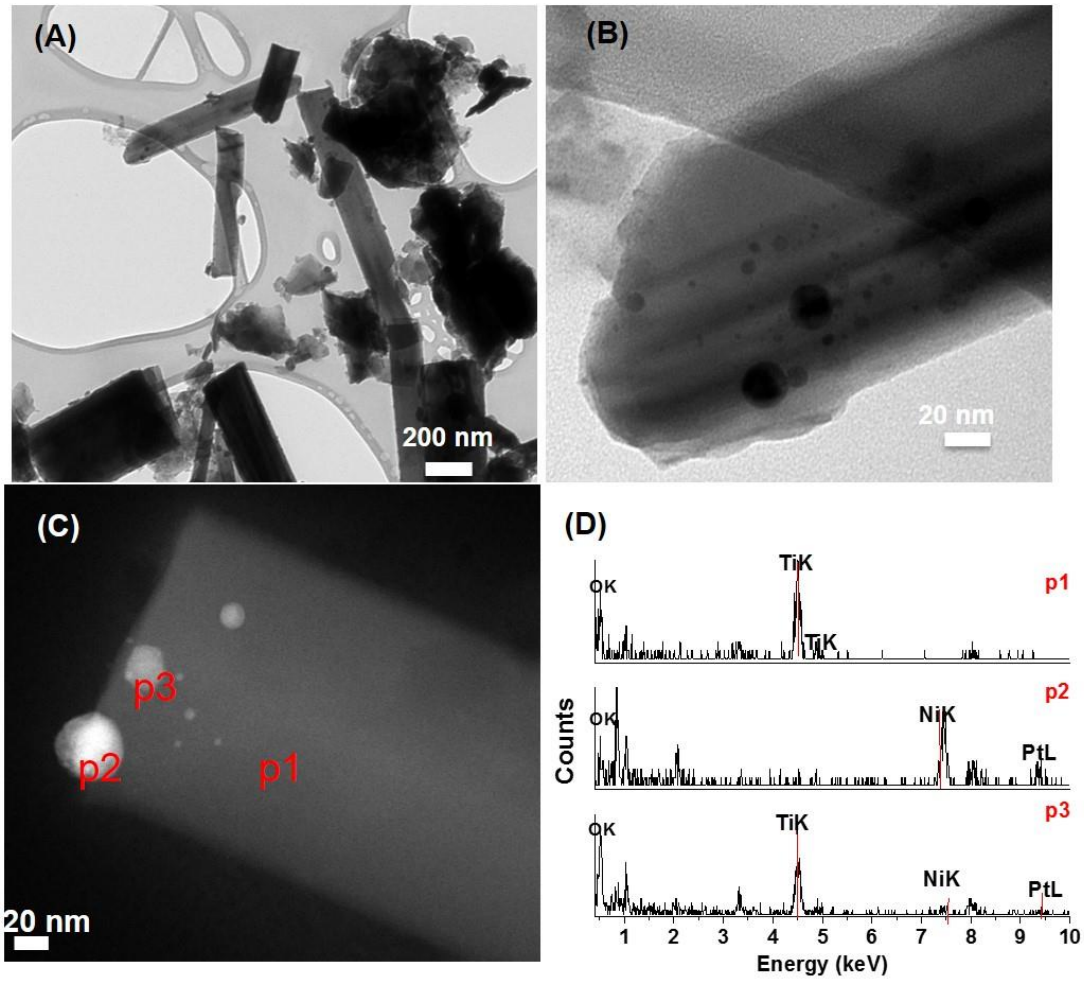

Figure 29. HRTEM images of $Ni_9Pt@TiO_2$ NPs (weight ratio=TiO_2/Ni_9Pt=1) after reduction at 800°C for 3 h (A) low magnification (B) high magnification (C) STEM image of the same sample along with (D) spot EDX analysis.

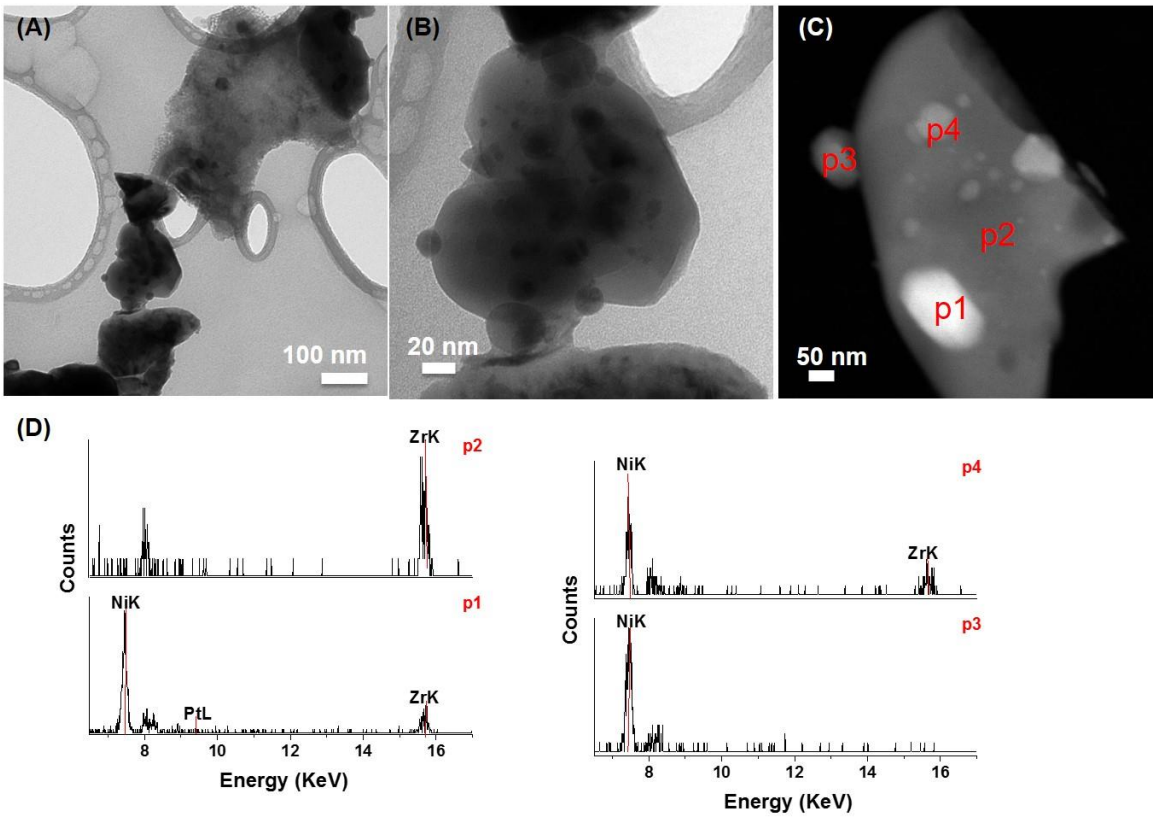

Figure 30. HRTEM images of $Ni_9Pt@ZrO_2$ NPs (weight ratio=ZrO_2/Ni_9Pt=1) after reduction at 800°C for 3 h (A) low magnification (B) high magnification (C) STEM image of the same sample along with (D) spot EDX analysis**.**

Figure 31 shows the TEM, STEM images and EDX of $Ni_9Pt@TiO_2$ NPs, (TiO_2/Ni_9Pt weight ratio= 0.2) after calcination at 400°C for 3 h. TEM and STEM images show core-shell nanostructures. EDX analysis under STEM mode (**Figure 31D**) confirms that the formation of NiPt alloy in core, however, both Ti and Ni were found in the shell layer. It is assumed that part of the Ni were oxidized and segregated from Ni_9Pt alloy as NiO forming a shell layer around this Ni_9Pt alloy. The small amount of TiO_2 oxide had incorporated within the NiO shell; as a result, small aggregated of NiO-TiO_2 oxides were surrounding the Ni_9Pt alloy NPs giving

a core-shell structure. Also, some of the TiO_2 aggregates were deposited away from Ni_9Pt NPs due to the rapid hydrolysis of titanium (IV) butoxide. The mean size of the Ni_9Pt NPs was 3±1.7 nm. There were some large Ni_9Pt NPs that were aggregated before the addition and incorporation of the TiO_2 NPs around them, which explain the wide particles size distribution. Next, the $Ni_9Pt@TiO_2$ (TiO_2/Ni_9Pt weight ratio= 0.2) sample was reduced in H_2 at two different temperature, namely, 400°C and 800°C for 3 h to understand better the effect of reduction temperature on the $Ni_9Pt@TiO_2$ sample. After reduction at 400°C for 3 h, Ni_9Pt NPs were embedded in TiO_2 matrix and the core-shell structure did not exist any longer due to the reduction of NiO shell (**Figure 32A**). Increasing the reduction to 800°C has produce denser TiO_2 material (**Figure 32B**), however, the Ni_9Pt NPs were still embedded in TiO_2 matrix.

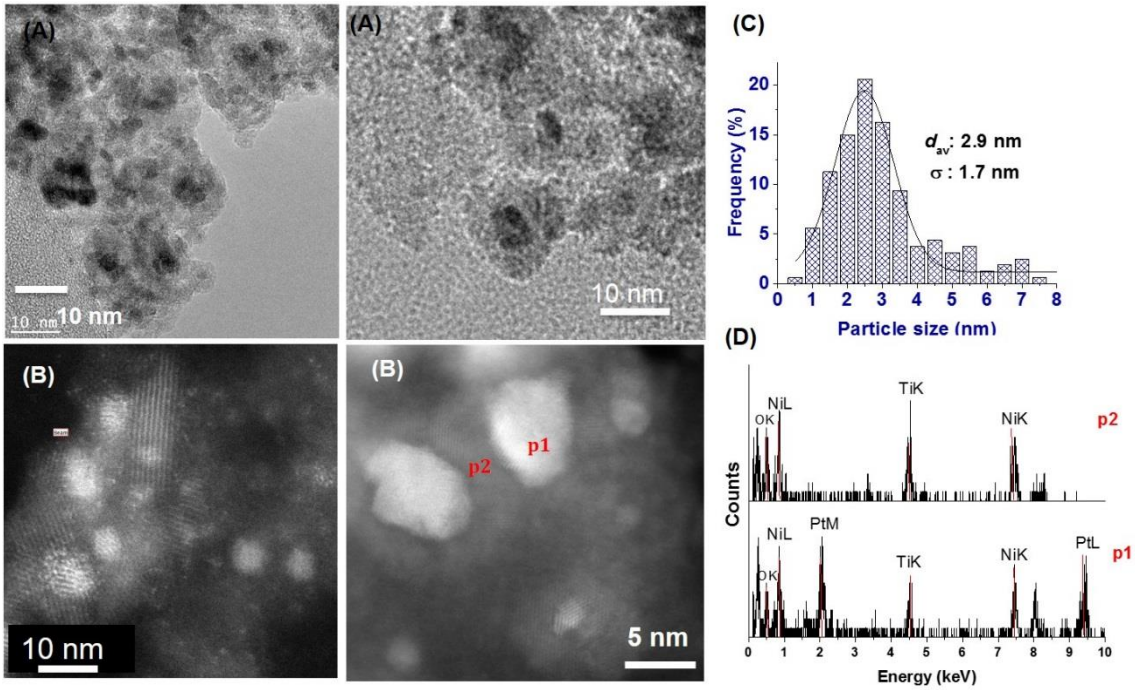

Figure 31. HRTEM images of $Ni_9Pt@TiO_2$ NPs (weight ratio=TiO_2/Ni_9Pt=0.2) after calcination at 400°C for 3 h (A) together with histogram of Ni_9Pt particle size distribution (C). STEM images of the same sample along with (B) spot EDX analysis (D).

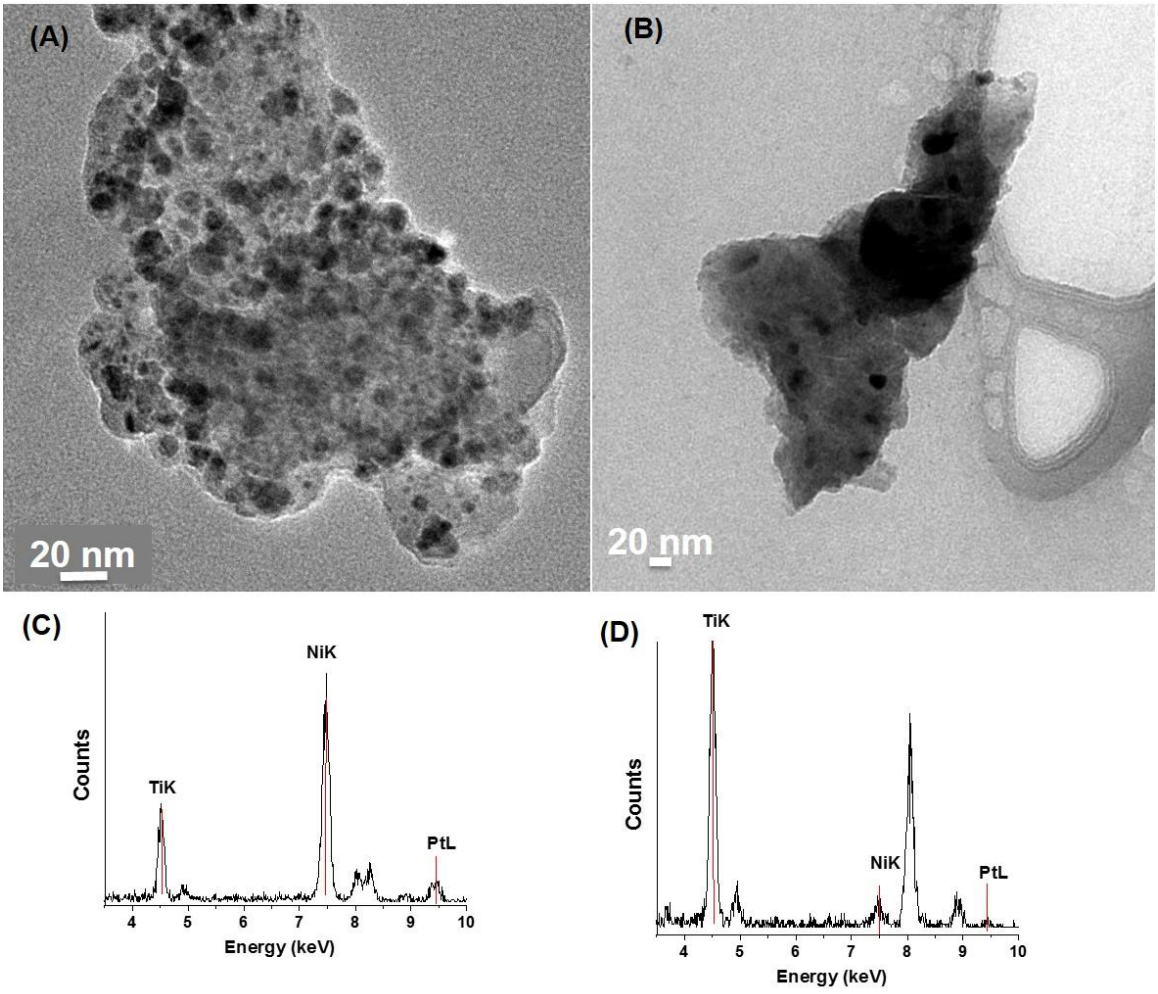

Figure 32. HRTEM images of $Ni_9Pt@TiO_2$ NPs (weight ratio=TiO_2/Ni_9Pt=0.2): after reduction at 400°C for 3 h (A) together with EDX elemental survey (C) after reduction at 800°C for 3 h (B) together with EDX elemental survey (D).

TEM and STEM images of $Ni_9Pt@ZrO_2$ NPs, (ZrO_2/Ni_9Pt ratio= ~0.2) after calcination at 400°C for 3 h are shown in (**Figure 33**). TEM and STEM images showed a more defined core-shell structure than with the $Ni_9Pt@TiO_2$ sample. The size of Ni_9Pt alloy NPs was 2.1±0.75 nm. The EDX analysis under STEM mode (**Figure 33D**) indicates that only NiO oxide shell was surrounding the Ni_9Pt alloy

and no trace of ZrO_2 within the oxide shell. That means that the ZrO_2 NPs did not incorporate in the NiO shell which might explain the uniform and more defined core-shell structure of Ni_9Pt@NiO compared with core-shell of Ni_9Pt@NiO-TiO_2. Apparently, the ZrO_2 NPs segregated away or next to Ni_9Pt@NiO NPs. To make sure that the Ni_9Pt alloy NPs incorporate within ZrO_2 matrix, the sample was only reduced in H_2 at 400°C for 3 h without calcination at air (**Figure 34**). Under reducing atmosphere, the Ni_9Pt alloy NPs was embedded within the ZrO_2 matrix forming embedded Ni_9Pt@ZrO_2 structure.

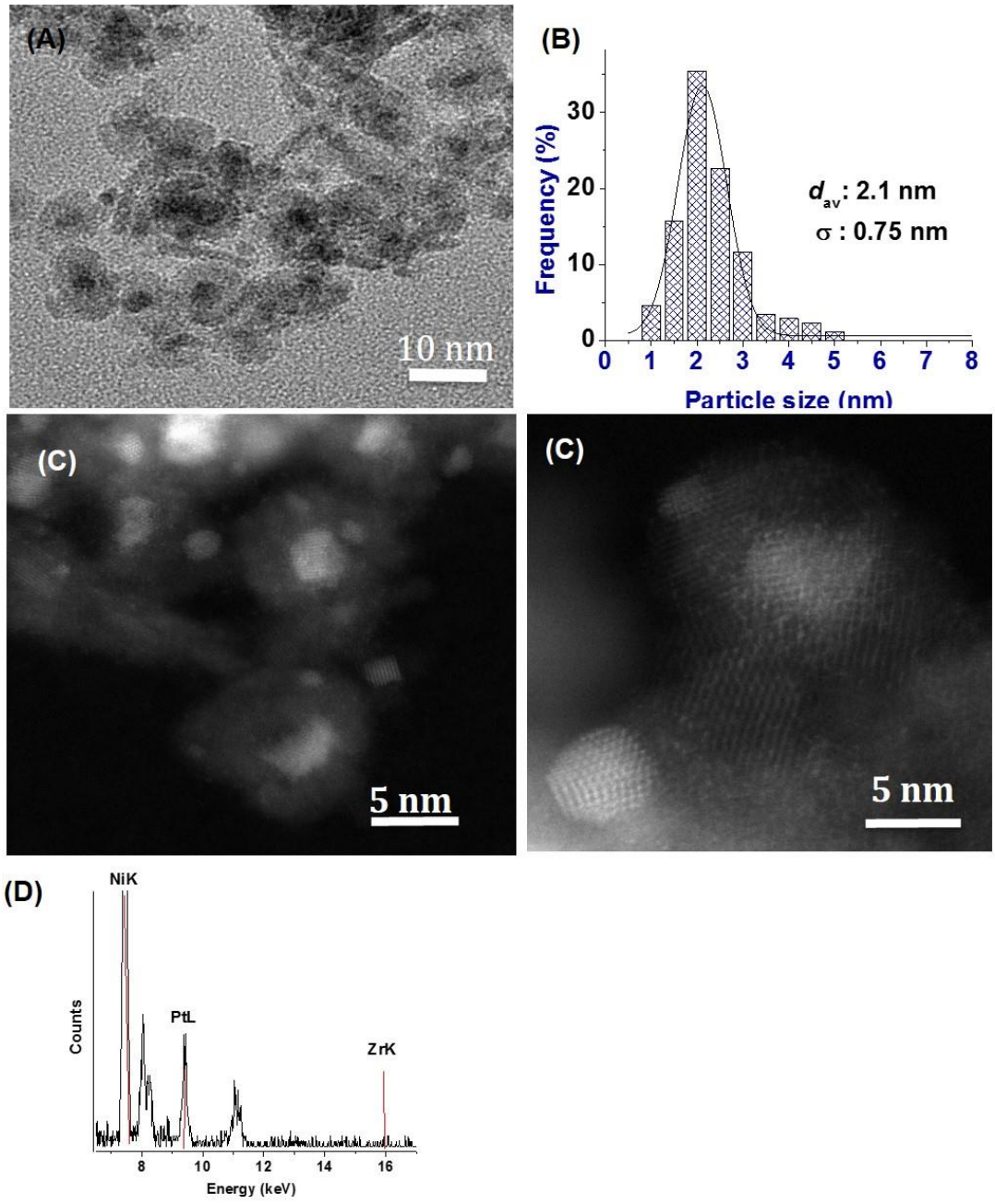

Figure 33. HRTEM images of $Ni_9Pt@ZrO_2$ NPs (weight ratio=ZrO_2/Ni_9Pt=0.2) after calcination at 400°C for 3 h (A) together with histogram of Ni_9Pt particle size distribution (B). STEM images of the same sample (C) together with EDX elemental survey (D).

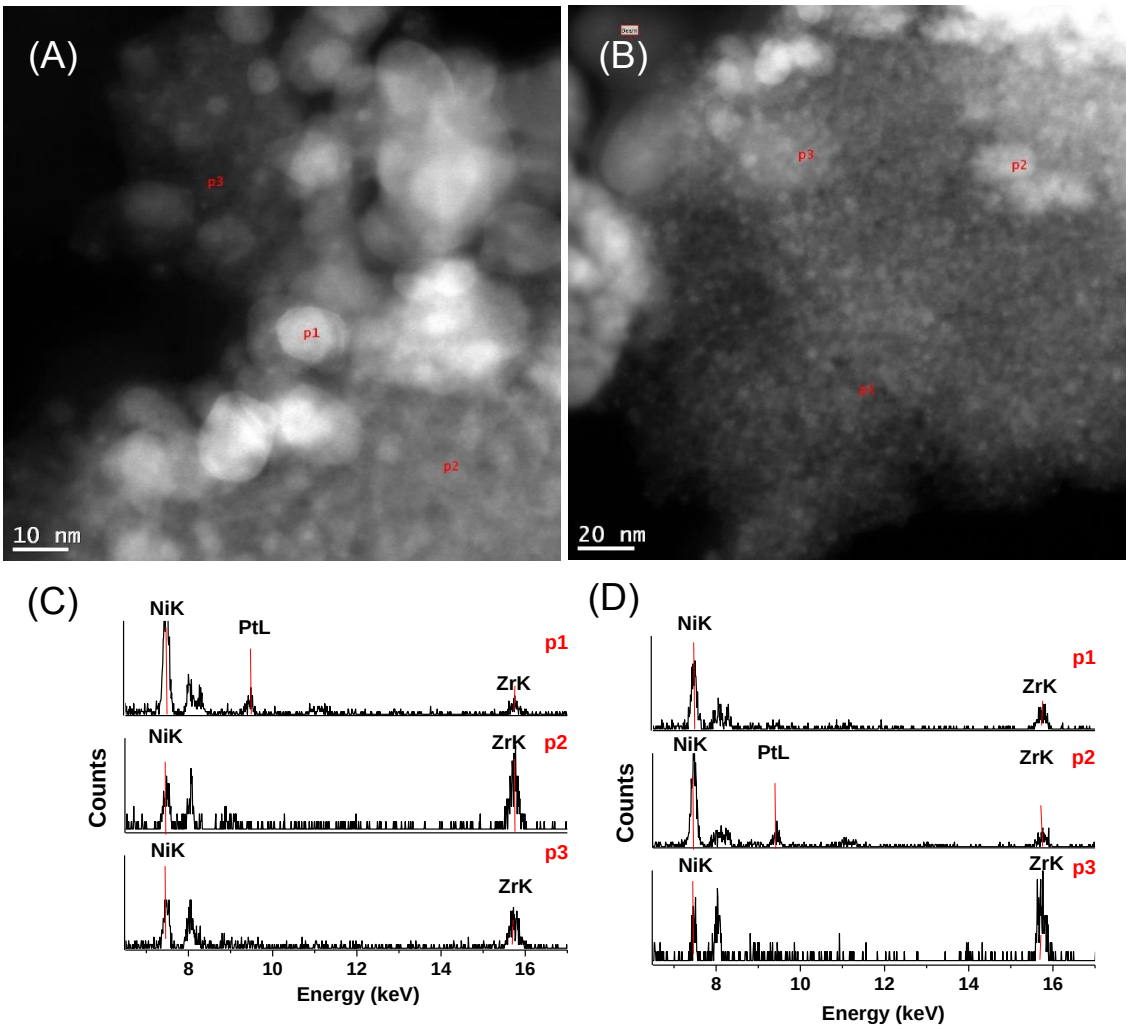

Figure 34. STEM images of $Ni_9Pt@ZrO_2$ NPs (weight ratio=ZrO_2/Ni_9Pt=0.2): (A),(B) after reduction at 400°C for 3 h (C),(D) together with EDX elemental survey.

Figure 39A illustrates the temperature program reduction (TPR) profiles of the Ni_9Pt (without TiO_2 or ZrO_2), $Ni_9Pt@TiO_2$ and $Ni_9Pt@ZrO_2$ (MO_2/Ni_9Pt ratio= ~0.2) NPs calcined at 400°C for 3 h without alumina support. In the case of Ni_9Pt alloy without TiO_2 or ZrO_2, It shows that the metal NPs were completely reduced at 450°C, and also confirmed the formation of bimetallic Ni_9Pt alloy. Tomishige [45]

and de Miguel [46] reported that the addition of Pt reduces and stabilizes the reduction temperature of Ni NP which is usually ^{3} 650°C. Similarly, the $Ni_9Pt@ZrO_2$ NPs were all completely reduced at 450°C. The reduction peaks were shifted to 12-55°C to lower temperatures that might indicate an increase of $Ni_9Pt@ZrO_2$ interface sites. Whereas $Ni_9Pt@TiO_2$ sample has two reduction profiles, the main peaks were at 450°C and a small shoulder peak at 674°C. The high temperature reduction peaks might be attributed to H_2 spillover effect where H_2 dissociated on Pt and H radical move to the TiO_2 leading to the strong metal support interaction (SMSI) phenomena which form a kind of intermetallic compound of Ni_9Pt/TiO_2 without knowing its precise structure and or composition.[47]

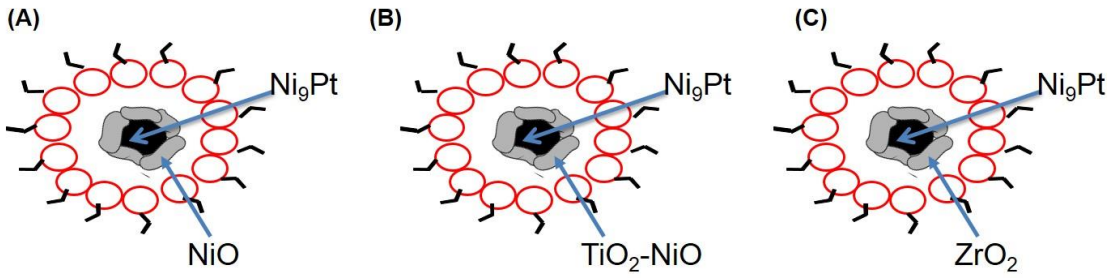

Figure 35. Schematic representation of the structural evolution of Ni_9Pt/MO_X NPs (MO_x=NiO, TiO_2 and ZrO_2) (A) NiO forms a shell around the Ni_9Pt (B) TiO_2 was incorporated in the shell with the NiO (C) ZrO_2 was coating over the Ni_9Pt under reducing atmosphere**.**

The structural evolution of $Ni_9Pt@MO_2$ (M= Ti or Zr) can be explained as follows (**Figure 35**): Ni_9Pt NPs were supposedly formed first in micelles, then, the metal butoxide $M(OC_4H_9)_4$ (M=Ti or Zr) was added which diffuses through the

micelles and starts to hydrolyze once it contacted the water present inside the micelle containing Ni_9Pt NPs. The metal butoxide $M(OC_4H_9)_4$ hydrolyzes rapidly inside the micelles forming aggregates that deposited around the Ni_9Pt NPs. Adding equal amount of metal oxide (M= Ti or Zr) to the Ni_9Pt NPs led to the aggregation and sintering of the oxide and the Ni_9Pt NPs after tje high temperature at 800°C. When the amount of oxide was reduced 5 folds, small part of Ni segregated as NiO shell after calcination under air at 400°C for 3 h. A small amount of TiO_2 was incorporated in NiO shell forming core-shell around the Ni_9Pt@NiO-TiO_2. Under reducing atmosphere, NiO shell is reduced and Ni_9Pt NPs were embedded within the oxide matrix (TiO_2 or ZrO_2) Ni_9Pt@oxide.

4.4.2 Catalytic performance of these Ni_9Pt NPs

To investigate the activity of $Ni_9Pt@TiO_2$ and $Ni_9Pt@ZrO_2$ NPs were dispersed on high surface area thermally stable Al_2O_3 support. Reforming of methane with CO_2 reaction was performed at 750°C for 20 h on the following catalysts: $Ni_9Pt@TiO_2/Al_2O_3$, $Ni_9Pt@ZrO_2/Al_2O_3$ (MO_2/Ni_9Pt weight ratio= 0.2) and Ni_9Pt/Al_2O_3 prepared by reverse micro-emulsion method (Figure 36). The catalytic tests of Ni_9Pt/Al_2O_3 samples were done to compare the performance of unembedded Ni_9Pt NPs with the embedded $Ni_9Pt@TiO_2/Al_2O_3$ and $Ni_9Pt@ZrO_2/Al_2O_3$ catalysts. All catalysts gave excellent initial CH_4 conversions 58, 57 and 69 for Ni_9Pt/Al_2O_3, $Ni_9Pt@TiO_2/Al_2O_3$ and $Ni_9Pt@ZrO_2/Al_2O_3$ respectively (**Figure 36A**). The high activities of the embedded catalysts confirm the accessibility of Ni_9Pt NPs within the oxides layer (TiO_2 and ZrO_2). As for the stability

of the catalysts during 20 h, the $Ni_9Pt@TiO_2/Al_2O_3$ and $Ni_9Pt@ZrO_2/Al_2O_3$ catalysts was maintained at almost constant CH_4 conversion (around 97% stability ratio and were way more stable) compared with the Ni_9Pt/Al_2O_3 sample, which lost 22% of the activity during 20 h (**Table 5**)**.** It is evident that the catalytic activity improved by adding the small amount of ZrO_2 and TiO_2 oxides. These catalytic activity results are in agreement with the data published by Lercher *et al.*[4, 48] were the stability of Pt NPs supported on different oxides decreased in the following order Pt/Al_2O_3>Pt/TiO_2>Pt/ZrO_2. They attribute the deactivation of Al_2O_3 supported catalyst to the Lewis acid sites on Al_2O_3, which prompted the methane dissociation that forms coke very close to the Pt- Al_2O_3 interface which physically block and cover the Pt active sites. Further characterization (TPO, TEM, TPR, and XRD) of the catalysts have been conducted to understand the reason of these catalytic improvements by ZrO_2 and TiO_2 oxides.

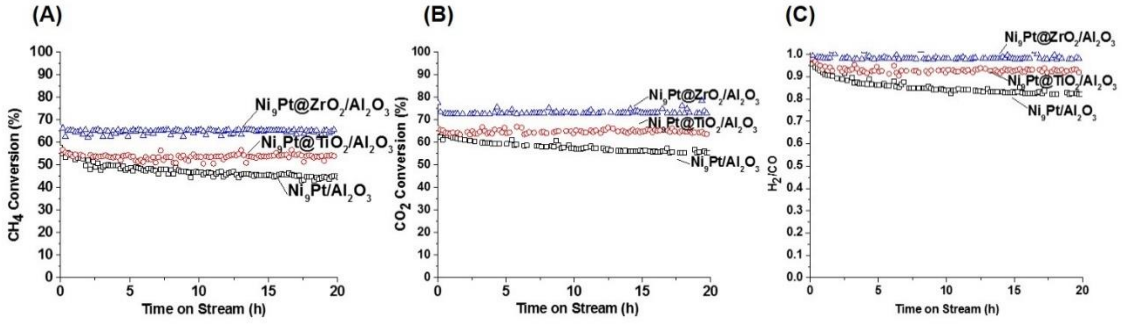

Figure 36. Dry reforming test during 20 h and 50 mg of Ni_9Pt/Al_2O_3 and $Ni_9Pt@MO_2/Al_2O_3$ catalysts (weight ratio=MO_2/Ni_9Pt=0.2) (MO_2= TiO_2 or ZrO_2) diluted with SiC, 750°C, $CH_4/CO_2/N_2$= 1/1/8, WHSV= 120 $L.h^{-1}.g^{-1}$. (A) CH_4 conversion (B) CO_2 conversion (C) H_2/CO ratio. Blue: $Ni_9Pt@ZrO_2/Al_2O_3$, black: Ni_9Pt/Al_2O_3 and red: $Ni_9Pt@ZrO_2/Al_2O_3$.

Table 5. Ni_9Pt content, catalytic performance and coke weight % of Ni_9Pt/Al_2O_3 and $Ni_9Pt@MO_2/Al_2O_3$ catalysts (weight ratio=MO_2/Ni_9Pt=0.2) (MO_2= TiO_2 or ZrO_2) during DRM test[a].

Sample	Ni_9Pt[b] [wt%]	Ni_9Pt [g]	Initial conversion [%]		Initial H_2/CO	Specific CH_4 conversion rate [mol/min.g_{metal}]	CH_4 stability ratio[c] [%]	Carbon[d] [wt%]
			CH_4	CO_2				
Ni_9Pt/Al_2O_3	5.6	0.002	58	65	0.98	0.028	78	0.75
$Ni_9Pt@TiO_2/Al_2O_3$	5	0.002	57	66	0.99	0.027	95	0.2
$Ni_9Pt@ZrO_2/Al_2O_3$	5	0.002	69	80	1	0.032	97	0.64

[a] Reaction conditions: T=750°C, $CH_4/CO_2/N_2$= 1/1/8, WHSV= 120 $L.h^{-1}.g^{-1}$, flow rate=100 $mL.min^{-1}$. [b] Ni_9Pt loading in Al_2O_3-supported measured by ICP for fresh catalyst. [c] Defined as the initial CH_4 conversion with respect to the final one and multiplied by 100. [d] Measured by TPO after DRM.

The Temperature program oxidation (TPO) analysis was conducted to measure the amount of carbon formed on the catalysts after DRM reaction (**Table 5**). The highest carbon amount was formed on the Ni_9Pt/Al_2O_3 catalyst producing 0.75 wt% carbon, whereas $Ni_9Pt@TiO_2/Al_2O_3$ catalyst formed a negligible quantity of carbon on the surface of the catalyst (around 0.2 wt%), which explains its stability during DRM reaction. Additionally, $Ni_9Pt@ZrO_2/Al_2O_3$ did not deactivate though carbon was formed on its surface (0.64 wt%) indicating that the carbon on this catalyst is active (amorphous carbon C_α or filament carbon C_β).[49]

Structural characterization (HRTEM, XRD, and TPR) of supported catalysts $Ni_9Pt@TiO_2/Al_2O_3$, $Ni_9Pt@ZrO_2/Al_2O_3$ and Ni_9Pt/Al_2O_3 were done before and after DRM to understand the reason of catalytic performance improvements of $Ni_9Pt@TiO_2/Al_2O_3$ and $Ni_9Pt@ZrO_2/Al_2O_3$ catalysts compared with Ni_9Pt/Al_2O_3 catalyst. (**Figure 37A**) and (**Figure 38A**) show the TEM image of $Ni_9Pt@TiO_2/Al_2O_3$ and $Ni_9Pt@ZrO_2/Al_2O_3$ after calcination at 400°C for 3 h followed by reduction at 800°C for 3 h and before testing the catalysts in dry reforming reaction. No carbon deposition was observed by TEM for both $Ni_9Pt@TiO_2/Al_2O_3$ and $Ni_9Pt@ZrO_2/Al_2O_3$ catalysts. The average sizes of Ni_9Pt NPs were 4±1.5 nm and 2.4±1.1 nm for $Ni_9Pt@TiO_2/Al_2O_3$ and $Ni_9Pt@ZrO_2/Al_2O_3$, respectively. After performing dry reforming reaction, the size of Ni_9Pt NPs grown significantly in the case of $Ni_9Pt@TiO_2/Al_2O_3$ (**Figure 37B**) with an average size of 8.8±6 nm. However, the size of Ni_9Pt NPs was much smaller in the

$Ni_9Pt@ZrO_2/Al_2O_3$ (average size 4.3±5 nm) (**Figure 38B**). Apparently, coating the Ni_9Pt NPs with ZrO_2 layer has reduced the growth of Ni_9Pt NPs, which is not the case for $Ni_9Pt@TiO_2$. The slight growth of Ni_9Pt NPs in $Ni_9Pt@TiO_2$ might be due to the less thermal stability of TiO_2 than the ZrO_2, which led to sintering of TiO_2. This was also observed by An *et al.*[50] how reported that the Pt NPs in sandwich-type core@shell $SiO_2@Pt@TiO_2$ catalyst went through sintering due to the incomplete protection of the TiO_2 shells during the reaction at 500°C.

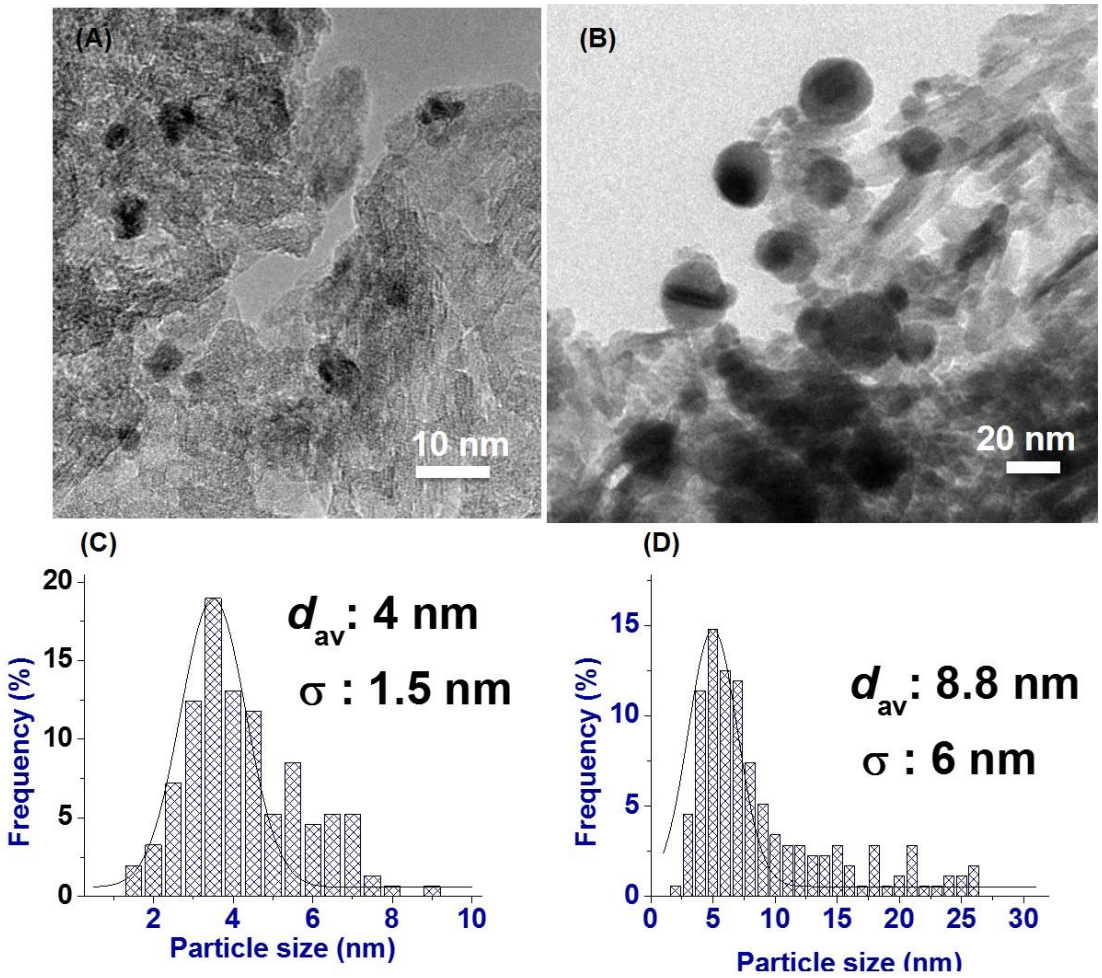

Figure 37. HRTEM images of $Ni_9Pt@TiO_2/Al_2O_3$ NPs (weight ratio=TiO_2/Ni_9Pt=0.2): before DRM and after reduction 800°C for 3 h (A) together with histogram of Ni_9Pt particle

size distribution (C) after DRM test (B) together with histogram of Ni_9Pt particle size distribution (D).

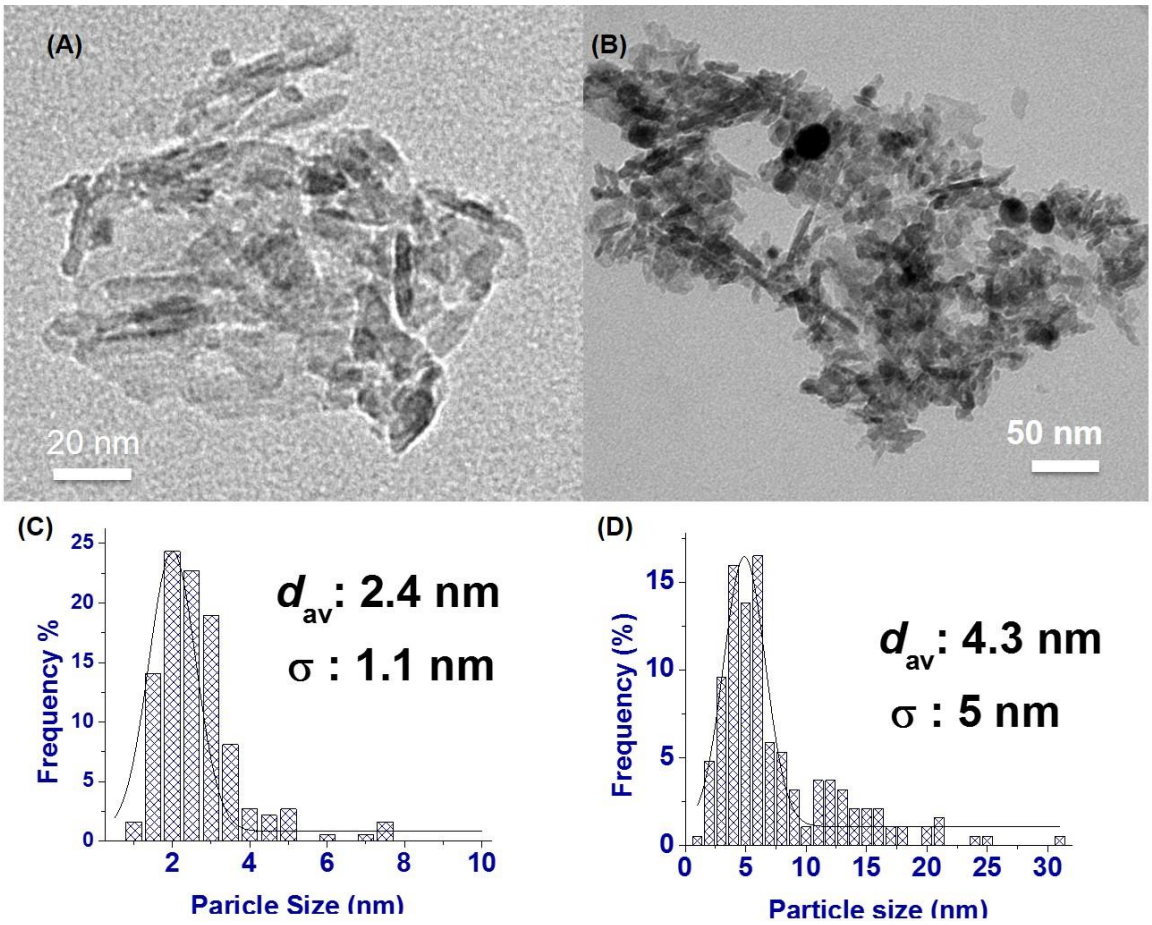

Figure 38. HRTEM images of $Ni_9Pt@ZrO_2/Al_2O_3$ NPs (weight ratio=ZrO_2/Ni_9Pt=0.2): before DRM and after reduction 800°C for 3 h (A) together with histogram of Ni_9Pt particle size distribution (C) after DRM test (B) together with histogram of Ni_9Pt particle size distribution (D).

Figure 39**B** illustrates the temperature program reduction (TPR) profiles of the Ni_9Pt /Al_2O_3, $Ni_9Pt@TiO_2/Al_2O_3$ and $Ni_9Pt@ZrO_2/Al_2O_3$ (MO_2/Ni_9Pt weight ratio= ~0.2) catalysts. The TPR results show three different peaks at different temperature (150°C, 560°C and 800°C) for the Ni_9Pt/Al_2O_3 sample. The large peak at 560°C indicates the reduction of Ni_9Pt NPs, while, the small peak at 800°C is the reduction temperature of the $NiAl_2O_4$ spinel structure.[49, 51] Also, The TPR profile of $Ni_9Pt@TiO_2/Al_2O_3$ shows mainly a sharp peak at 800°C. The Ni_9Pt metal particles were reduced completely below 500°C in the case of $Ni_9Pt@ZrO_2/Al_2O_3$ and the 800°C reduction peak was not present which is in agreement with previous report[52]. It is well-known that the reducibility of NiO species in Ni-alumina catalysts strongly depend on the strength of interaction between the Ni and the support.[53] From the TPR results, the reduction of $Ni_9Pt@TiO_2/Al_2O_3$ sample happened mainly at 800°C indicating the strong interaction between metal and support and formation of $NiAl_2O_4$. H_2 spillover is well-known phenomena which occur on TiO_2 supported catalyst where H_2 dissociated on Pt and H radical move to the TiO_2.[47] So, the high reduction temperature might also be attributed to the reduction of TiO_2 that led to the strong metal support interaction (SMSI) effect which could produce a type of intermetallic compound of Ni_9Pt/TiO_2.[47, 54-55] Most of the metal NPs of Ni_9Pt/Al_2O_3 sample, on the other hand, was reduced at low temperature (below 560°C) and only small part of the metal was reduced at 800°C, which indicates the small amount of $NiAl_2O_4$. The $NiAl_2O_4$ phase was not observed in the $Ni_9Pt@ZrO_2/Al_2O_3$ sample and all the metal reduced at low temperature (below 500°C). Interestingly, the presence of ZrO_2 oxide prevented the Ni_9Pt from forming $NiAl_2O_4$ spinel

structure.[56-57] The base site on ZrO_2 could be the reason for preventing the Ni_9Pt from forming $NiAl_2O_4$ spinel structure.[56-57]

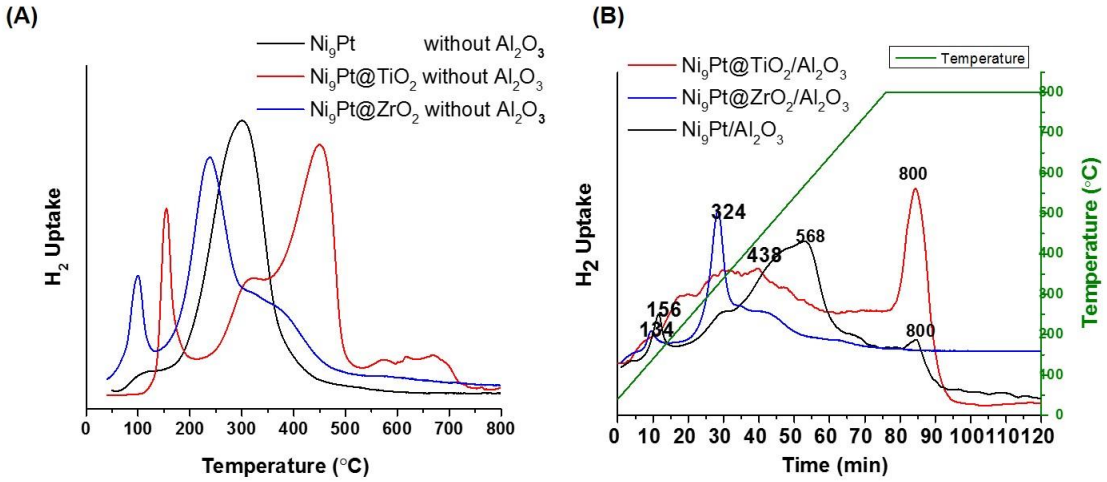

Figure 39. TPR profiles of Ni_9Pt and Ni_9Pt/MO_2 NPs (MO_2= TiO_2 or ZrO_2) (A) without Al_2O_3 support (B) with Al_2O_3 support.

X-ray diffraction (XRD) analysis was done on the alumina supported $Ni_9Pt@TiO_2/Al_2O_3$, $Ni_9Pt@ZrO_2/Al_2O_3$ (MO_2/Ni_9Pt ratio= ~0.2) and Ni_9Pt/Al_2O_3 samples before and after DRM test (**Figure 40**). The XRD spectra corresponding to NiPt alloy composition with face-centered cubic (fcc) phase [111] and [200] were observed for all the samples, and Ni, Pt and $NiAl_2O_4$ peaks were absent.[58] It is evident that the peaks of monometallic Ni and Pt were shifted to bimetallic NiPt alloy. The crystal sizes of Ni_9Pt before DRM for Ni_9Pt/Al_2O_3, $Ni_9Pt@TiO_2/Al_2O_3$, and $Ni_9Pt@ZrO_2/Al_2O_3$ catalysts were (10.25, 10.76 and 7.35 nm), respectively, calculated using the Scherrer equation. After dry reforming of methane, the crystal sizes of Ni_9Pt for Ni_9Pt/Al_2O_3, $Ni_9Pt@TiO_2/Al_2O_3$, and $Ni_9Pt@ZrO_2/Al_2O_3$ catalysts

were (16, 12 and 14 nm), respectively. Also, the XRD pattern of the $Ni_9Pt@TiO_2/Al_2O_3$ sample shows anatase crystallographic phase TiO_2 spectrum that appeared at (q =25).[59] As for the $Ni_9Pt@ZrO_2/Al_2O_3$ sample, a tetragonal crystal phase of ZrO_2 was detected.[59]

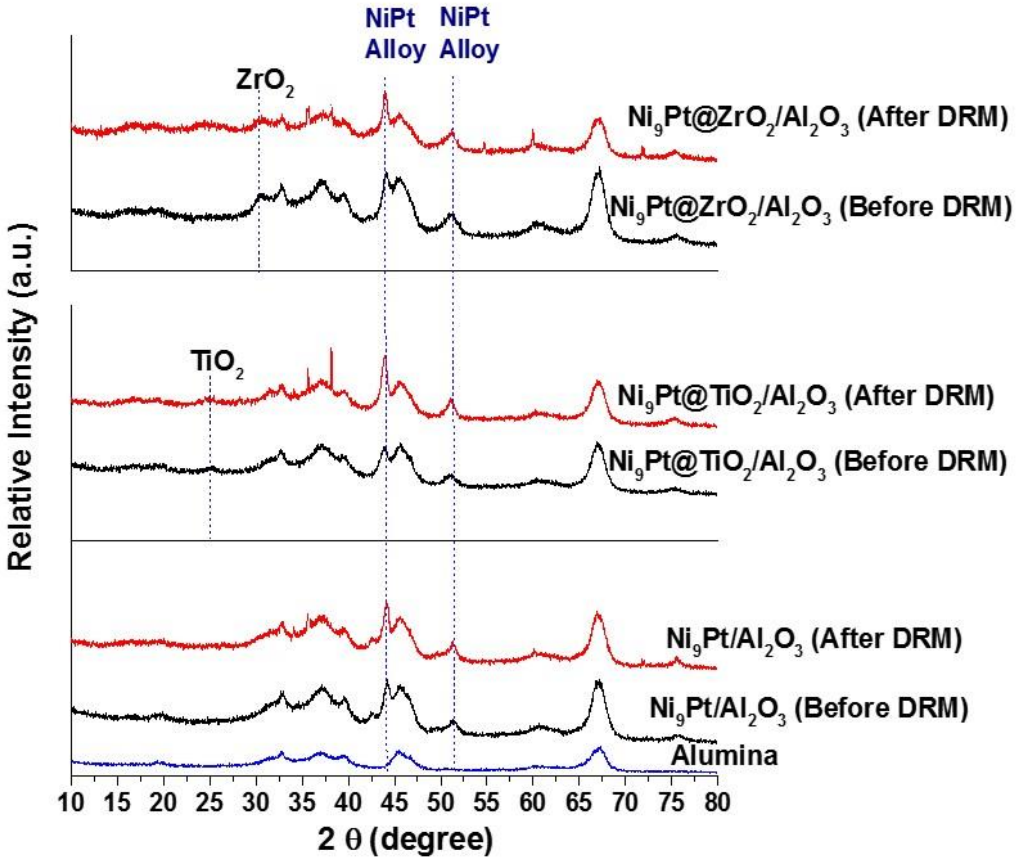

Figure 40. XRD pattern of Ni_9Pt/Al_2O_3 and $Ni_9Pt@MO_2/Al_2O_3$ NPs (weight ratio=MO_2/Ni_9Pt=0.2) (MO_2= TiO_2 or ZrO_2). Blue: Al_2O_3 support alone, black: before DRM and after reduction 800°C for 3 h and red: after DRM test.

The conclusion from the structural characterization and DRM test is the coating of the ZrO_2 layer over Ni_9Pt bimetallic NP has prevented the formation of $NiAl_2O_4$ spinel structure[56-57] and reduced the metal sintering at high temperature (800°C) and under DRM condition. As a result, the initial and stability conversion of methane had improved compared with uncoated Ni_9Pt with small amount of coke was produced. The structural and activity enhancement of $Ni_9Pt@ZrO_2/Al_2O_3$ catalyst might be due to the Lewis acid-base properties of ZrO_2 and the encapsulation of Ni_9Pt NPs within ZrO_2 structure. The embedded structure of $Ni_9Pt@ZrO_2$ increases the interface between the Ni_9Pt and ZrO_2 and reduces metal growth. The Lewis base sites of ZrO_2 improves the adsorption and activation of CO_2 especially at the perimeter between Ni_9Pt and ZrO_2.[36] Coating the Ni_9Pt bimetallic NPs with TiO_2, on the other hand, had also improved the methane conversion in addition to the significant reduction of coke formation during DRM. TiO_2 oxide was more sensitive against sintering compared with ZrO_2 as observed by TPR, which led to the incomplete protection of Ni_9Pt bimetallic NPs within TiO_2. Nevertheless, the presence of TiO_2 had suppressed carbon formation and enhanced the catalyst activity towards DRM reaction. The redox property of TiO_2 produces oxygen vacancies which can store oxygen from CO_2 activation and then release it.[37] Those released oxygen from TiO_2 can react with carbon accumulated on the metal from methane dissociation at the metal-TiO_2 boundaries.[37] Therefore embedding Ni_9Pt NPs within TiO_2 matrix has maximized the interface between Ni_9Pt and TiO_2 and thus prompted the oxidation of deposited carbon.

4.5. Conclusion and future outlook

Ni_9Pt alloy NPs with uniform size (3.4±1.5 nm) were synthesized via reverse micro-emulsion method. Addition of metal butoxide $M(OC_4H_9)_4$ (M=Ti or Zr) to the micelles containing the Ni_9Pt NPs generated aggregates of TiO_2 or ZrO_2 that deposited around the Ni_9Pt NPs via rapid hydrolysis. The samples were treated at 400°C for 3 h under air to remove the surfactant residue completely which led to the segregation of some of the Ni from Ni_9Pt alloy as NiO forming Ni_9Pt@NiO core-shell structure. TiO_2 was incorporated to the NiO shell forming NiO-TiO_2 composite surrounding the Ni_9Pt alloy whereas ZrO_2 did not diffuse through the NiO shell. The Ni_9Pt@NiO core-shell structure was no longer evident after reduction at 400 or 800°C for both TiO_2 and ZrO_2 samples due to the reduction of NiO shell. Consequently, embedded structure of Ni_9Pt@TiO_2 and Ni_9Pt@ZrO_2 catalysts were formed. The amount of oxide with respect to the Ni_9Pt NPs was crucial since excess amount of oxide was subjected to phase transfer at high reduction temperature (800°C) forming crystalline nanorod morphology and crystalline irregular structure of TiO_2 and ZrO_2, respectively. The phase transfer of the oxides phenomena from amorphous to crystalline coincided with sintering and growth of the encapsulated the Ni_9Pt NPs. Therefore, to minimize the formation of crystalline oxide during DRM condition, the amount of TiO_2 and ZrO_2 were reduced (MO_2/Ni_9Pt weight ratio= 0.2) and Ni_9Pt@oxide NPs were dispersed on the Al_2O_3 support to isolate the small Ni_9Pt@oxide particles. Ni_9Pt@TiO_2 and Ni_9Pt@ZrO_2 NPs were deposited on an Al_2O_3 support to increase their dispersion giving a 5% loading of Ni. The catalysts were calcined at 400°C and further reduced at 800°C

for 3 h before they was tested in DRM reaction. The reduction behavior of the catalysts after calcination 400°C were studied by TPR technique. TPR profile of $Ni_9Pt@TiO_2$ sample exhibited high reduction temperature (800°C) that can be attributed to the reduction of TiO_2 oxide and/or reduction of $NiAl_2O_4$ spinel structure; while all Ni_9Pt NPs was reduced completely at a low temperature (below 500°C). The XRD measurements confirmed the presence of NiPt alloy composition with face-centered cubic (fcc) phase in all the samples and Ni, Pt and $NiAl_2O_4$ peaks were absent. It is evident that the peaks of monometallic Ni and Pt were shifted to bimetallic NiPt alloy, also peaks of TiO_2 and ZrO_2 were observed. The crystal size of Ni_9Pt NPs of $Ni_9Pt@TiO_2$ and $Ni_9Pt@ZrO_2$ catalysts before and after DRM did not change significantly (~10 nm). The coating of the oxide layer (TiO_2 and ZrO_2) over Ni_9Pt NPs had reduced the metal growth significantly during the condition of the DRM reaction compared with uncoated Ni_9Pt NPs The average size of Ni_9Pt NPs in $Ni_9Pt@ZrO_2$ catalyst were 2.4 and 4.3 nm before and after DRM reaction, respectively. Whereas, the TiO_2 material was more sensitive to high temperature than ZrO_2 and the average size of Ni_9Pt NPs were 4 and 8.8 nm before and after DRM reaction, respectively. The catalytic activity of bimetallic Ni_9Pt NPs for DRM greatly improved by coating these particles with TiO_2 and ZrO_2 layer. The small size of Ni_9Pt NPs, Lewis base sites on ZrO_2 and redox properties of TiO_2 might be the reasons to give stable catalytic performance and reduced amount of coke formed during at least 20 h of DRM reaction. Indeed, redox properties of TiO_2 have suppressed the coke formation during DRM reaction on $Ni_9Pt@TiO_2$ catalyst.

Studying the reaction mechanism of $Ni_9Pt@TiO_2$ and $Ni_9Pt@ZrO_2$ catalysts during the DRM test will help in understanding deep reasons and causes of catalytic improvements. Thus conducting kinetic study of DRM reaction on $Ni_9Pt@TiO_2$ and $Ni_9Pt@ZrO_2$ catalysts at steady state will be great of interest to know also the activation energy of theses catalysts.

4.6. References

[1] A. Bhattacharyya, V. W. Chang, in *Studies in Surface Science and Catalysis, Vol. Volume 88* (Eds.: B. Delmon, G. F. Froment), Elsevier, **1994**, pp. 207-213.

[2] J. R. Rostrup-Nielsen, J. Sehested, J. K. Nørskov, in *Advances in Catalysis, Vol. Volume 47*, Academic Press, **2002**, pp. 65-139.

[3] K. Aasberg-Petersen, I. Dybkjær, C. V. Ovesen, N. C. Schjødt, J. Sehested, S. G. Thomsen, *Journal of Natural Gas Science and Engineering* **2011**, *3*, 423-459.

[4] J. H. Bitter, W. Hally, K. Seshan, J. G. van Ommen, J. A. Lercher, *Catalysis Today* **1996**, *29*, 349-353.

[5] J. Rostrup-Nielsen, in *Catalysis, Vol. 5* (Eds.: J. Anderson, M. Boudart), Springer Berlin Heidelberg, **1984**, pp. 1-117.

[6] A. T. Ashcroft, A. K. Cheetham, M. L. H. Green, P. D. F. Vernon, *Nature* **1991**, *352*, 225-226.

[7] S. C. Tsang, J. B. Claridge, M. L. H. Green, *Catalysis Today* **1995**, *23*, 3-15.

[8] J. R. Rostrup-Nielsen, *Catalysis Today* **2002**, *71*, 243-247.

[9] B. Delmon, *Applied Catalysis B: Environmental* **1992**, *1*, 139-147.

[10] J. R. Rostrup-Nielsen, in *Studies in Surface Science and Catalysis, Vol. Volume 81* (Eds.: H. E. Curry-Hyde, R. F. Howe), Elsevier, **1994**, pp. 25-41.

[11] M. C. J. Bradford, M. A. Vannice, *Catalysis Reviews-Science and Engineering* **1999**, *41*, 1-42.

[12] S. Wang, G. Q. Lu, G. J. Millar, *Energy & Fuels* **1996**, *10*, 896-904.

[13] M.-S. Fan, A. Z. Abdullah, S. Bhatia, *ChemCatChem* **2009**, *1*, 192-208.

[14] A. M. Gadalla, B. Bower, *Chem. Eng. Sci.* **1988**, *43*, 3049-3062.

[15] D. L. Trimm, *Applied Catalysis A: General* **2001**, *212*, 153-160.

[16] J. A. Moulijn, A. E. van Diepen, F. Kapteijn, *Applied Catalysis A: General* **2001**, *212*, 3-16.

[17] D. Chen, K. O. Christensen, E. Ochoa-Fernández, Z. Yu, B. Tøtdal, N. Latorre, A. Monzón, A. Holmen, *Journal of Catalysis* **2005**, *229*, 82-96.

[18] J. R. Rostrupnielsen, J. H. B. Hansen, *Journal of Catalysis* **1993**, *144*, 38-49.

[19] J. T. Richardson, S. A. Paripatyadar, *Applied Catalysis* **1990**, *61*, 293-309.

[20] D. Qin, J. Lapszewicz, *Catalysis Today* **1994**, *21*, 551-560.

[21] J. Lu, B. Fu, M. C. Kung, G. Xiao, J. W. Elam, H. H. Kung, P. C. Stair, *Science* **2012**, *335*, 1205-1208.

[22] J.-H. Kim, D. J. Suh, T.-J. Park, K.-L. Kim, *Applied Catalysis A: General* **2000**, *197*, 191-200.

[23] R. A. Van Santen, M. Neurock, *Catalysis Reviews* **1995**, *37*, 557-698.

[24] A. J. Forman, J.-N. Park, W. Tang, Y.-S. Hu, G. D. Stucky, E. W. McFarland, *ChemCatChem* **2010**, *2*, 1318-1324.

[25] L. Li, S. He, Y. Song, J. Zhao, W. Ji, C.-T. Au, *Journal of Catalysis* **2012**, *288*, 54-64.

[26] P. Jung-Nam, Z. Peng, H. Yong-Sheng, W. M. Eric, *Nanotechnology* **2010**, *21*, 225708.

[27] S. H. Joo, J. Y. Park, C. K. Tsung, Y. Yamada, P. Yang, G. A. Somorjai, *Nat Mater* **2009**, *8*, 126-131.

[28] J.-N. Park, A. J. Forman, W. Tang, J. Cheng, Y.-S. Hu, H. Lin, E. W. McFarland, *Small* **2008**, *4*, 1694-1697.

[29] S. Takenaka, Y. Orita, H. Umebayashi, H. Matsune, M. Kishida, *Applied Catalysis A: General* **2008**, *351*, 189-194.

[30] J. W. Han, C. Kim, J. S. Park, H. Lee, *ChemSusChem* **2014**, *7*, 451-456.

[31] D. Pakhare, J. Spivey, *Chemical Society Reviews* **2014**, *43*, 7813-7837.

[32] J. H. Bitter, K. Seshan, J. A. Lercher, *Journal of Catalysis* **1998**, *176*, 93-101.

[33] G. K. Reddy, S. Loridant, A. Takahashi, P. Delichère, B. M. Reddy, *Applied Catalysis A: General* **2010**, *389*, 92-100.

[34] S. M. Stagg-Williams, F. B. Noronha, G. Fendley, D. E. Resasco, *Journal of Catalysis* **2000**, *194*, 240-249.

[35] M. M. V. M. Souza, D. A. G. Aranda, M. Schmal, *Journal of Catalysis* **2001**, *204*, 498-511.

[36] X. Du, L. J. France, V. L. Kuznetsov, T. Xiao, P. P. Edwards, H. AlMegren, A. Bagabas, *Applied Petrochemical Research* **2014**, *4*, 137-144.

[37] K. Takehira, *Catalysis Surveys from Asia* **2002**, *6*, 19-32.

[38] X. Zhang, H. Wang, B.-Q. Xu, *The Journal of Physical Chemistry B* **2005**, *109*, 9678-9683.

[39] J.-M. Wei, B.-Q. Xu, J.-L. Li, Z.-X. Cheng, Q.-M. Zhu, *Applied Catalysis A: General* **2000**, *196*, L167-L172.

[40] H. Sakai, T. Kanda, H. Shibata, T. Ohkubo, M. Abe, *Journal of the American Chemical Society* **2006**, *128*, 4944-4945.

[41] P. M. Arnal, M. Comotti, F. Schüth, *Angewandte Chemie International Edition* **2006**, *45*, 8224-8227.

[42] I. Capek, *Advances in Colloid and Interface Science* **2004**, *110*, 49-74.

[43] M. Boutonnet, S. Lögdberg, E. Elm Svensson, *Current Opinion in Colloid & Interface Science* **2008**, *13*, 270-286.

[44] J. Eastoe, M. J. Hollamby, L. Hudson, *Adv Colloid Interface Sci* **2006**, *128-130*, 5-15.

[45] K. Tomishige, S. Kanazawa, M. Sato, K. Ikushima, K. Kunimori, *Catalysis Letters* **2002**, *84*, 69-74.

[46] S. R. de Miguel, I. M. J. Vilella, S. P. Maina, D. San José-Alonso, M. C. Román-Martínez, M. J. Illán-Gómez, *Applied Catalysis A: General* **2012**, *435–436*, 10-18.

[47] S. J. Tauster, S. C. Fung, R. L. Garten, *Journal of the American Chemical Society* **1978**, *100*, 170-175.

[48] J. A. Lercher, J. H. Bitter, W. Hally, W. Niessen, K. Seshan, in *Studies in Surface Science and Catalysis, Vol. Volume 101* (Eds.: W. N. D. E. I. Joe W. Hightower, T. B. Alexis), Elsevier, **1996**, pp. 463-472.

[49] L. Zhou, L. Li, N. Wei, J. Li, J.-M. Basset, *ChemCatChem* **2015**, *7*, 2508-2516.

[50] K. An, Q. Zhang, S. Alayoglu, N. Musselwhite, J.-Y. Shin, G. A. Somorjai, *Nano Letters* **2014**, *14*, 4907-4912.

[51] C. Jiménez-González, Z. Boukha, B. de Rivas, J. R. González-Velasco, J. I. Gutiérrez-Ortiz, R. López-Fonseca, *Energy & Fuels* **2014**, *28*, 7109-7121.

[52] V. M. Gonzalez-Delacruz, R. Pereñiguez, F. Ternero, J. P. Holgado, A. Caballero, *ACS Catalysis* **2011**, *1*, 82-88.

[53] M. Zangouei, *The influence of nickel loading on reducibility of NiO/Al2O3 catalysts synthesized by sol-gel method*, Bangladesh University of Engineering and Technology, **2010**.

[54] O. S. Alexeev, S. Y. Chin, M. H. Engelhard, L. Ortiz-Soto, M. D. Amiridis, *The Journal of Physical Chemistry B* **2005**, *109*, 23430-23443.

[55] S. J. Tauster, *Accounts of Chemical Research* **1987**, *20*, 389-394.

[56] C. Li, Y. Fu, G. Bian, T. Hu, Y. Xie, J. Zhan, *Journal of Natural Gas Chemistry* **2003**, *12*, 167-177.

[57] H. S. Roh, K. W. Jun, S. C. Baek, S. E. Park, *BULLETIN-KOREAN CHEMICAL SOCIETY* **2002**, *23*, 793-794.

[58] M. García-Diéguez, E. Finocchio, M. Á. Larrubia, L. J. Alemany, G. Busca, *Journal of Catalysis* **2010**, *274*, 11-20.

[59] M. E. Manríquez, T. López, R. Gómez, J. Navarrete, *Journal of Molecular Catalysis A: Chemical* **2004**, *220*, 229-237.

CHAPTER 5

5. SUMMARY AND FUTURE OUTLOOK

Water-in-oil reverse micro-emulsion technique is a promising synthetic procedure to produce mono-dispersed small NPs with precise control of their size and morphologies. Moreover, it is an effective tool for the synthesis of oxides shell with high control of their composition, thickness, and size of metal oxide shell. The thickness of oxide layer can be modified by changing some parameters such as the concentration of precursors, catalysts, coating time, and the presence of other reactants.

I utilized reverse micro-emulsion technique to develop an embedded catalysts that can protect metal NPs against sintering at high temperature by encapsulation within a porous oxide shell. The embedded metal catalyst can be heated to 500°C or above without loss of activity as observed during the CO oxidation and dry reforming tests. High thermal stability against metal sintering was achieved by a protective layer of oxide around the metal NPs that avoids the direct contact between the particles thus the particle growth via particle coalescence is inhibited.

Chapter 2 presents the mechanism of forming Pt@SiO_2 core-shell particles and the influence of aging time of Pt colloids and addition time of SiO_2 precursor on the properties and morphology of the Pt/SiO_2 NPs using reverse micro-emulsion method. The promising results including high catalytic activity during CO

oxidation reaction of $Pt@SiO_2$ core-shell motivated to extend this concept to other catalytic reactions, and different core composition as well as the chemical nature of the shell material.

The concept of catalyst stabilization by a core-shell method was employed in **chapter 3** for the development of further variations on the entrapment of Pt NPs within another oxides layer such as ZrO_2 and TiO_2. The TiO_2 and ZrO_2 precursors hydrolyzed rapidly once it contacted the water present in the micelles, which formed amorphous oxides that were aggregated and deposited around the Pt NPs. The amount of ZrO_2 and TiO_2 in respect to the Pt NPs were varied to cover the Pt NPs fully with TiO_2 and ZrO_2 layer. The Pt NPs embedded within these oxides matrix were stable against sintering and catalytic activate during the CO oxidation reaction after thermal treatment at elevated temperatures.

Chapter 4 describes the investigation/study of a more challenging system to synthesize than Pt monometallic particle, namely, bimetallic Ni_9Pt NPs that can be used for high temperature dry reforming of methane reaction. Ni NPs were added to the Pt in attempt to increase the activity of the catalysts and to make it suitable for the application of dry reforming of methane. The amount of ZrO_2 and TiO_2 were varied to achieve the right amount of the oxides relative to the amount of Ni_9Pt NPs. Both $Ni_9Pt@TiO_2$ and $Ni_9Pt@ZrO_2$ catalysts exhibited high stability in the dry reforming of methane at 750°C and improved the sintering resistance property compared to uncoated Ni_9Pt NPs.

My preliminary results of dry reforming of methane on $Ni_9Pt@TiO_2$ and $Ni_9Pt@ZrO_2$ catalysts suggest that future study is required to understand deeply

the reasons and causes of catalytic improvements. Thus conducting the kinetic study of DRM reaction on $Ni_9Pt@TiO_2$ and $Ni_9Pt@ZrO_2$ catalysts at steady state could be informative to know also the activation energy of theses catalysts. Also, a precise design of TiO_2 and ZrO_2 deposition around the metal particles was challenging since the hydrolysis rate of Ti and Zr (IV) butoxide was rapid. Therefore, controlling the hydrolysis rate of TiO_2 and ZrO_2 precursors' by modifying their precursors with a longer organic chain or altering other experimental parameters such as pH, water content, organic solvent type, etc. could be further investigated.

LIST OF PUBLICATION

(1) "Design of Core-Shell Pt-SiO_2 Catalyst in Reverse Microemulsion System: Distinctive Kinetics on CO Oxidation at Low Temperature"

Noor Almana, Somphonh Peter Phivilay, Mohamed N. Hedhili, Paco Laveille, Paolo Fornasiero, Kazuhiro Takanabe, Jean-Marie Basset, *J. Catal.* **2016 Accepted**

LIST OF CONFRENCES

2015 KCC Scientific Advisory Board Meeting

(Selected *poster presentation*) KAUST, Saudi Arabia.

2015 Chemistry of natural resources, 249th ACS National Meeting

(*Oral presentation and poster presentation*) Denver, USA.

2015 KCC Catalytic carbon and hydrogen management symposium

(*Poster presentation*) KAUST, Saudi Arabia.

2014 KAUST-ACS on campus

(*Poster presentation*) KAUST, Saudi Arabia.